Spring 1-1-2012

Fast kinetics of human myosin heavy chain contraction in health and disease

John C. Deacon
University of Colorado at Boulder, jcdeacon@gmail.com

FAST KINETICS OF HUMAN MYOSIN HEAVY CHAIN CONTRACTION IN HEALTH AND DISEASE

by

JOHN C. DEACON

B.A. University of California, Berkeley, 2007

A thesis submitted to the faculty of the Graduate School of the University of Colorado
in partial fulfillment of the requirement for the degree of Doctor of Philosophy
in the Department of Molecular Cellular and Developmental Biology

2012

This thesis entitled:
Fast kinetics of human myosin heavy chain contraction in health and disease
written by John C. Deacon
has been approved for the Department of
Molecular Cellular and Developmental Biology

_____
Thomas Perkins, Chair

_____
Shelley Copley

_____
Michael Stowell

_____
Johannes Rudolph

_____
Leslie Leinwand

_____
Date

The final copy of this thesis has been examined by the signatories and we find that both the content and the form meet acceptable presentation standards of scholarly work in the above mentioned discipline.

Deacon, John C. (Ph.D. candidate, Molecular Cellular and Developmental Biology)

Fast kinetics of human myosin heavy chain contraction in health and disease

Thesis directed by Leslie A. Leinwand, Professor of Distinction, Molecular, Cellular and Developmental Biology

The myosin heavy chain composition of human heart and skeletal muscles is dynamic in health and disease and is known to define the maximum velocity and force generated by contracting muscles. The study of the individual isoforms that comprise this diversity has recently been aided by the development of a recombinant expression system capable of producing functional sarcomeric human myosin motors. The eight primary human sarcomeric myosin isoforms are herein shown to differ by between 1.5- and 4.5-fold in their F-actin-activated ATPase activities. Due to the greatly differing contractile environments in which they function it has been anticipated that the kinetics of the reactions that comprise the contractile cycle vary to an even greater extent. Using pre-steady-state techniques it is possible to determine the kinetics of the steps of myosin contraction. Among the eight isoforms tested, we observe multiple biochemical patterns that differentiate the motors into fast-moving and slow, tension-maintaining categories. Additionally, we have characterized pathological point mutations associated with developmental and cardiac disease. We find that unique patterns of alteration to the reactions of the myosin ATPase cycle characterize each mutation. These alterations are predicted to cause significant disruptions to the reactions governing attachment and detachment between myosin and F-actin. These studies lay the foundation for structure vs. function analysis of pathological myosin mutations and fill an important void in understanding the contributions of the various myosin isoforms to human muscle contraction.

ACKNOWLEDGEMENTS

The author acknowledges the contributions of Daniel Resnicow, for development of the expression system and the majority of the steady-state data, Steve Langer, for expertise in tissue culture, cloning and recombinant adenoviral production, Ariana Combs, for tissue culture, Jiaju Shen, for his involvement in work on embryonic and FSS kinetics, Marieke Bloemink, for stopped-flow and kinetics training, as well as significant contributions of data and coauthorship at the University of Kent, Sam Lynn, for actin purification at the University of Kent, Nancy Adamek, for quenched-flow assays at the University of Kent, Hans Warrick, for motility assays, data, and training at Stanford University, Kathy Ruppel and Jim Spudich, for reagents, clones, and training at Stanford University, and Dima Klenchin and Ivan Rayment for crystallography work at the University of Wisconsin. The author also acknowledges the significant contributions of his mentors Leslie Leinwand and Michael Geeves in training, motivating and in innumerable ways making this work possible. Finally, the author acknowledges the members of this thesis committee, Tom Perkins, Shelley Copley and Michael Stowell for their time, advice and training over the years spanning this work, and especially its most recent member, Johannes Rudolph, for his extensive support in the revision of this thesis. This work was funded in part by National Institutes of Health - University of Colorado Molecular Biophysics Training Grant T32 GM65013.

CONTENTS

TABLES

FIGURES

GENERAL INTRODUCTION

General muscle biology

The evolution of large mobile animals necessitated the development of coordinated systems for locomotion. The musculoskeletal system of vertebrates consists of a set of highly coordinated and functionally dynamic structures. To meet the demands of a wide variety of activities, muscles must be able to rapidly contract, to generate and sustain high tension, and in some cases to contract repetitively for decades. Muscle systems in larger animals must also be capable of coordination and control by nervous system signals. This is achieved by a highly conserved set of cellular processes.

The two primary categories of muscle are smooth muscle and striated muscle. These can be distinguished microscopically. Striated muscle cells are characterized visually by a repeated pattern of banded structures (Figure 1A, B), while smooth muscles lack these banded structures (Figure 1C, D)[5]. The structure responsible for the banded pattern in striated muscles is the sarcomere, which is the basic contractile unit of striated muscle. Within the muscle fiber sarcomeres are linked end-to-end into long cylindrical bodies, known as myofibrils (Figure 2)[4, 5]. The sarcomere is composed of interdigitated thick and thin filaments consisting primarily of myosin and actin, respectively (Figure 3). The sarcomere contracts by the motor activity of myosin while bound to actin in what is termed a "crossbridge" between the filaments[6]. Smooth muscles also generate contractile force by interactions between actin and myosin but do so in a different manner without the regular, organized, and coordinated structures of the sarcomere[7].

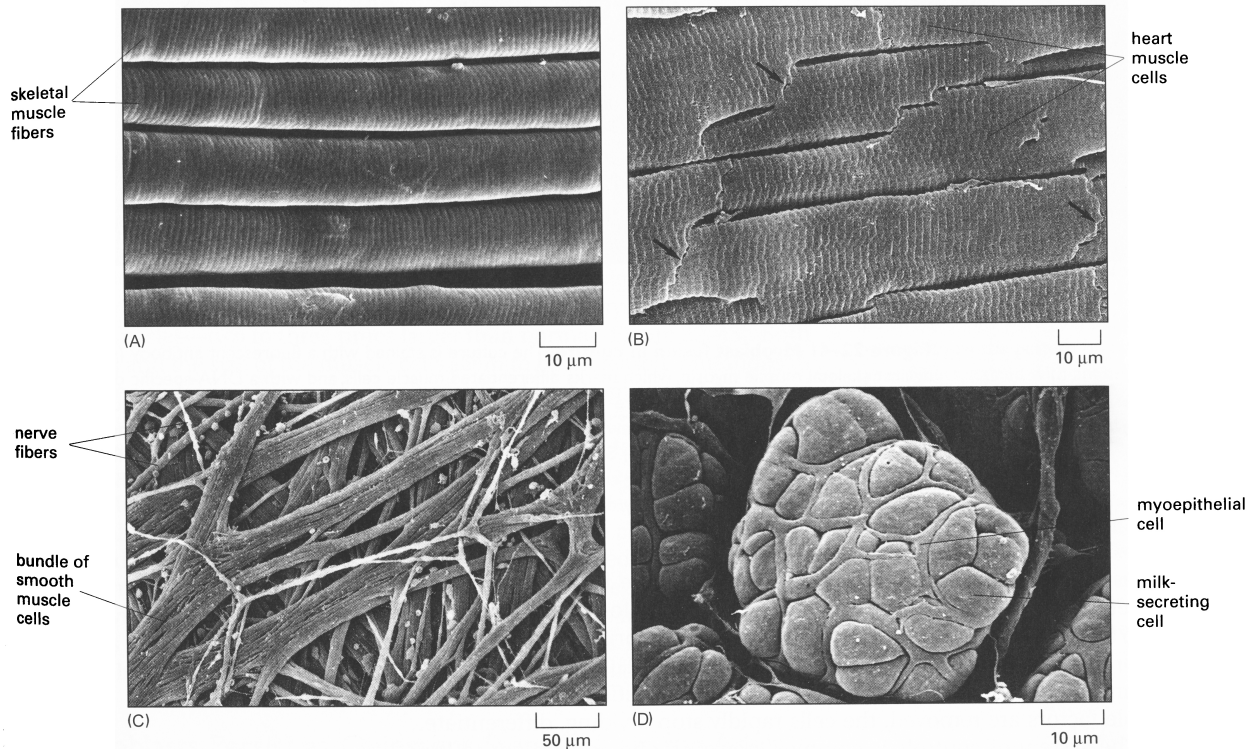

Figure 1: Electron micrographs of striated and smooth muscles. Scanning electron micrographs of skeletal (A) and cardiac (B) striated muscles and smooth muscles (C and D). Most obviously striated and smooth muscle cells differ morphologically in shape, uniformity, and in the characteristic banding that is seen in striated muscles and not in smooth muscles. These morphological differences reflect their functional differences, as striated muscles are responsible for rapid directional contraction and smooth muscles for slower and commonly constricting contraction. Adapted from Alberts, et al. (2002) Molecular Biology of the Cell[5].

Figure 2: Fluorescence micrograph of ventricular myocytes. Neonatal rat ventricular myocytes transfected with an α-myosin heavy chain rod domain fusion with GFP shows incorporation of the exogenous rod protein-GFP fusion into the sarcomeres (GFP signal is shown as white). The long tubular structures composed of end-to-end linked sarcomeres are myofibrils. Each cell contains many myofibrils aligned with one another for coordinated contractile activity. Adapted from Buvoli, et al. (2012) Effects of Pathogenic Proline Mutations on Myosin Assembly[4].

Striated muscles are responsible for all voluntary muscle contraction as well as several involuntary functions, including control of the larynx and heart contraction[8]. Striated muscle can be subcategorized into skeletal and cardiac muscles. Skeletal muscles, as the name implies, are primarily associated with skeletal movement. In larger animals such as humans these muscles can span well over a foot in length. Skeletal muscle fibers reflect this contractile environment in that they are long and thin (Figure 1A). Additionally, skeletal muscle fibers have many nuclei distributed through the cell near the cell surface. The heart, by contrast, is a far more compact structure. While skeletal muscles typically contract along a single axis of movement, heart musculature produces multidirectional contractile force in the process of constricting the heart's chambers. Cardiac muscle fibers reflect this contractile environment morphologically by their short, columnar shape (Figure 1B), which allows for more axes of contraction within the muscle[5, 8, 9]. While skeletal and cardiac fibers differ most obviously in their shape and size, they carry distinct proteomes as well[10, 11].

Cardiac muscle fibers differ in contractile protein composition among animals as well as regionally within the heart, between atria and ventricles, but are morphologically relatively uniform in adults. Skeletal muscles have a great deal of fiber type diversity. Skeletal muscle fibers have been broadly categorized into slow, type I, fibers and fast, type II, fibers. The fiber types are characterized primarily by metabolic activity, from slow oxidative metabolism to fast glycolytic metabolism as a function of the activity ratios of metabolic enzymes, such as hexokinase, phosphofructokinase, and fructose-1,6-bisphosphatase[12]. The fast, type II, fibers have been further characterized into the relatively slower type IIA, the intermediate IID/X and the fastest class, IIB[12]. Differences in contractile velocity among fiber types are closely correlated with differences in the sarcomeric proteome, particularly with respect to the isoforms

of the molecular motor protein, myosin.

The release of calcium into the cytosol of muscle cells is the signal that initiates muscle contraction. Triggered by neuromuscular interactions in skeletal muscle or intrinsic systems in the heart, a brief influx of calcium ions from outside the cell activates the release of calcium ions stored in the sarcoplasmic reticulum. The calcium binds to regulatory protein complexes in the contractile apparatus to allow contraction to occur[13, 14]. Upon activation of muscle contraction in this manner, the contractile apparatus of the muscle generates contractile force. The sarcomeric machinery that produces muscle contraction is the subject of this thesis.

The sarcomere

The sarcomere is composed of three primary structures, the Z-disc, the thin filament, and the thick filament (Figure 3). The Z-disc anchors the filaments of the sarcomere and by cooperation with two massive proteins, nebulin and titin, forms a frame for the sarcomere[15, 16]. The thin filaments anchor to α-actinin proteins in the Z-disc[15, 17, 18]. Nebulin, also anchored to the Z-disc, extends along the thin filament and is thought to regulate thin filament length[15, 19-22]. Titin, a large "elastic" protein, is anchored to the Z-disc and tethers thick filaments on either side of the Z-disc to hold them between thin filaments in a position to perform their role in sarcomere contraction[23-30]. The Z-disc differs in size among muscle fiber types. In cardiac and slow-contracting muscle fibers the microscopic band associated with this structure, the Z-band, is around 100 to 140 nm, whereas in fast-contracting skeletal muscle fibers the Z-band is far narrower, at around 30 to 50 nm[15, 31, 32].

The thin filament is primarily constructed of a helical pair of actin filaments. Actin polymerization and depolymerization are known to be very active in non-muscle cells, but in muscle cells actin polymer dynamics are tightly regulated by capping proteins[15, 33]. Actin

polymers have a polarity dictated by the orientation of the monomers in the filament. The "plus" or "barbed" end is the end of a filament where actin monomers are added as the filament elongates and is opposed by the "minus" or "pointed" end. Their descriptive names originate microscopically, where actin filaments decorated with bound myosin motor domains were observed to have a directionally oriented repeating arrowhead shape (Figure 4)[34-36].

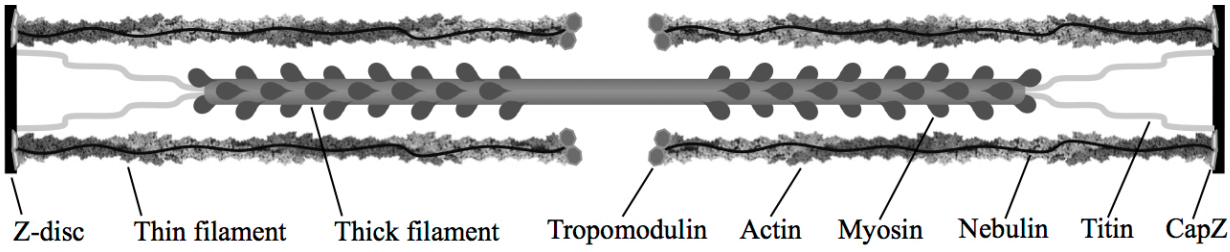

Figure 3: Sarcomere structure. Sarcomeres consist of interdigitated thin and thick filaments. Thin filaments consist of primarily actin polymers, which are capped at plus and minus ends by CapZ and tropomodulin proteins, respectively. They are also overlaid by the large protein nebulin, which may influence thin filament length. Thick filaments consist of primarily MyHC organized in parallel in the arms and antiparallel in the central "bare zone" where no myosin heads protrude. The filaments are each tethered to the Z-discs, the thin filament rigidly and directly and the thick filament flexibly by the large elastic protein titin. The bipolar orientation of the thick filament allows for coordinated interactions between actin and MyHC to produce contractile force, pulling together the Z-disks. Exposure of MyHC binding sites on actin filaments is governed by additional protein complexes which are regulated by Ca^{2+}, allowing for cell and tissue level coordination of contractile events.

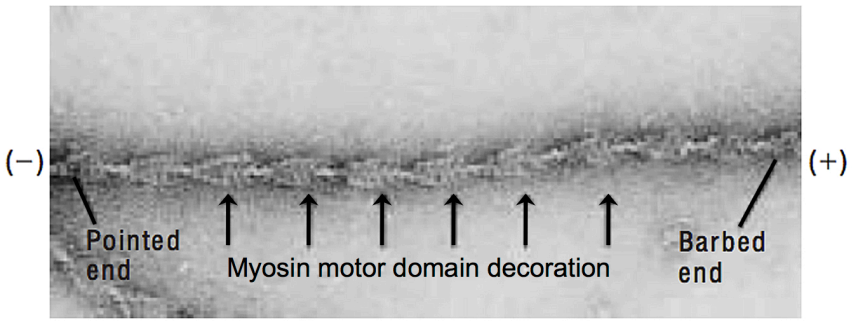

Figure 4: Actin filament polarity. Filamentous actin decorated by bound myosin motor domains has a characteristic arrowhead shape formed by the orientation of the myosin motor domain on the filament. Myosins are plus-end directed motors and thus orient uniformly on the two parallel strands of actin in its helical filamentous form. Adapted from Lodish et al. (2003) Molecular Cell Biology[35].

The actin filaments are anchored at their plus-ends to α-actinin in the Z-disc and capped by CapZ and tropomodulin proteins at their plus and minus-ends, respectively[15, 33]. While each thin filament is stable *in vitro* at around 1 μm in length from the Z-disc, in live cells tropomodulin capping is transient and some dynamics have been shown to occur at the minus-ends of the actin filaments[37-41]. The actin filament is bound by additional proteins, which regulate the activity of the thin filament in sarcomeric contraction. The troponin-tropomyosin complex regulates the availability of myosin binding sites on actin in the thin filament in a calcium-dependent manner, in response to calcium flux from the sarcoplasmic reticulum (Figure 5). Tropomyosin is a large protein, which interacts with actin filaments in such a way as to block the myosin binding site of actin. Its conformation is influenced by a complex of three troponin proteins, troponin I, troponin T and troponin C. Troponin C binds calcium and as a result undergoes a conformational change, which is transmitted through its binding partners troponin T and troponin I to alter the shape and position of tropomyosin on the thin filament, opening up myosin binding sites on the actin filaments to allow crossbridging[42-44].

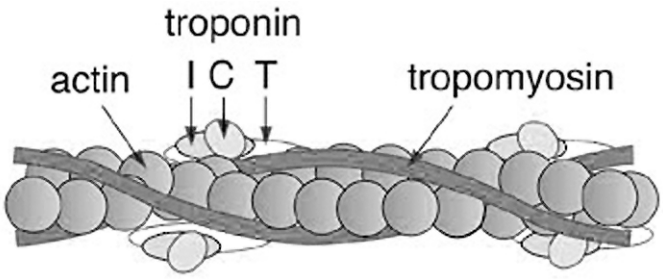

Figure 5: The regulatory complex on the thin filament. The thin filament is primarily constructed of two helical actin filaments. This basic structure is decorated with a complex of proteins which regulate the availability of myosin binding sites on actin, coupling availability to calcium signals associated with cellular activation of contraction. Tropomyosin binds to thin filament actin in such a way as to block binding sites on actin. A complex of three proteins, troponin T, troponin I, and troponin C respond to calcium release in the cell by changing shape and inducing conformational changes in tropomyosin to unblock myosin binding sites on actin (Adapted from http//:jolisfukyu.tokai-sc.jaea.go.jp/fukyu/tayu/ACT04E/04/0406.htm).

The third major substructure of the sarcomere is the thick filament. The thick filament is

primarily composed of myosin. Myosin is a heterohexamer consisting of two myosin heavy chain proteins (MyHC) each bound by a pair of non-identical myosin light chain proteins. MyHCs assemble their long α-helical rod domains into coiled-coils and subsequently into large filaments of approximately 300 MyHC proteins to form the primary structure of the thick filament. These proteins are arranged in parallel in the lateral regions of the filament and in anti-parallel in the center. Myosins are plus-end directed actin-based motors. With the plus-ends of actin filaments oriented towards the Z-discs of the sarcomere, the activity of actin-myosin interactions produces leads to the contraction of the Z-discs towards one another. The motor domains of MyHC proteins project outward from the thick filament, towards the surrounding thin filaments. At the junction between the motor and rod domain the MyHCs are bound by myosin light chains to produce a stiff lever arm, which also projects outward from the thick filament. Myosin binding protein-C, a thick filament protein, regulates the projection of the myosin motor domain away from the thick filament. The large thick filament structure is suspended between the thin filaments and Z-discs by the large elastic protein titin, proximal to multiple thin filaments. The interaction between the motor domains of the myosins in the thick filament and the actin in the thin filament leads to contraction of the sarcomere due to the cyclical ATP-dependent motor activity of the MyHC proteins. MyHC's cycle of activity is the subject of this study.

Myosin

Myosins comprise a large family of motor proteins involved in cellular activities such as cargo trafficking, cell division, and muscle contraction. Sequence alignments estimate that there may be as many as 17 phylogenetically distinct myosin subtypes[45]. The conventional myosin family involved in muscle contraction is the myosin II class. These myosins act in a coordinated

manner, bind two myosin light chains per heavy chain, and spend a low percentage of their enzymatically activated cycle bound to actin. The latter trait is referred to as having a low "duty ratio." The human striated muscle myosin II isoforms have been shown to play two roles in muscle contraction: fast movement and force maintenance[46]. These functional features will be discussed in depth later on.

Human striated muscles contain eight major myosin isoforms and two more recently discovered isoforms about which far less is known. The eight major myosins are clustered in the genome in two groups: the cardiac isoform group, α and β, and the skeletal isoform group, IIa, IIb, IId, perinatal, embryonic, and extraocular. These isoforms are encoded by separate genes known as MYH6, MYH7, MYH2, MYH4, MYH1, MYH8, MYH3 and MYH13, respectively[47]. MyHC-β is expressed in both cardiac muscle and slow skeletal muscle fibers. The roles of the more distantly related isoforms, MyHCs 15 and 7b, in mammalian muscles are currently being investigated.

This family of myosin isoforms is highly conserved, with amino acid sequence identities between 77% and 94% (Table 1). This high degree of sequence identity historically led to the hypothesis that MyHC isoforms would prove to be functionally very similar. While they are all F-actin-activated ATPases, the rates and affinities with which each carry out their ATPase and contractile functions can differ significantly even between highly related isoforms[1, 2]. This diversity of isoforms is therefore capable of producing a high degree of functional diversity by their differential expression in various muscles.

Myosin isoforms often exist in mixtures in muscle fibers with their expression tightly regulated. In muscle fibers, contractile and metabolic rates depend upon myosin composition[48]. The identities and proportions of the myosin isoforms in a fiber correlate with the fiber's

maximum shortening velocity[49]. This dependence underlies the importance of MyHCs in muscle contraction and how understanding the contractile characteristics of each isoform can contribute to understanding the dynamics of muscle contraction.

	α	β	IIa	IIb	IId	Peri	Emb	Exoc
α	*100*							
β	92	*100*						
IIa	80	81	*100*					
IIb	80	80	91	*100*				
IId	80	81	94	94	*100*			
Peri	80	80	92	90	92	*100*		
Emb	78	78	84	83	83	84	*100*	
Exoc	77	77	81	81	81	81	78	*100*

Table 1: Percent identity between human MyHC isoforms. Percent amino acid sequence identities between human MyHC isoforms were determined by pairwise alignments using ClustalW (http://www.ebi.ac.uk/Tools/msa/clustalw2) and sequences obtained from NCBI (http://www.ncbi.nlm.nih.gov/gene).

Human striated muscle MyHC isoforms are expressed in distinct spatial and temporal patterns. During embryonic development the embryonic, perinatal and β-MyHC isoforms predominate in skeletal muscles [50, 51]. At and around birth, embryonic and perinatal MyHC become undetectable. Their expression in adults is only detected in regenerating injured or diseased muscles[52]. The perinatal isoform is also expressed in the fetal heart[50, 51, 53, 54]. After birth, in humans, skeletal muscles primarily contain the fast skeletal isoforms, IIa and IId, and the slow β isoform[55-60]. The IIb isoform, which predominates in the skeletal muscles of small mammals such as mice, is not detectable in healthy human muscles, but the gene can encode a functional motor[61]. In specialized skeletal muscles such as the extraocular and laryngeal muscles, many isoforms are present, including the unique extraocular isoform[62-64]. In the adult human heart, β-MyHC predominates, accounting for >90% in the ventricles, while α represents the remainder[65]. By contrast, in small mammals such as mice and rats, the adult heart is comprised

of mainly α-MyHC[66].

MyHC contributes to muscle contraction through its coordinated activity in the sarcomere. MyHC proteins are ~200 kDa and contain two distinct functional domains: an α-helical rod domain which assembles into the thick filament, and a globular motor domain which binds actin and ATP (Figure 6). The motor domain is responsible for MyHC enzymatic function by coupling interactions with actin to a cycle of ATP hydrolysis and product release. Thick filaments are bipolar with arms of parallel MyHC molecules and a central bare zone of antiparallel MyHC where no motor domains protrude from the filament. In this way they are capable of contracting the sarcomere by motor domains in the arms binding to actin in the thin filaments and undergoing an ATP-dependent conformational change to produce linear movement along the thin filament. Because each pole of the thick filament does this in opposition, the net effect on the sarcomere as a whole is the contraction of the two Z-disks towards one another, shortening the sarcomere.

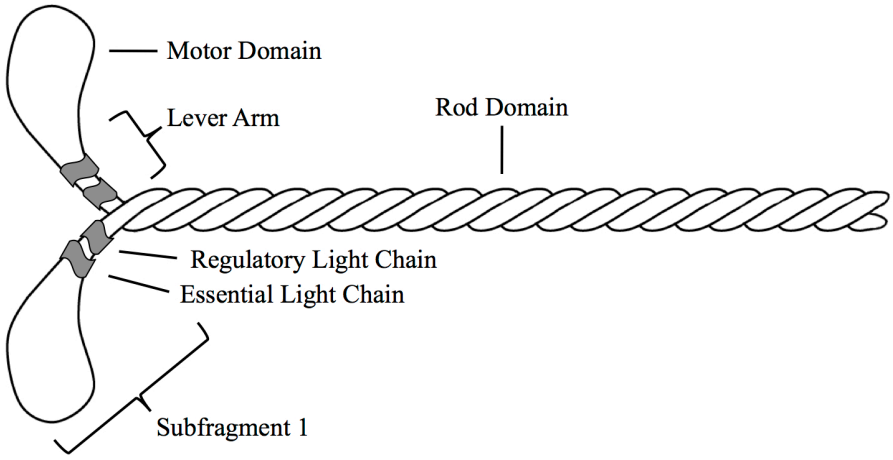

Figure 6: Myosin structure. The myosin molecule is a heterohexamer containing two heavy chains (in white), joined by their α-helical coiled-coil rod domains, and two pairs of non-identical light chains (in grey), one essential light chain (ELC) and one regulatory light chain (RLC), bound to each heavy chain to stiffen its lever arm. By papain cleavage at the intersection of the lever arm and rod domain a soluble fragment, Subfragment 1 (S1), can be isolated. S1 maintains all enzymatic and motor functions of the heavy chain.

Subfragment 1 (S1) of myosin contains the amino-terminal motor domain of MyHC and the myosin light chain binding lever arm. It lacks the carboxy-terminal α-helical coiled-coil rod domain, which is associated with the assembly of myosin into the thick filament. S1 is therefore a soluble fragment of MyHC and retains all of the enzymatic functions of the whole protein[67, 68]. This makes S1 a suitable fragment for *in vitro* assays. Subfragments of this sort were originally isolated from the full-length protein by proteolytic cleavage using papain and chymotrypsin. These proteases cleave full length MyHC at different positions and selectively in solvent exposed structures where the soluble proteases can access the peptide sequence. For this reason these two proteases produce two different subfragments. The papain-derived subfragment is the traditional S1[69], containing the motor domain and both light chain-binding "IQ domains," so named for the frequency with which the amino acids isoleucine (I) and glutamine (Q) are found at the beginning of the domain[70]. Chymotrypsin digestion produces a smaller subfragment by cleaving the heavy chain between the two light chain-binding domains, such that only the essential light chain is associated with the heavy chain subfragment[71]. This is herein referred to as "short-S1" or sS1.

The structure of the myosin motor domain has been determined by crystallographic methods. These studies describe a highly interactive set of substructures which can be observed in multiple stable conformations associated with the steps of the myosin contractile cycle[3, 72]. The motor domain was initially subclassified by additional proteolytic fragments. Limited proteolysis produced three fragments of the motor domain, which were referred to by their masses as the 25 kDa subunit including the amino terminus, the 50 kDa subunit including the bulk of the motor domain, and the 20 kDa subunit including the carboxy terminal end of the motor domain[73]. Two soluble loops joining these subunits to one another were also named for

their associated subunits: the 25-50 kDa loop or loop 1 and the 50-20 kDa loop or loop 2. Within subfragment 1 there are four primary functional domains. These are the actin-binding pocket, the enzymatic nucleotide-binding pocket, the converter domain, and the myosin light chain binding lever arm (Figure 7). The loops interact with these sites, such that loop 1 influences the nucleotide binding pocket and loop 2 influences actin binding[74]. Additional substructures support the functions of their domains, such as switch II which must be in the "closed" conformation for ATP hydrolysis activity to take place[75] and the SH1 helix which terminates in a flexible glycine residue thought to act as a hinge, which along with the neighboring relay helix interact with the converter to transfer rotational conformational changes in the motor domain to the lever arm (Figure 7)[76].

Crystallographic studies of S1 purified from muscle sources have indicated that S1 can exist in at least three conformational states, dictated by the contents of the nucleotide-binding pocket. These states were coined, the "near-rigor" state in the absence of nucleotide, the "pre-power-stroke" or "transition" state in the presence of ADP-VO_4, which mimics ADP and inorganic phosphate (P_i) after ATP hydrolysis, and the "detached" state in the presence of ADP (Figure 8). While these crystallographic views of myosin structure are important for understanding the general principles of myosin movement, the limitations of crystallography using myosins block our ability to observe the states that are most relevant to its physiological activity. These limitations are the inability to observe myosin in the presence of F-actin and the inability to capture myosin binding to its transiently bound substrates.

The function of myosins as motor proteins is due to their ability to translocate relative to actin filaments. Aside from their ability to bind actin, this means they must be capable of producing directional motion. This is achieved by a conformational change known as the

"power-stroke" which follows the release of inorganic phosphate from the nucleotide-binding pocket after ATP hydrolysis[55, 77-79]. This movement swings the lever arm through 60 to 70 degrees of rotation with respect to the motor domain to produce a directional translocation of the motor domain and its attached actin filament with respect to the thick filament-associated carboxy-terminus[76]. The size of each "step" of this motor action for muscle myosin II proteins is on the order of 5 nm, generating a force on the order of a few pN[80, 81].

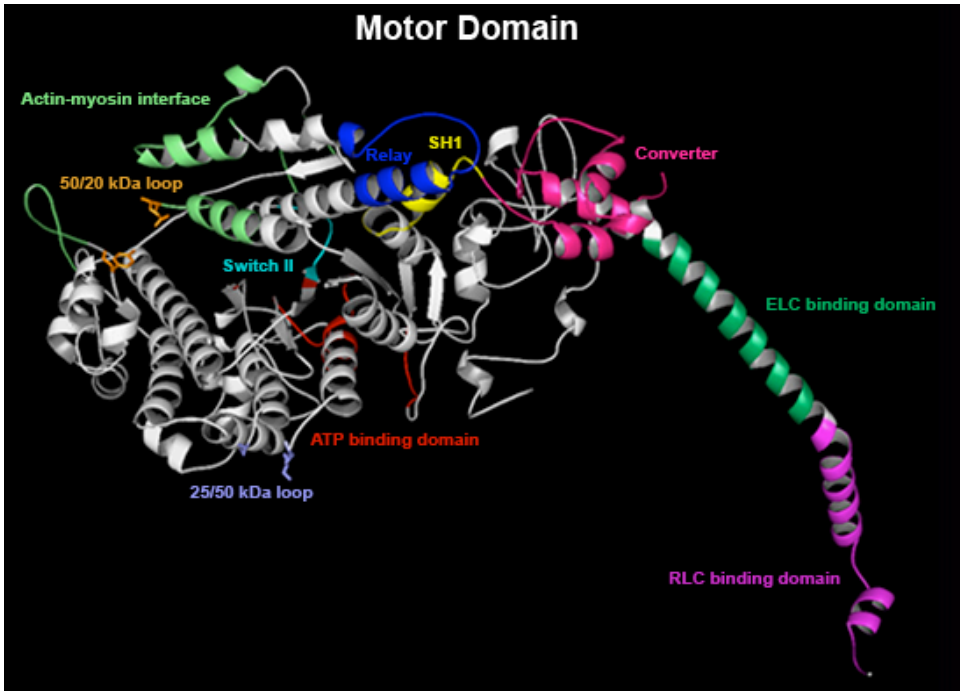

Figure 7: Structural domains of MyHC subfragment 1. MyHC subfragment 1 (S1) contains the minimal functional motor of myosin. This includes the motor domain and myosin light chain binding lever arm. Within the motor domain several functional domains operate in a closely coordinated manner, including the actin binding, ATP binding, and converter domains. The motor domain can be broken down into subdomains of 50 kDa, 25 kDa, and 20 kDa by proteolytic cleavage, as these subdomains are joined by solvent exposed loops: the 25/50 kDa loop associated with the ATP binding domain and the 50/20 kDa loop associated with the actin binding domain. Additional structures, such as switch II, SH1 and the relay helix, are known to play roles in intramolecular communication between functional domains. Adapted from (http://bmf.colorado.edu/myomapr/help.psp).

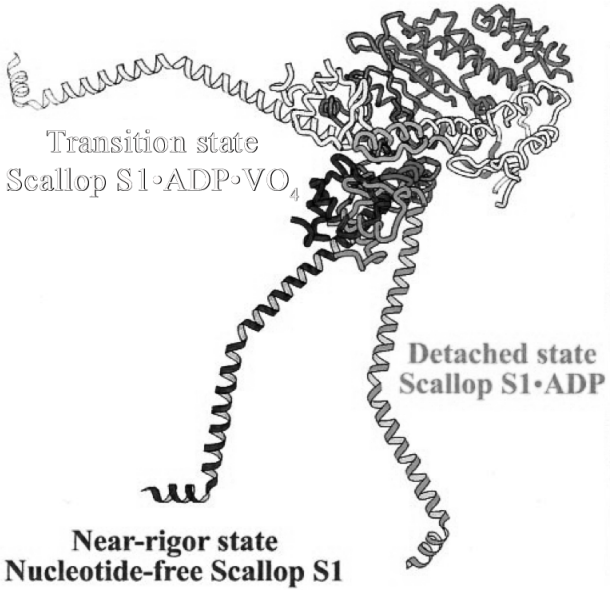

Figure 8: Three structural states of S1. MyHC S1 from scallop muscle has been crystalized and its structure solved in three conformational states. The three states, captured in the presence of three different nucleotide pocket contents, represent the positions of the lever arm in pre- and post-power-stroke conformations. The swing of the lever arm through 60 to 70 degrees of rotation with respect to the motor domain produces movement of the thick and thin filaments relative to one another. Adapted from Houdusse, et al. (2000) Three conformational states of scallop myosin S1[3].

Disease-causing mutations in myosin genes

Mutations in sarcomeric genes have been known to lead to human cardiac and musculoskeletal diseases since before 1990, when the first mutation leading to familial hypertrophic cardiomyopathy was localized to the cardiac β-MyHC gene[82]. In the time since that discovery, more than 300 mutations leading to numerous skeletal and cardiomyopathies have been identified in β-MyHC alone (regularly updated at http://bmf.colorado.edu/myomapr).

Disease-causing mutations occur in five of the human myosin II heavy chain isoforms. These are the cardiac isoforms α and β, the developmental isoforms embryonic and perinatal, and the fast skeletal isoform IIa. Mutations in the cardiac isoforms α and β have been found to cause cardiac diseases, such as hypertrophic and dilated cardiomyopathies[83-85], and since β myosin is also a major component of slow skeletal muscle, mutations in it also cause myosin storage myopathy and Laing distal myopathy[86, 87]. Mutations in the developmental isoforms embryonic and perinatal have been found to cause the distal joint contracture disorders, Freeman-Sheldon Syndrome, Sheldon-Hall Syndrome[88], and Carney complex[89]. A mutation in

the myosin IIa gene has been shown to cause an inclusion body myopathy[90]. The majority of these mutations are single missense mutations, indicating that even subtle changes to the structure of MyHC can have dramatic effects on the function of the contractile system.

Some of these disorders can also be caused by mutations in other members of the contractile machinery. In the case of hypertrophic cardiomyopathy, the disease can be caused by mutations in many sarcomeric genes[84]. Dilated cardiomyopathy can be caused by mutations in sarcomeric genes as well as in other non-sarcomeric muscle specific systems[83, 85]. Sarcomeric machinery mutations known to cause hypertrophic cardiomyopathy have been identified in troponin I, troponin T, troponin C, tropomyosin, actin, myosin binding protein-C, myosin essential light chain and myosin regulatory light chain genes in addition to MyHC isoforms α and β[83-85]. This disease is therefore a complex cellular disease that can be caused by disruption of the contractile machinery.

In other cases, however, this diversity of disease-causing genes is not present. In the cases of the developmental and skeletal myopathies, including the joint contracture and inclusion body myopathies, all mutations leading to these disorders that have so far been identified are in MyHC genes. This dichotomy indicates that the specifics of the type of disruption to contractile activity must in some important way differ between these disease types. It is therefore of great interest to seek to understand the contractile disruptions caused by such mutations.

Genetic models for studying myosin function.

Genetic approaches in the model organisms *Caenorhabditis*[91, 92], *Dictyostelium*[93, 94], *Drosophila*[95, 96], and *Mus*[97] have been used to study the role of myosins in intact organisms. By several methods MyHC genes have been inactivated in each organism to study their function. In *C. elegans* and *Drosophila*, genetic screens have been used to study the inactivation and

mutation of muscle myosin genes. Inactivation of each of the two body wall myosins in *C. elegans* has been shown to cause uncoordination or lethality[98, 99]. Null mutations in the MyHC gene of *Drosophila* cause a flightless phenotype[100]. In *Dictyostelium* homologous recombination approaches have been used to study the inactivation of myosin genes as well as to study structure-function relationships in specific regions of the myosin motor domain. These studies demonstrated that MyHC genes play a vital role in development as well as adult biology. These invertebrate and amoeboid model organisms have few MyHC genes and vastly different muscle biology from humans.

Murine muscles are far more similar to human muscles than invertebrate or amoeboid cells and possess the same complement of striated muscle MyHC II isoforms. Genetic inactivation of mouse cardiac MyHCs was lethal[101-103], but knockouts of two fast isoforms, IIb and IId, produced numerous muscular and growth defects in mice[50, 103-105]. Interestingly, in knockouts of a MyHC that made up the majority of MyHC in that muscle, the total myosin content of the muscles was not reduced[50, 104]. Therefore in the absence of particular myosin isoforms, muscle cells can compensate by expressing more of other isoforms[103, 104].

Recombinant expression of striated muscle myosins

Biochemical studies of MyHC proteins are of great interest in the field of muscle biology given the central role of MyHC in contraction. Classical methods of protein isolation from muscle are limited, however, by the mixed and varied nature of the MyHC composition of muscle fibers. For that reason, few studies of relatively pure single isoforms have been available until recently. In the few cases where nearly pure single isoform populations of MyHC could be isolated, the single fiber nature of the experiments posed significant limitations on protein quantity, constraining experiments to extremely efficient, but also extremely limited, techniques

such as flash photolysis and single molecule studies[106-109]. Separation of mixed isoforms has been similarly impractical due to the large size of myosin and biochemical similarity among the isoforms.

A system capable of producing recombinant striated muscle MyHC proteins would alleviate these limitations as well as allow the production of mutated versions of the protein to study pathogenesis. Expression was attempted in traditional recombinant expression systems including both bacterial and eukaryotic cells for many years with no success, yielding only inactive, misfolded myosin motor domains. Interestingly, active recombinant smooth muscle myosin II isoforms can be produced in SF9 insect cells using baculovirus as an expression vector[110].

The mapping of an "uncoordinated" mutant in *C. elegans* led to the identification of a unique set of chaperones necessary for the proper folding of myosin motor domains. Unc-45 and its mammalian homologues, Unc-45A and Unc-45B, were shown to be necessary but not sufficient to recover MyHC activity in recombinant expression systems[111-118].

One solution that circumvented some of these limitations was the production of rodents expressing transgenic MyHC in cardiac muscle. This approach also had the capability of producing mutant MyHC proteins and could yield nearly pure fibers. However, because the myosin composition of rodents and humans is different, mutations in different mouse myosin backgrounds were found in certain cases to produce opposing molecular phenotypes: hyperactive or hypoactive by steady-state biochemical tests[97, 119]. For this reason it is necessary to use the appropriate human background, and appropriate isoform, to properly analyze motor function and the effects of mutations therein. As human tissue samples are a rare source for both wild-type and mutant muscle proteins, recombinant approaches are required to carry out such work.

Winkelmann and colleagues pioneered the use of mouse myotubes differentiated from C_2C_{12} mouse myoblasts as an expression platform for recombinant MyHC proteins. They observed that differentiated C_2C_{12} lysates aided the folding of MyHC *in vitro*[117]. As C_2C_{12} cells possess the intrinsic ability to properly fold endogenous myosin proteins, this group developed a system wherein myotubes grown in culture and infected with recombinant adenoviruses encoding MyHC-S1 under the transcriptional control of a constitutive cytomegalovirus (CMV) promoter could produce active and properly folded recombinant MyHC[117, 118]. Work in the Leinwand lab optimized this system for the over-expression of human MyHC S1 proteins. Using poly-histidine tags encoded into terminal ends of the recombinant proteins, various forms of all eight MyHC subfragments have been successfully purified using traditional chromatographic purification techniques in quantities sufficient for biochemical[1, 2] and even crystallographic studies of human β-MyHC (PDB ID: 4DB1, manuscript in preparation).

The recent emergence of this technique for producing active recombinant human myosin subfragments has enabled studies to address several questions that had previously been inaccessible. The studies presented in this thesis address the following questions:

1. How are the various MyHC isoforms functionally specialized for the demands of their contractile environments?
2. What are the functional characteristics of human α-MyHC, and how do they differ from those of human β-MyHC?
3. How do pathogenic mutations in MyHCs alter their functional properties?

CHAPTER I

Human skeletal muscle myosin isoforms are functionally diverse.

INTRODUCTION

Human skeletal muscles are composed of mixtures of diverse fiber types[55]. These mixtures of fibers cooperate to produce contractile activities tuned to the functional demands on the muscle. For example, muscles requiring rapid contraction with relatively low load such as the extensor digitorum longus are composed almost entirely of fast, type II fibers, while slow postural muscles such as the soleus contain a large number of slow, type I fibers[55]. Fast versus slow and type II versus type I, are so named because of their differences in metabolism and shortening velocity[55, 120]. These differences, in turn, correlate with differences in the expression of elements of the contractile apparatus.

Both shortening velocity and force generation are key characteristics in a muscle's adaptation to its contractile role. Muscle fibers with high maximal rate of fiber shortening under the zero load conditions common to fast-twitch muscles such as the extensor digitorum longus are particularly adapted to this environment where low-force contraction is the norm. However, to maintain force, such fibers must twitch at high frequency, using a proportionally higher metabolic load[121]. These fibers would therefore not be well-suited to the contractile environment of slow-twitch postural muscles such as the soleus, where load-bearing conditions require sustained force. Slow, type I fibers, however, are well adapted to this contractile environment. They operate very efficiently to generate and maintain force during low-frequency experimental activation by both shortening and relaxing each contraction more slowly[121, 122]. Under load-bearing conditions the ability of muscle fibers to efficiently maintain force is beneficial in their

contractile role. In this manner, different contractile environments are characterized by muscle fibers with distinct contractile features.

MyHC proteins play a central role in determining the contractile properties of muscle fibers. The MyHC isoform composition of muscle fibers is highly correlated with maximal shortening velocity[120, 123] and force generation[124, 125]. While a wealth of factors are present in and around the contractile machinery in muscle cells to participate in activating or regulating contraction, it is unsurprising that MyHC identity should play a key role in muscle contraction, as it is the sole motor element in the sarcomere. It is therefore of interest to the field of muscle biology to understand how the functional diversity of MyHC isoforms contributes to the ability of muscles to meet the demands of the various contractile environments in which they function.

MyHC provides the ATPase activity of myosin. This ATPase activity is magnesium-dependent, as the nucleotide-binding site of MyHC coordinates a Mg^{2+} ion, which is associated with stabilizing the phosphates of ATP, and is thereby necessary for ATP hydrolysis[126]. Myosin hydrolyzes ATP into ADP and P_i and releases the two products coupled to its contractile activity. The dependence of myosin motor activity on the production of ATP-hydrolysis products means the ATPase activity of myosin can be experimentally coupled to the movement of actin filaments. Classical measures of MyHC activity include *in vitro* motility, where fluorescently labeled actin filaments can be microscopically observed to crawl across slide coverslips coated in myosin oriented with their motor domains away from the surface, in the presence of ATP[1, 127]. The rates of filament movement in this assay reflect the ability of the myosin to contract sarcomeres *in vivo* and tend to correlate with the other measures of myosin ATPase activity[1].

Other classical measures of myosin's ATPase activity use the measurement of product formation (ADP or P_i) over time. This activity is highly dependent on myosin's binding partner

for contractile functions in the sarcomere, filamentous actin (F-actin). ATPase activity has been measured in various experimental environments, such as muscle fibers[128], isolated myofibrils[129, 130], and purified MyHC proteins[1]. Whole muscle fibers, chemically permeabilized to allow for manipulation *in vitro*, have the benefit of representing the physiologically relevant environment of the function under study, but are complex systems with multiple reactions contributing to the products being measured. Also, the time scale of chemical diffusion into fibers limits the time resolution possible for measuring reactions in whole fibers[128, 129]. For these reasons fibers are a poor medium in which to study myosin. Myofibrils, the contractile organelles isolated from fibers[131], represent a simpler experimental system than whole fibers. Myofibrils, formed of many end-to-end linked sarcomeres, possess all the essential mechanical components required to study contraction. Additionally, with myofibrils it is possible to perform parallel biochemical and microscopic experiments to correlate biochemical activities with physical contractile changes, such as sarcomere length[129]. However, the presence of the regulatory structures on the thin filament (e.g. the troponin-tropomyosin complex) obscures the activity of myosin with additional variables affecting the ATPase rate. For these reasons, myosin ATPase experiments have most commonly been performed on isolated MyHC proteins.

The role of ATP in myosin activity is coupled to the contractile cycle of myosin with F-actin, shown graphically in Figure 9. In the absence of ATP, myosin binds F-actin strongly and stably. The addition of ATP to this complex induces a conformational change in myosin, which leads to dissociation of the complex. Following dissociation, a series of events follows: myosin hydrolyses ATP to ADP and P_i, returns its lever arm to the pre-power-stroke angle, binds to F-actin, and releases P_i, activating the power-stroke. The subsequent release of ADP returns myosin to the original complex[76-78] (Figure 9). In the absence of F-actin the events following

ATP-hydrolysis are interrupted, yet similar events with respect to the conformation of the myosin motor domain are thought to occur to complete the cycle in the absence of F-actin. This leads to "basal" ATPase activity, but this basal cycle is known to be far slower than F-actin-activated ATPase activity[1, 132-134].

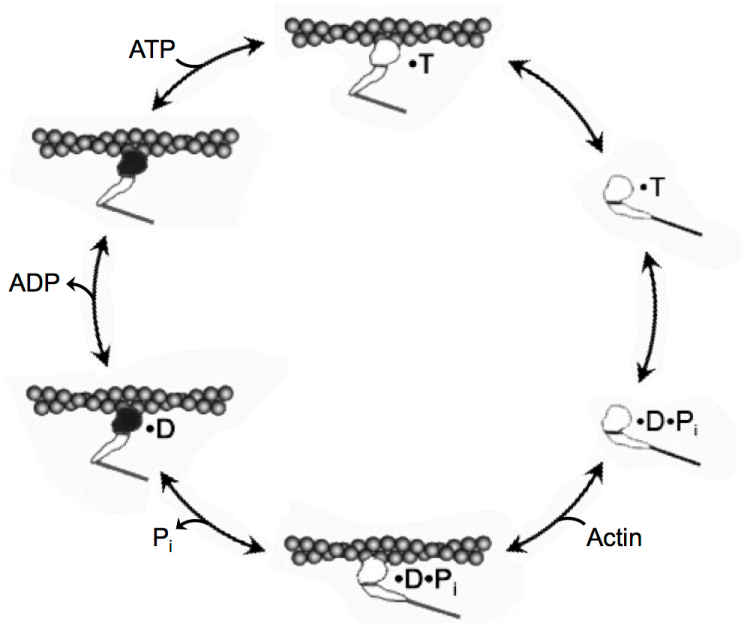

Figure 9: F-actin-myosin ATPase cycle. The F-actin-activated myosin ATPase cycle hydrolyzes one molecule of ATP to ADP and P_i per turnover of the cycle, per myosin motor domain. The formation of a crossbridge, then release of these two products and the binding of another ATP molecule during the crossbridged phase of the cycle (black myosin motor domains) must precede further steps of hydrolysis. The rate-limiting step of the cycle in F-actin-activated ATPase reactions has been determined to be in the detached state (white myosin motor domains) and defines k_{cat}. Substrates are abbreviated as follows: ADP (D), ATP (T), and inorganic phosphate (P_i).

In this way, myosin requires F-actin, its crossbridge partner in the sarcomere, to perform its role in physiological contraction. ATPase measurements therefore exist in two categories: basal ATPase, measured in the absence of F-actin, and F-actin-activated ATPase. Basal ATPase activity is simple to measure, but is not informative with regards to muscle contraction, as it occurs in the absence of the crossbridge. F-actin-activated ATPase activity follows the physiologically relevant reaction steps for muscle contraction, but is more difficult to measure as

the reaction is complicated by the highly viscous nature of F-actin in solution. Traditional methods also typically measure such activity at lower than physiological temperature, due to the constraints of the lab environment and protein longevity at higher temperatures. In previous work in the Leinwand lab, Daniel R. Resnicow developed a system to overcome these limitations, using a Reacti-Therm heating and stirring module [Pierce] to constantly mix reactions in microcentrifuge tubes at 37° C. The work described in this chapter on the steady-state ATPase measurements on MyHC isoforms IIa, IId, IIb, embryonic, perinatal, extraocular, and β was carried out collaboratively with Dr. Resnicow when he was a graduate student and resulted in Resnicow et al. (2010)[1].

Measurements of ATPase activity follow a slightly varied form of traditional enzyme kinetics. Traditional Michaelis-Menten kinetics concerns the direct relationship between enzymes and substrates. In the F-actin-activated ATPase assay, the substrate enzymatically operated upon by myosin is ATP, but instead of reaction rates being measured over a range of ATP concentrations, from limiting to saturating, ATP concentration is held constant and in excess throughout the set of reactions and instead the concentration of the binding partner and activator, F-actin, is varied. When rates of product formation are plotted with respect to F-actin concentration and the data fit by non-linear regression using the Michaelis-Menten equation, the traditional constants, V_{max} and K_M, can be determined. The traditional definitions of these constants are: V_{max} = the rate of the reaction at saturating substrate concentration and K_M = the concentration of substrate that produces $V_{max}/2$. In the F-actin-activated ATPase assay the traditional definition of V_{max} remains accurate, though it would be more correct to describe it as: the rate of the reaction at saturating ATP in the presence of saturating F-actin. Because F-actin-activated ATPase rates are plotted with respect to the activator, F-actin, rather than to the

catalytic substrate, ATP, the K_M value is an unusual form of Michaelis constant. In this case the relationship differs because it refers to the concentration of a cofactor, not to the catalytic substrate. It is unclear in our model of the reaction to which step or steps of the ATPase cycle this constant should relate. This constant is referred to herein as K_{ATPase}[135, 136].

Steady-state ATPase reactions are governed by two additional factors that are not obvious *a priori*. First, the reaction conditions must be ~10-fold lower than physiological ionic strength (14 mM versus ~150 mM), as ionic strength influences F-actin-myosin affinity *in vitro* such that kinetic differences between isoforms become indistinguishable[137]. Second, the rate-limiting step under the reaction conditions *in vitro* does not necessarily reflect what factors limit the rate of actin-myosin interaction in activated sarcomeres. In an activated sarcomere, the geometry of the filaments governs the rate of the transition from unbound to crossbridged for an individual myosin, but *in vitro* this constraint is not present[2, 55, 79, 136, 138-140]. While these facts indicate that there are limitations in the relationship of *in vitro* ATPase data to the intact physiological system, relative comparisons of isoforms measured in the same manner and under the same conditions may still be valuable.

The subject of this chapter is the comparative analysis of the seven human skeletal muscle MyHC isoforms, IIa, IId, IIb, embryonic, perinatal, extraocular and β, by their F-actin-activated ATPase activity. This study was performed by producing and purifying recombinant human MyHC-S1 proteins, then testing their F-actin-activated ATPase activities using an enhanced form of the traditional assay.

METHODS

Production of recombinant MyHC

Using the recombinant adenovirus construction system, the pAdEasy kit [Qbiogene], expression cassettes were constructed encoding S1 fragments of human MyHC isoforms under the transcriptional control of a CMV promoter[141]. The AdEasy system is designed to produce replication-deficient adenovirus, with exogenous expression constructs encoded into the E1 locus of the viral genome under the transcriptional control of a CMV promoter (depicted graphically in Figure 10A). MyHC-S1s were constructed as soluble fragments analogous to the subfragment produced by papain digestion of MyHC, spanning methionine-1 through proline-838 with respect to the human β-MyHC sequence. These subfragments were encoded as fusions with enhanced green fluorescent protein (eGFP) at their carboxy termini, followed by a 6xHistidine tag for affinity purification (depicted graphically in Figure 10B). The eGFP fusion to the carboxy termini of MyHC-S1 proteins was designed initially to allow these proteins to be used in collaboration with the Spudich lab at Stanford in *in vitro* motility experiments, where antibodies to eGFP could be used to anchor MyHC-S1 proteins to glass coverslip surfaces with a defined, motor domain "up," orientation, but also acted to aid in the initial development of the expression system to provide a visual indication of protein expression in live cultured cells.

Human MyHC subfragments were amplified from human cDNA by PCR and subcloned into the multiple cloning site of pShuttle-CMV plasmids downstream of the CMV promoter. pShuttle plasmids were then linearized by digestion with PmeI [New England Biolabs] and transformed into competent BJ5183 bacteria containing the replication-deficient adenoviral genome plasmid pAdEasy. The pShuttle expression cassette inserted into the E1 region of pAdEasy by homologous recombination. After confirming successful recombination by

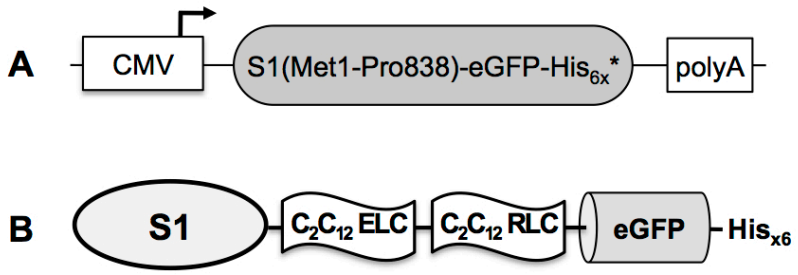

Figure 10: Constructs for expression of recombinant human skeletal muscle S1 proteins. ***A.*** S1 isoforms spanning residues methionine-1 through proline-838, with respect to human β-MyHC are cloned into pShuttle plasmid in frame with eGFP-6xHistidine-Stop (*), under transcriptional control of a CMV promoter and upstream of a polyA signal sequence. ***B.*** The proteins produced by this expression cassette consist of S1 fused at its carboxy terminus with eGFP and a 6xHistidine-tag. These proteins copurify with myosin light chains (ELC and RLC) endogenous to the C_2C_{12} cells in which the protein is expressed.

restriction digestion and gel electrophoresis, pAdEasy DNA was produced in bacteria and isolated. Isolated pAdEasy DNA was linearized by digestion with PacI and purified by phenol-chloroform extraction. Linearized DNA was transfected into human epithelial kidney (HEK293) cells expressing E1 to complement viral replication, then allowed to produce and replicate viral particles until plaques were visible in the cell monolayer. Freeze-thaw cycles were used to liberate viral particles from cells, then clarified lysates applied to larger quantities of cells in escalating cycles until sufficient quantities of virus were available for purification.

Each recombinant adenovirus was purified using a two-step cesium chloride (CsCl) gradient. First, the clarified lysates were applied over the top of a step gradient consisting of 1.25 g/mL over 1.4 g/mL CsCl. Gradients were centrifuged in an SW40 rotor [Beckman] at 230,000 x g for one hour, then viral bands were isolated from above the CsCl step by side-puncture of the centrifuge tubes with a syringe. These initial bands were then transferred to heat-seal tubes and the tubes filled with 1.35 g/mL CsCl, sealed, then centrifuged for at least two hours in a VTi65 rotor [Beckman] at 400,000 x g. Viral bands were isolated from heat-sealed tubes, dropwise from bottom-punctures, then diluted 1:5 in glycerol storage buffer for storage at

-20° C.

Expression of recombinant MyHC was achieved by infection of myotubes derived from C_2C_{12} myoblasts with purified recombinant adenoviruses. C_2C_{12} myoblasts were cultured in Dulbecco's Modified Eagle Media (DMEM) supplemented with 10% fetal bovine serum (FBS), 100 units/mL penicillin and 100 µg/mL streptomycin [Gibco]. Cells were split at ~50% confluency. Once sufficient cell quantities were obtained, cells were allowed to grow to 100% confluency. Once confluent, the myoblasts were differentiated into myotubes by changing the medium to DMEM supplemented with 2% horse serum (HS) and penicillin/streptomycin. After two days in HS, the cells exhibited the classical morphological characteristics of skeletal muscle fibers, becoming elongated and multinucleate, and were then infected with 10^6 to 10^8 plaque-forming units (pfu) of adenovirus per 100-mm Petri dish. Infected cells were allowed to grow for three to four days before collection for MyHC purification.

Purification of recombinant MyHC-S1 proteins

The purification of recombinant MyHC subfragments was performed initially using freshly cultured myotubes after three to four days of infection. Using this approach, 25 to 50 100-mm Petri dishes of confluent myotubes, all infected with a given recombinant adenovirus, were scraped directly into chilled lysis buffer: 50 mM Tris HCl, pH 7.0, containing 20 mM imidazole, 100 mM NaCl, 0.5% Tween-20, 1 mM DTT and 1x protease inhibitor cocktail [Roche]. Cells were then lysed mechanically in a Dounce homogenizer and the lysate cleared by centrifugation in a Ti50 rotor [Beckman] for two to three periods of 15-minutes at 80,000 x g, transferring supernatants to fresh tubes between centrifugal steps. Clarified lysates were brought to 0.5 M NaCl by adding ~1/10th volume of 5 M NaCl to match buffer conditions for the next step of purification.

Fast Protein Liquid Chromatography (FPLC) was used for purification of recombinant MyHC-S1 proteins. As previously described, these proteins were designed to carry carboxy terminal 6x histidine tags. Poly-histidine tagged proteins have been shown to bind nickel resins and release by competition with high concentration imidazole solutions[142, 143]. Using an AKTApurifier FPLC system [GE Healthcare] with a 1 mL HisTrap HP nickel-Sepharose column [GE Healthcare], S1 proteins were isolated from clarified cell lysates. FPLC steps were carried out at a flow rate of 1 mL per minute in a temperature controlled environment at 4° C. HisTrap HP columns were equilibrated to running buffer before use by flowing 10 column volumes of running buffer, followed by stripping the columns with 5 column volumes of 1 M imidazole stripping buffer and re-equilibrating with 10 column volumes of running buffer. Lysates were loaded onto equilibrated columns using a running buffer of 50 mM Tris pH 7.0, containing 20 mM imidazole, 500 mM NaCl, 0.05% Tween-20 and 1 mM DTT. An additional 10 column volumes of running buffer was used to wash out unbound materials. More stringent wash steps were then applied, using 10 column volumes of 30 mM imidazole wash buffer, and then 10 column volumes of 50 mM imidazole wash buffer to eliminate non-specific binders. Elution of S1 proteins was performed in 5 column volumes of elution buffer (50 mM Tris pH 7.0, containing 350 mM imidazole, 500 mM NaCl, 0.05% Tween-20 and 1 mM DTT). The 5 mL elution was collected in 1 mL fractions. The MyHC S1 peak was uniformly found in fractions 2 through 4. These fractions were pooled and dialyzed overnight at 4° C into a low salt buffer: 25 mM imidazole, pH 7.0, containing 10 mM KCl, 4 mM $MgCl_2$, and 1 mM DTT, in preparation for anion-exchange chromatography.

After dialysis and centrifugation at ~14,000 x g to remove precipitates, eluates were subjected to anion-exchange chromatography. HiTrap Q HP 1 mL Sepharose anion-exchange

columns [GE Healthcare] were equilibrated in running buffer: 25 mM imidazole, pH 7.0, containing 1 mM DTT, in the same manner as described previously, using 10 column volumes of running buffer, followed by 5 column volumes of stripping buffer: 25 mM imidazole, pH 7.0, containing 1 M NaCl and 1 mM DTT, and then re-equilibrating with 10 column volumes of running buffer. Dialyzed eluates were loaded onto equilibrated columns and an additional 10 column volumes of running buffer was used to wash out unbound sample. Elution was carried out using a linear gradient from 0 to 1 M NaCl over 20 column volumes. Fractions were collected in 1 mL aliquots. S1 proteins typically eluted at ~300 mM NaCl, then were dialyzed overnight into reaction buffers differing depending on the assays to be performed. Concentrations were determined by absorbance at 280 nm using the calculated extinction coefficient 94000 $cm^{-1}M^{-1}$ (based on the Eldehoch model of estimating the contributions of tryptophan, tyrosine, and cysteine to the absorbance at 280 nm[144]).

Recent collaborations with the Rayment lab at the University of Wisconsin at Madison to crystallize the human β motor domain necessitated devising a method for the collection and long-term storage of materials such that large amounts of the protein could be purified in a single batch. Thanks to the contributions of Dima Kenchin of the Rayment lab and Ariana Combs in the Leinwand lab, this was accomplished by the collection of three to four day infected cells by trypsinization off their culturing surfaces, followed by washing and pelleting in the presence of 0.2% Pluronic® F-68 [Sigma], a polyoxyethylene-polyoxypropylene block copolymer, commercially sold to stabilize cell membranes against shearing and freezing damage. These pellets were flash frozen in liquid nitrogen and stored at -80° C. After thawing pellets in lysis buffer and continuing with purification as described above, proteins isolated from these frozen pellets were found to retain all activity with no apparent loss in yield.

ATPase assays

Concurrent with development of the system for over-expression and purification of MyHC-S1 proteins, existing biochemical methods for confirming and characterizing their activity were refined by Daniel R. Resnicow in the Leinwand lab. Measuring the cyclical ATPase activity of these soluble motor fragments at steady-state was possible *in vitro* using methods adapted from those published by Kathleen Trybus[145]. Basal ATPase activity, the cyclical hydrolysis of ATP by S1, independent of actin, is very slow relative to the actin dependent cycle. Basal ATPase activity was measured by mixing 25 μg/mL S1 with saturating 3 mM ATP in low-salt buffer: 4 mM imidazole, pH 7.0, containing 10 mM KCl, 4 mM $MgCl_2$, 1 mM NaN_3, and 1 mM DTT in a Reacti-Therm heated stirring module [Pierce] and quenching aliquots at 1- to 5-minute timepoints into denaturing stop-solution containing 60 mM EDTA, pH 6.5, and 6.6% SDS. Appropriate time courses were determined for each isoform to establish conditions that would be within detection limits and would not significantly alter substrate concentration. Inorganic phosphate (P_i) was quantified at each time point using an ammonium molybdate based colorimetric assay as described previously[145].

F-actin-activated ATPase was measured similarly with the additional presence of purified chicken filamentous-actin (F-actin), which was prepared as described previously by Pardee and Spudich[146]. S1 protein (5 μg/mL) was first mixed with F-actin (0 to 100 μM), then mixed with saturating 3 mM ATP. At specific timepoints between 20 seconds and 2 minutes, depending on the isoform, aliquots were quenched by 1:1 mixing with stop-solution. Four timepoints, including a zero-timepoint, were taken for each reaction condition and the P_i concentration at the zero timepoint was subtracted from each to remove the background concentration. To determine more physiologically relevant rates, ATPase assays were performed at 37° C. Reactions were

performed in duplicate and on multiple biological replicates (biological replicates are herein defined as separate protein preparations).

RESULTS

Production and purification of recombinant MyHC subfragments

Functional recombinant striated muscle MyHC motor domains have historically been difficult to produce due to the absence of muscle-specific cofactors from traditional cell types used for protein expression[114-118, 147]. MyHC-S1 protein was produced for this study by infection of mouse myotubes in culture with recombinant, replication-deficient adenoviruses expressing human MyHC subfragments, using a system developed based on the work of Don Winkelmann and colleagues[111].

Previous work in the Leinwand lab has shown that transfection of differentiated mouse myotubes was not suitable for this purpose due to the inefficiency of transfection. While C_2C_{12} myoblasts are readily transfectable, they do not express the muscle-specific cofactors required for the proper folding of the myosin motor domain. Therefore, for this study recombinant adenoviruses were produced to insert MyHC expression cassettes into myotubes. Adenoviral vectors readily infect mammalian cells and are effective for infecting both myoblasts and myotubes regardless of differentiation state. As such, adenoviruses are suitable for inserting DNA into mouse myotubes.

Using methods as described above, MyHC-S1 proteins were produced and purified for the human skeletal muscle MyHC isoforms IIa, IId, IIb, embryonic, perinatal, extraocular, and β. A representative SDS-PAGE gel for two purified MyHC-S1 proteins is shown in Figure 11. As noted, extraocular-S1 protein does not appear to have light chains associated with it, most likely

because C_2C_{12} cells do not express extraocular light chain isoforms. Embryonic-S1 protein variably copurified with myosin light chains. The other five MyHC-S1 proteins copurified with bands of the appropriate size for mouse ELC and RLC isoforms: 18 kDa, 22 kDa, and 25 kDa (Figure 11, lane A; data not shown). Copurified myosin light chains were identified by mass spectrometry [UCHSC Proteomics Core] as a mixture of four light chain isoforms: alkali myosin light chain 1 (MLC1F), regulatory myosin light chain 2 (MLC2F), alkali myosin light chain 3 (MLC3F), and myosin light chain 1, atrial/fetal isoform (MLC1A).

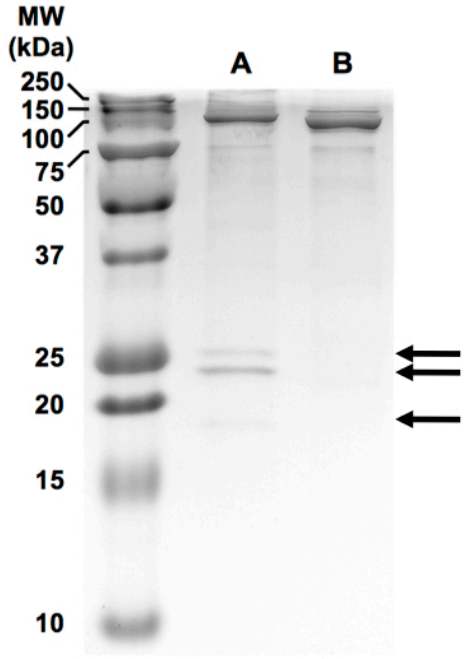

Figure 11: Purified recombinant human skeletal muscle S1 proteins. eGFP-tagged S1 proteins are ~125 kDa and the majority copurify with light chains endogenous to the C_2C_{12} cell expression system, as seen at between ~18 and 25 kDa for MyHC-S1 IId in lane **A** (indicated by arrows). Not all isoforms carried detectable amounts of light chains. In the cases of embryonic and extraocular, it appeared that no light chains were present, as seen for extraocular MyHC-S1 in lane **B**.

Measurements of steady-state F-actin-activated and basal ATPase activity.

ATPase activity was quantified by measuring the concentration of P_i product in each quenched ATPase reaction aliquot. P_i quantification was accomplished using the colorimetric assay described by Kathleen Trybus[145], and comparison to a standard curve of known phosphate concentrations. For each concentration of F-actin, the rate of P_i production was calculated from the four reaction timepoints. These values were divided by the concentration of S1 to yield units of s^{-1}. Reaction rates were plotted with respect to F-actin concentration and the resulting

saturation curves were well-described by fitting with the Michaelis-Menten equation:

$V_{obs} = \frac{V_{max}[S]}{K_M + [S]}$, which can be rewritten for actin-activated ATPase as:

Equation 1: $V_{obs} = \frac{k_{cat}[S1] \bullet [F-Actin]}{K_{ATPase} + [F-actin]}$,

where $K_{ATPase} = K_M$, to give calculated k_{cat} and K_{ATPase} values for each isoform (Figure 12).

F-actin-activated ATPase k_{cat} values from fitted functions ranged from the slowest, β-MyHC, at 18.9±1.5 s^{-1}, to the fastest, IIb, at 86.1±8.4 s^{-1}, giving a range of ~4.4-fold among the isoforms tested, with the group's mean value at ~55 s^{-1} (Table 2). K_{ATPase} values from the fitted functions ranged from the lowest, IIb, at 14.0±3.2 μM, to the highest, IIa, at 44.5±5.6 μM, giving a range of >3-fold, with the group's mean value of ~30 μM (Table 2). Basal ATPase activity, measured in the absence of F-actin, at saturating ATP gave rates ranging from the slowest, perinatal, at 0.04±0.03 s^{-1}, to the fastest, extraocular, at 0.12 s^{-1}, giving a range of 3-fold, with a group mean of ~0.08 s^{-1} (Table 2).

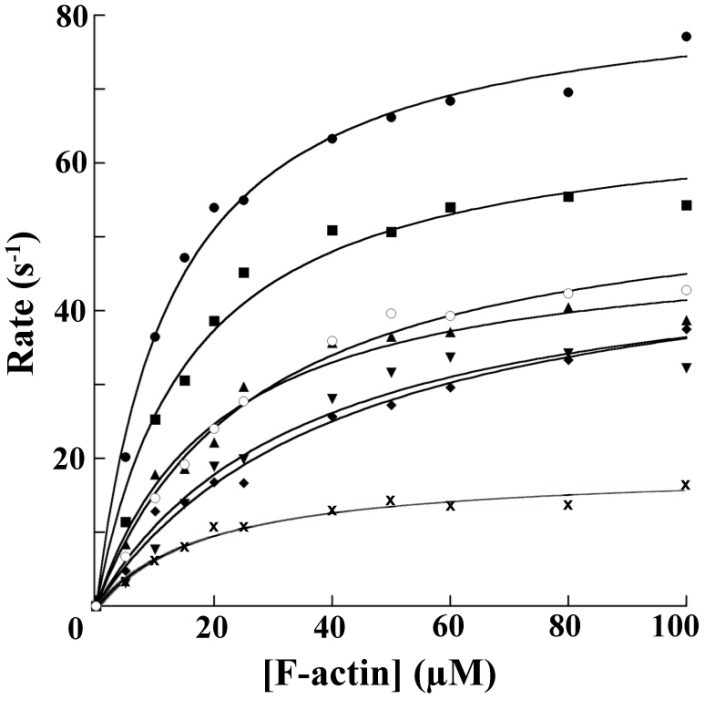

Figure 12: F-actin-activated myosin ATPase. Saturation curves plotted from F-actin-activated ATPase measurements and fit using Equation 1. Recombinant human MyHC isoforms are represented as: IIa (♦), IIb (●), IId (■), Embryonic (▼), Perinatal (○), Extraocular (▲), and β (**x**). Published in similar form in Resnicow, et al. (2010)[1].

	k_{cat} (s^{-1})	K_{ATPase} (μM)	k_{cat}/K_M ($s^{-1}\mu M^{-1}$)	Basal ATPase (s^{-1})	Fold F-actin activation (k_{cat}/basal)
IIb	86.1±8.4	14.0±3.2	6.15	0.08±0.02	1080
IId	65.7±2.1	15.7±1.3	4.18	0.11±0.01	597
IIa	52.8±4.4	44.5±5.6	1.19	0.08±0.01	660
Embryonic	41.2±3.7	35.1±1.8	1.17	0.08±0.01	515
Perinatal	59.7±4.9	41.2±3.7	1.45	0.04±0.03	1490
Extraocular	59.2±5.7	37.2±4.5	1.59	0.12±0.02	493
β-MyHC	18.9±1.5	18.7±4.8	1.01	*not determined*	*not determined*

Table 2: F-actin-activated myosin ATPase. Steady-state F-actin-activated MyHC-S1 ATPase was measured over a range of F-actin concentrations, from 0-100 μM. Calculated kinetic constants vary up to ~4.5-fold among the skeletal isoforms. The fastest isoforms, IIb and IId, both have low K_{ATPase} values, but the slowest isoform, β, also shares this feature. Understanding the diversity of this constant therefore may require measurements at the pre-steady-state level. Published in similar form in Resnicow, et al. (2010)[1].

DISCUSSION

F-actin is an activating cofactor of myosin ATPase activity

The ability of F-actin to greatly increase the rate of myosin ATPase activity over its basal levels represents a well-adapted regulation on passive ATP usage by muscles. While cellular ATP concentrations are thought to remain consistently high, binding sites for myosin on F-actin in the thin filament are not. In the sarcomere the troponin-tropomyosin complex on the thin filament blocks the interaction of F-actin and myosin in cells at rest. This means that independent of the concentration of the enzymatic substrate, the rate of catalysis can still be effectively regulated. The degree of activation by F-actin of ATPase activity over basal activity observed in this population of motors far exceeds the degree seen in previous studies of equivalent MyHC II proteins. In previous studies of myosin isolated from rabbit skeletal muscle and rat heart ventricle muscle the degree of F-actin activation of ATPase activity over basal

ATPase was found to be ~20-fold[148, 149]. In this study, basal ATPase rates were each determined to be between 0.04±0.03 s^{-1} (perinatal) and 0.12±0.02 s^{-1} (extraocular), which was activated to between 18.9±1.5 s^{-1} (β-MyHC) and 86.1±8.4 s^{-1} (IIb) at saturating F-actin. The degree of F-actin activation over basal ATPase in these human recombinant skeletal MyHC-S1 proteins is between ~500-fold (extraocular) and ~1500-fold (perinatal), far greater than the degree of activation observed previously in other studies.

While previous studies reported ~20-fold activation of ATPase by F-actin, this study found the F-actin-activation of ATPase over basal activity to be on the order of ~1000-fold. The source of this ~50-fold increase in the degree of F-actin-activation over previous studies of similar motors is likely due to the refinements in our ATPase assay method. In our study, ATPase is measured at physiological temperature (37° C) rather than the typical assay temperature of ~20° C[150] and with improved stirring methods using the Reacti-Therm stirring heatblock and a magnetic stirbar within each reaction tube[1]. One feature unique to the F-actin-activated ATPase assay and absent from the basal ATPase is the high viscosity of reactions containing high F-actin concentrations. By stirring reactions we have attempted to overcome the localized product buildup and substrate exhaustion that can occur in viscous reaction environments. The improved stirring methods of our system are likely to increase the apparent maximum reaction rates of F-actin-activated ATPase activity over those measured without stirring, but not the maximum rates of basal ATPase activity which are performed in the absence of F-actin and therefore are not in viscous conditions. We believe this to be the reason for the far larger increase in F-actin activation measured in this study over previous studies.

Functional diversity in the ATPase activities of the human skeletal muscle myosins

These data can be used to compare the relative activities of the human skeletal MyHC

isoforms. The k_{cat} values reflect a hierarchy among the skeletal isoforms in terms of relative activity, from faster to slower: IIb > IId > perinatal > extraocular > IIa > embryonic > β-MyHC. Among the fast skeletal isoforms, this hierarchy (IIb > IId > IIa) agrees with previously published data from both human and rodent muscle derived myosins[150-153]. The isoform found to have the highest ATPase rate, IIb, is prevalent in small, fast rodent muscles, while the slower isoform, IIa, is prevalent in larger, slower human muscles, reflecting the physiological appropriateness of these observations. This also supports the idea that the varied MyHC isoform compositions of muscles reflect specific adaptations to varied contractile demands.

The developmental isoforms, embryonic and perinatal, play a yet undetermined role in musculoskeletal development. Previous studies of their activity from chicken and rat tissues indicated that the steady-state activities of the developmental isoforms may be very slow[154, 155]. This leads to the idea that developmental isoforms may play only a passive role in the muscle, without contributing to contractile activity significantly[154, 155]. However, the existence of disease-causing mutations in the enzymatic site of both embryonic and perinatal MyHC[88, 89] indicate that their activity is vital to their role in the sarcomeres of developing muscles. These data indicate that in fact the ATPase activity of the human perinatal isoform is faster than that of the most abundant fast skeletal isoform in adult human muscles, IIa. Also, while the human embryonic isoform is slightly slower than IIa, it is still ~2.5-fold faster than the slow isoform, β-MyHC. The fact that these parameters for the developmental isoforms trend closely with the fast skeletal isoforms indicates that the developmental isoforms may be capable of contractile activity similar to that of the adult isoforms.

The slow, type I fiber isoform, β-MyHC, is predicted to be ~2- to 5-fold slower than the fast isoforms, from the relative maximum fiber shortening velocities of fast type II and slow type

I fibers[55, 156], as shortening velocity is correlated with MyHC isoform composition[49]. This prediction follows closely with the calculated k_{cat} values for the human skeletal isoforms where β-MyHC is measured to be 2.8- to 4.6-fold slower than the fast skeletal isoforms, IIa and IIb, respectively.

The extraocular isoform presents an unusual contrast to its anticipated activity level from the function of muscle fibers in which the isoform is found. Such fibers, from the muscles controlling movement of the eyes and the larynx, have been shown to possess among the fastest shortening velocities of any skeletal muscle fiber[157, 158]. However, the F-actin-activated ATPase activity of human extraocular-MyHC has a k_{cat} value very near the average of the skeletal isoforms, 59.2 s^{-1}. The specialization of the extraocular isoform may exist not in its steady-state activity as measured by ATPase, but rather in its pre-steady-state kinetics, as a rapid fiber twitch may only require a single reaction turnover to complete (see Chapter 2).

K_{ATPase} values, mathematically equivalent to K_M values and derived from the Michaelis-Menten fit to the data, are not simple to interpret, as the reaction step responsible for determining K_{ATPase}, as well as the rate-limiting step of the ATPase cycle, responsible for determining k_{cat}, may vary from isoform to isoform. Discussion of this constant in myosin biochemistry has historically focused around the crossbridge formation step and F-actin affinity as determining this constant[159]. If this interpretation is correct, then the results showing that both the fastest isoform by k_{cat}, IIb, and the slowest, β-MyHC, share among the lowest K_{ATPase} values, 14.0 and 18.7 μM, respectively, compared to a group mean of ~30 μM, could be explained by both isoforms binding F-actin with relatively high affinity, and β-MyHC possessing a far slower rate-limiting step following crossbridge formation. To test these hypotheses it is necessary to break down the ATPase cycle into its component reaction steps, as described in Chapters 2 and 4.

The ratio, k_{cat}/K_{ATPase}, is used to describe the catalytic efficiency of an enzyme at low substrate concentrations, where "perfect" enzymes will catalyze their substrates at an essentially diffusion limited k_{cat}/K_M of ~10^8 to 10^9 $\mu M^{-1}s^{-1}$ [160]. These myosins, while quite imperfect enzymes by this metric, show notable variability within this group. The two fastest isoforms by k_{cat}, IIb and IId, each have higher k_{cat}/K_M values of 6.15 and 4.18 $\mu M^{-1}s^{-1}$, respectively, while the rest of the isoforms group together with lower values between 1.01 and 1.59 $\mu M^{-1}s^{-1}$. The coupling of the higher k_{cat}/K_M values with the fastest two k_{cat} values may indicate that this metric has a degree of relevance to myosin activity, but it is unclear from these steady-state data what that relevance might be. Each of these differences found among the human skeletal muscle myosin isoforms are modest in scale, but indicate that there may be more to be learned from further study of these motors at pre-steady-state.

Refined F-actin-activated ATPase methods produce faster rates

It would be desirable to directly compare these results to existing studies in order to both establish the comparability of proteins from this recombinant expression system to those derived from animal muscles and to compare the isoforms in this study to their orthologs in previous studies. This is complicated by the fact that previous studies were performed primarily on muscles containing mixed populations of isoforms and were performed at varied reaction conditions. When the results of this study are compared to existing data from lower temperatures and without improved mixing techniques, they are universally higher than existing data. In the case of β-MyHC, existing F-actin-activated ATPase rates range from 6- to 60-fold slower[161-165]. This 10-fold range in the existing data exists even between experiments performed at the same temperature[163, 165]. Because of these inconsistencies in the existing literature, it is desirable to establish a universal set of reaction conditions for these studies. The improvements in detecting

V_{max} using the mixing techniques described in this study lend weight to its adoption in F-actin-activated ATPase studies more broadly.

While up to ~4.5-fold differences were observed using this metric, these steady-state measurements also disguise much of the potential diversity in contractile activity within summed events (Figure 9). Therefore elucidating the specific biochemical features from which these differences in product formation originate will require additional tests. Notably, this work describes the first ever kinetic measurements performed on recombinant human MyHC. This represents a significant step forward in the study of these motors, which until this point could essentially only be isolated from animal muscle sources. This technique expands the possibilities for study to the pure populations of single isoforms, to human isoforms, and to pathogenic mutant myosin proteins.

CHAPTER II

Pre-steady-state skeletal muscle myosin kinetics

INTRODUCTION

MyHC in adult skeletal muscles

As discussed in Chapter I, skeletal muscles express a wide variety of MyHC isoforms in distinct temporal and spatial patterns. In adults, IIa and IId are the primary MyHCs of human fast skeletal muscle fibers. Interestingly, IIb, which is very common in rodent fast fibers, is not expressed in healthy human muscles, yet it is known to be a functional motor[61]. The extraocular isoform is only found in fibers of a highly mixed isoform nature in muscles around the eye and larynx[62-64]. By steady-state measurements, the adult fast skeletal muscle MyHC isoforms, IIa, IId, IIb, and extraocular, cluster within a span of ~1.5-fold in terms of k_{cat} of F-actin-activated ATPase. These isoforms diverge somewhat in terms of K_{ATPase}. IId and IIb, with faster k_{cat} = 65.7 and 86.1 s^{-1}, respectively, had lower K_{ATPase} = 15.7 and 14.0 μM, respectively. IIa and extraocular, with slower k_{cat} = 52.8 and 59.2 s^{-1}, respectively had 2- to 3-fold higher K_{ATPase} = 44.5 and 37.2 μM, respectively (Chapter I, Table 2). These four isoforms can be considered as a group, representing the adult fast skeletal muscle MyHC isoforms. However, it is likely that this group possesses an additional degree of functional diversity in the steps that comprise the ATPase cycle, as these steady-state kinetic trends and the diversity of fast contractile fibers suggest. Using pre-steady-state methods it should be possible to elucidate additional functional diversity in this family of fast MyHCs.

Pre-steady-state reaction kinetics

Myosin undergoes a cyclical interaction with actin and ATP to contribute to muscle

contraction. In Chapter I this ATPase cycle of myosin was investigated at steady-state. Steady-state measurements are useful in that they represent a simple activity metric by which proteins can be compared. However, within the cycle of coupled reactions a large degree of functional diversity may be present that would not be possible to reveal by measurements at steady-state. The ATPase cycle is composed of numerous steps, each of which may differ in rate or substrate dependence among isoforms to produce different profiles of contractile cycle kinetics. To identify such functional differences within the ATPase cycle, the reactions that compose the cycle must be observed at pre-steady-state, before the cyclical activity of these reactions makes observation of any individual reaction impossible. The subject of this chapter is the pre-steady-state analysis of the reactions that compose the ATPase cycle for the MyHC isoforms of human adult fast skeletal muscles.

Biochemical reaction kinetics concerns the rates of interactions between enzymes and their substrates, which depend in part upon the affinities of such binding interactions. Together these features of reactions can be described by determining the constants that govern the rates and substrate dependences of the system under study. Reaction events, such as the enzymatic activity of an ATPase, occur at rates based on various physical factors of the interaction. At a given set of physical parameters, a rate constant describes the relationship of how fast a reaction occurs with respect to the concentrations of reaction participants in a solution. A rate constant is represented as: k_x, where "x" indicates the type of reaction being described. For example, k_{+1}, represents an association reaction where the arbitrary molecules "A" and "B" bind to one another, as can be described by the expression: $A + B \rightarrow AB$. The rate of this reaction relates to the constant, k_{+1}, in a manner dependent upon the concentrations of reactants by the expression: rate $= k_{+1}[A][B]$. Because a reaction rate is expressed in terms of concentration per units of time,

such as M/s, the association rate constant reflects this with units per concentration, per unit time, such as $M^{-1}s^{-1}$. Similarly, k_{-1}, is a dissociation constant, where for example: $AB \rightarrow A + B$, giving: rate = $k_{-1}[AB]$. The units of k_{-1} are therefore s^{-1}. In experimental measurements, another rate constant is used. The observed rate of a given reaction at a given set of conditions is referred to as $k_{observed}$ or k_{obs}, and has units of (s^{-1}) [166].

At a given set of physical conditions, binding equilibria are also described by constants known as equilibrium constants and are represented as K_x, where again "x" indicates the type of reaction being described. The constant, K_D, represents a dissociation constant, which describes the equilibrium of the reaction $A + B \rightarrow AB$. Its relationship to this equilibrium can be defined using the rates of forward and reverse reactions as described above: $K_D = k_{-1}/k_{+1}$ and therefore has units of $s^{-1}/(M^{-1}s^{-1}) = M$. A "Binding" or "association" equilibrium constant is represented as K_A and is the inverse of the dissociation constant for the associated reaction, such that: $K_A = k_{+1}/k_{-1}$. Equilibrium constants can be described in terms of the product and reactant concentrations reached at equilibrium, as: $K_D = \frac{[A][B]}{[AB]}$ and $K_A = \frac{[AB]}{[A][B]}$ [166]. Using these kinetic principles, the rates and substrate dependences of the reactions of the MyHC ATPase cycle can be quantitatively described and compared.

Pre-steady-state studies of MyHC

Studying pre-steady-state kinetics of the myosin ATPase cycle allows for close examination of the reaction steps that ultimately lead to sarcomeric contraction. MyHC isoforms often work in synergistic mixtures in muscle fibers, such as α-MyHC and β-MyHC in cardiac muscle fibers[167] and IIa, IIb, IId and extraocular in various mixtures in fast skeletal muscle fibers[62-64]. Since it has been shown that alterations in the balance of these isoforms in a fiber affect contractility[168-172], it is of interest to understand their separate activities in an attempt to

learn how these might combine to produce muscle function.

Pre-steady-state assay techniques using stopped-flow and quench-flow systems have been used to observe the reactions that comprise the myosin ATPase cycle. These techniques have proven capable of characterizing differences among groups of MyHC isoforms[132, 133]. These studies have been limited to observations of muscle-derived S1 proteins, and so have been limited by the available muscle sources with respect to MyHC isoforms and species. Using the recombinant MyHC expression system described above, it has been possible to overcome these limitations. To perform pre-steady-state studies on these recombinant human MyHC proteins, a collaboration was established with the Geeves lab at the University of Kent in Canterbury, UK. In previous studies, the Geeves lab fully characterized the pre-steady-state kinetics of S1 from slow type I fibers, using the type I fiber-rich bovine masseter muscle, and of S1 from fast type II fiber-rich rabbit skeletal muscle[132, 133]. These established pre-steady-state methods were used in the studies described in this thesis and the Geeves lab's kinetic data derived from fast and slow S1 proteins purified from animal muscles gave us a comparison base.

The reactions of the F-actin-activated myosin ATPase cycle

The F-actin-activated myosin ATPase cycle can be simplified to five steps, depicted graphically in Figure 13. Starting arbitrarily from the rigor state, where myosin is strongly bound to F-actin in the absence of nucleotide: in Step 1A, the actin-myosin complex binds ATP, which causes a conformational change, Step 2A, drastically lowering the affinity of the actin-myosin interaction and leading to rapid dissociation of the actin-myosin complex. In Step 3, myosin hydrolyzes the bound ATP to ADP and P_i. Associated with ATP hydrolysis, a conformational change increases affinity for F-actin. In Step 4A the strongly bound actin-myosin complex is reformed, then releases P_i and undergoes its characteristic contractile

conformational change: the power-stroke. At this stage, myosin's nucleotide binding pocket is still occupied by ADP, blocking ATP-binding to induce crossbridge detachment, and so it must release ADP in step 5A before the cycle can begin again[2, 76, 78, 132, 133]. Similar conformational changes occur upon cyclical nucleotide binding interactions in the absence of actin, but with often vastly differing kinetics, in what was described above as the basal ATPase cycle. The steps of the basal ATPase cycle are shown graphically in the inner ring of Figure 13.

Notably absent from this reaction model are rates for actin-myosin dissociation and re-association before and after Step 3. Dissociation of the actin-myosin crossbridge following Step 2A has been shown to occur immediately and at a rate inseparable from that of Step 2A, as parallel measurements of Step 2A reaction progress by fluorescence and of complex dissociation by light scattering both follow the same rate, as demonstrated previously ([135, 173, 174]) and represented in Figure 14. Further, these observed dissociation events have been shown to be temperature dependent. The protein conformational change in Step 2A has been therefore defined as the rate-limiting step of dissociation followed by the rapid separation of the complex, which itself does not influence the kinetics of the cycle. The crossbridge formation step following Step 3 in the physiological sarcomeric environment is thought to be governed by the geometry of the sarcomere, which cannot be modeled in our experimental system. Crossbridge formation is therefore not measured in this study.

While analyzing these steps represents a more detailed analysis than steady-state ATPase measurements, in each case these steps encompass multiple reactions as well. Nucleotide binding, for instance, is a multi-step process, including a rapid equilibrium step and associated slower conformational change[175, 176]. For the purposes of this kinetic analysis the reactions are simplified to the steps shown in Figure 13, and rate and equilibrium constants assigned to the

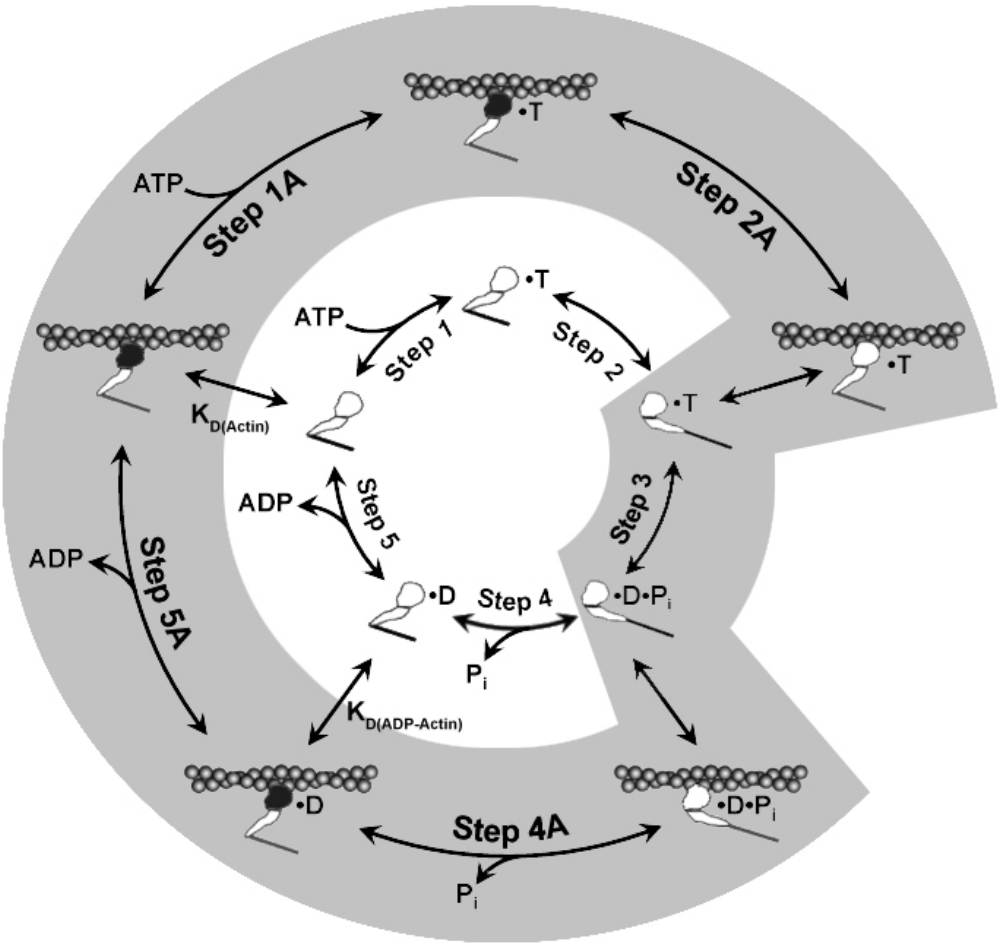

Figure 13: Reaction scheme for the actin-myosin ATPase cycle. The interaction of myosin with F-actin and nucleotides is represented here in a simplified ATPase cycle. ATP, ADP, and inorganic phosphate are represented by T, D and P_i respectively. Strong actin-MyHC binding is represented by black motor domains and detached or weakly-bound states by white motor domains. Steps occurring while bound to F-actin are indicated as Step 1A-5A, and steps in the absence of actin as Steps 1-5. The highlighted path is the physiological, active contractile cycle. Steps 1 and 1A are dependent upon the equilibrium constants of ATP binding (K_1 and K_{1A}, respectively). Steps 2 and 2A are dependent upon the rate constants of a conformational change in the motor domain associated with loss of F-actin affinity (k_{+2} and k_{+2A}, respectively). Step 3 is dependent upon the rate constant of ATP hydrolysis (k_{+3}+k_{-3}). Steps 4 and 4A are dependent upon the rate constants of P_i release (not measured here). Step 5 and 5A are dependent upon the rate constants of ADP release (k_{+5} and k_{+5A}, respectively). Dissociation of myosin from F-actin in the absence of nucleotide is governed by the dissociation constant $K_{D(Actin)}$. Dissociation of myosin from F-actin in the presence of ADP is governed by the dissociation constant $K_{D(ADP-Actin)}$. Dissociation of myosin from F-actin after Step 2A is essentially diffusion limited. Published in similar form in Deacon, et al. (2012)[2].

reaction steps as depicted in schemes accompanying each measurement henceforth. To distinguish reactions occurring in the presence of actin from parallel reactions in the absence of actin, steps in the presence of actin are referred to as Steps 1A - 5A, and in the absence of actin as Steps 1 - 5. Rate and equilibrium constants are associated with these steps using subscript descriptors of the same nomenclature, 1A - 5A or 1 - 5, respectively. It is important to note that the subscript "A's" in these descriptors indicate the presence of actin and do not denote "association" constants, as in the nomenclature, K_A.

In this chapter the steps of the ATPase cycle for the fast skeletal muscle MyHC isoforms IIa, IId, IIb and extraocular are examined at pre-steady-state. Experimental measurements were designed to determine properties of the actin-myosin ATPase cycle that would best contribute to understanding physiologically relevant characteristics of the MyHC isoforms in this study.

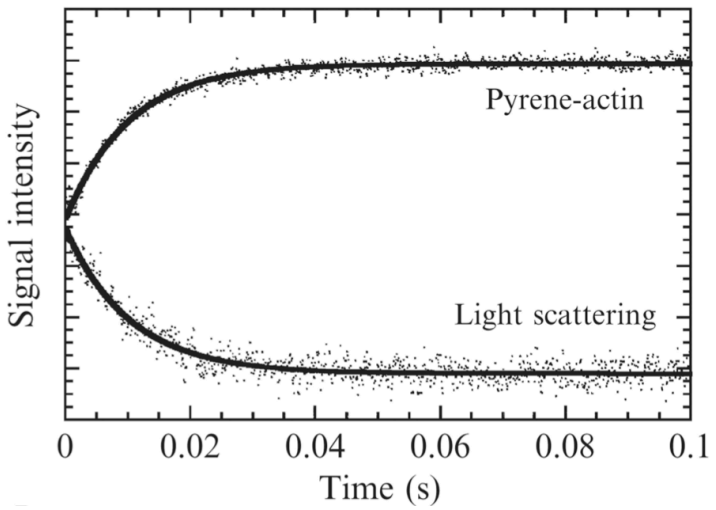

Figure 14: Rapid actin-myosin dissociation follows Step 2A. Dissociation of the actin-myosin complex is modeled to proceed rapidly following Step 2A of the actin-myosin ATPase cycle. By observing the dissociation reaction in parallel by a fluorescence signal known to change following Step 2A (Pyrene-actin) and a signal known to change upon reduction in particle size (Light scattering), dissociation clearly occurs at a rate governed by Step 2A. It is therefore assumed that separation of actin and myosin following Step 2A is essentially diffusion limited. Adapted from De La Cruz and Ostap (2009)[135].

METHODS

Stopped-flow measurements

Because of the rapid nature of certain of these reactions at the necessary temperature and reagent concentrations, these measurements require specialized experimental systems. Stopped-flow systems are designed to rapidly mix two or more solutions by pneumatically driving two syringes coupled to a single piston, pushing the solutions together through a mixing chamber and through an optical flowcell. In the flowcell, reaction mixtures can be observed as the reaction progresses by multiple optical techniques. The movement of the solutions is stopped by the backpressure of a stop syringe downstream of the flowcell. This maintains the position of the reaction aliquot in the flowcell for observation as the reaction progresses and gives the system its name, "stopped-flow." Optical readouts commonly measured with such systems include absorbance/transmittance, light scattering, circular dichroism, and fluorescence.

Stopped-flow measurements were performed using a HiTech Scientific SF-61DX2 stopped-flow system. To observe reactions at pre-steady-state, all assays were performed in high-salt buffer: 20 mM MOPS pH 7.0, containing 100 mM KCl, 5 mM $MgCl_2$, and 1 mM DTT. All reactions were performed at 20° C unless otherwise noted. Measurements were made using fluorescent signals of reaction progress. Data handling and non-linear regression analysis were performed using the stopped-flow's included software package, Kinetic Studio. Since the MyHC isoforms described in this chapter were constructed as S1-eGFP fusion proteins, there was a need to remove the fluorescence of eGFP from the data signal. This was achieved using a Kodak 47B filter, which was ~50 to 60% transparent to reaction signal wavelengths and opaque to eGFP emission fluorescence.

Fluorescence approaches to observing myosin kinetics

In order to measure actin-myosin ATPase cycle reactions in the presence of F-actin, a fluorescent marker of actin-myosin dissociation was used. F-actin can be covalently labeled with N-(1-pyrenyl)iodoacetamide (pyrene-actin) at cysteine-374 by previously established methods[132, 173]. Briefly, F-actin was dialyzed overnight into 10 mM MOPS, pH 7.6, buffer containing 100 μM $CaCl_2$, 100 mM KCl, 1 mM $MgCl_2$, 500 μM Na_2ATP, and 1 mM NaN_3, then diluted to 50 μM in the dialysis buffer in the presence of 200 μM N-(1-pyrenyl)iodoacetamide. The F-actin was rocked overnight in a light-shielded container at room temperature, then pelleted by ultracentrifugation at 200,000 x g for 90 minutes at 4° C. The pellet was resuspended in 2 mM MOPS, pH 7.6, containing 100 μM $CaCl_2$, 200 μM Na_2ATP, 1 mM NaN_3 and 1 mM DTT using a Dounce homogenizer, then depolymerized back to G-actin and subsequently repolymerized to F-actin as described previously by Pardee and Spudich[146]. Depolymerization-repolymerization cycles were used to remove damaged or dysfunctional proteins resulting from the labeling reaction, as damaged actin is expected to be unable to repolymerize. This approach has been shown to improve the quality and purity of actin samples[146, 173].

Fluorescence from pyrene-actin was excited at 365 nm and the emission, with a maximum at ~407 nm, observed through a KV389 long-pass filter. In the strongly bound complex, pyrene-actin-S1, pyrene fluorescence is ~70% quenched, likely due to allosteric effects in actin as a result of S1 binding[173, 177]. Upon dissociation of the complex immediately following Step 2A, fluorescence is unquenched, allowing pyrene-actin-S1 dissociation to be observed as an increase in fluorescence signal intensity[2, 76, 78, 132, 133, 135, 138, 173, 174, 178-182].

In the absence of actin, the intrinsic protein fluorescence of MyHC-S1 proteins was measured by excitation at 280 nm and emission observed through a WG320 long-pass filter.

Intrinsic protein fluorescence intensity is known to be modulated in MyHC-S1 proteins in response to nucleotide binding and ATP hydrolysis. These fluorescence changes are thought to be due to the shielding/deshielding of tryptophan residues resulting from conformational changes in the motor domain. Two tryptophan residues may signal nucleotide binding events at amino acid positions 112 and 130, as these residues lie within the nucleotide binding pocket[76, 183, 184]. The tryptophan residue thought to signal ATP hydrolysis is at amino acid position 508, as this residue lies near the converter and is modeled to transition from an exposed to a shielded environment as a result of a hydrolysis-coupled conformational change in the motor domain[76, 126, 185] (amino acid positions are reported with respect to the human β-MyHC sequence).

For stopped-flow reactions, concentrations are traditionally reported at their post-mixing concentrations, under the conditions in which the reactions occur. In this thesis, concentrations reported for stopped-flow assays use this convention unless otherwise specified.

Measuring crossbridge detachment

Actin-associated reactions can be examined on the stopped-flow by observing pyrene-actin fluorescence. As described above, pyrene-actin fluorescence intensity is greater in free pyrene-actin than in the pyrene-actin-S1 complex. Therefore, an increase in fluorescence intensity as a result of pyrene-actin dissociation from S1 can be observed following Step 2A of the ATPase cycle (Figure 14). This dissociation reaction can be induced by the addition of ATP to the pyrene-actin-S1 complex. On the stopped-flow, measurements of ATP-induced actin-S1 dissociation were performed by loading syringe 1 with equimolar pyrene-actin and MyHC-S1 to form the complex, and loading syringe 2 with ATP. The contents of the two syringes were then rapidly mixed and the signal change observed as the reaction progressed in the flowcell. This

reaction is designed to include Steps 1A and 2A, and therefore is dependent upon the affinity of pyrene-actin-S1 for ATP (K_{1A}) and the rate constant for Step 2A (k_{+2A}).

To observe actin-S1 crossbridge detachment and determine the constants K_{1A} and k_{+2A}, pyrene fluorescence experiments were conducted on the stopped-flow. Syringe 1 was loaded with pyrene-actin and MyHC-S1 to form the pyrene-actin-S1 complex, and syringe 2 was loaded with ATP. After mixing on the stopped-flow, pyrene-actin-S1 was at a final concentration of 0.25 μM. Reactions were repeated from 5 μM to as much as 2 mM ATP. These reactions were performed at 20° C, and fluorescence recorded for up to 10 seconds after mixing (until the fluorescence signal reached plateau). For these measurements pyrene was excited at 365 nm and a KV389 band-pass filter was used to isolate the pyrene emission signal at ~407 nm as well as a Kodak 47B filter to block eGFP background. Each reaction was repeated for 3 to 5 mixing events and the traces averaged to produce a single fluorescence trace. Each averaged fluorescence trace was fit by non-linear regression using the single exponential function:

Equation 2: $F = A \cdot (1 - e^{(-k_{obs} \cdot t)}) + F_{\infty}$

to determine the rate of the observed reaction. k_{obs} values were plotted with respect to ATP concentration and fit using the hyperbolic function:

Equation 3A: $k_{obs} = \frac{k_{max}[ATP]}{K_{1/2} + [ATP]}$.

Since $k_{max} = k_{+2A}$ and $K_{1/2} = 1/K_{1A}$, by replacing terms and multiplying the function by $1 = \frac{K_{1A}}{K_{1A}}$, the equation can be rewritten as:

Equation 3B: $k_{obs} = \frac{K_{1A}k_{+2A}[ATP]}{1 + K_{1A}[ATP]}$.

This set of reactions was repeated for 3 separate preparations of each protein.

Measuring ADP affinity of actin-S1

To measure the affinity of actin-S1 for ADP, ADP can be used as an inhibitor of the ATP-induced actin-S1 dissociation reaction. Since ADP also binds the nucleotide-binding site on S1, it can block ATP binding, and therefore inhibit dissociation. On the stopped-flow, measurements to determine ADP affinity can be performed by loading syringe 1 with pyrene-actin-S1, and loading syringe 2 with a fixed, low concentration of ATP and varied ADP concentrations. This reaction is designed to use ADP as a competitive inhibitor of ATP-induced actin-S1 dissociation, and therefore is dependent upon the affinity of actin-S1 for ADP (K_{5A}) as well as the rate of the uninhibited ATP-induced dissociation reaction, defined as k_0.

To investigate ADP binding to actin-S1 and determine the constant K_{5A}, pyrene flourescence experiments were conducted on the stopped-flow. Syringe 1 was loaded with pyrene-actin and MyHC-S1 to form the pyrene-actin-S1 complex and syringe 2 was loaded with ATP and ADP. After mixing on the stopped-flow, pyrene-actin-S1 was at a final concentration of 0.25 μM and ATP was at a final concentration of 50 μM. Reactions were performed with no ADP to establish k_0, then repeated with from 2.5 μM to as much as 1 mM ADP. These reactions were performed at 20° C, and fluorescence recorded for up to 10 seconds after mixing (until the fluorescence signal reached plateau). For these measurements pyrene was excited at 365 nm and a KV389 band-pass filter was used to isolate the pyrene emission signal at ~407 nm as well as a Kodak 47B filter to block eGFP background. Each reaction was repeated for 3 to 5 mixing events and the traces averaged to produce a single fluorescence trace. Each averaged fluorescence trace was fit by non-linear regression using Equation 2 rate of the observed reaction. This set of reactions was repeated for three separate preparations of each protein.

These data were fit using a model of Michaelis-Menten kinetics in the presence of a competitive inhibitor: $v_o = \frac{v_{max}[S]}{K_M(1+\frac{[I]}{K_I})+[S]}$, where "I" is the inhibitor and K_I is the dissociation constant for the inhibitor. This can be rewritten with terms for this context as:

$k_{obs} = \frac{k_{+2A}[ATP]}{\frac{1}{K_{1A}}(1+\frac{[ADP]}{K_{5A}})+[ATP]}$. This can be modified by dividing both sides of the equation by k_0, where k_0 is the rate of the reaction in the absence of inhibitor, as described above:

$k_0 = k_{obs} = \frac{k_{+2A}[ATP]}{\frac{1}{K_{1A}}+[ATP]}$, and since at low ATP concentrations, such as those used in these reactions, the [ATP] terms drop out of the equation, this yields:

Equation 5: $\frac{k_{obs}}{k_0} = k_{rel} = \frac{1}{1+([ADP]/K_{5A})}$ [135, 181, 186].

To determine the rate constant k_{+5A}, which governs ADP-dissociation from actin-S1, saturating ADP (500 μM for IIa, IIb, and IId and 1 mM for extraocular, before mixing) was pre-incubated with pyrene-actin-S1 and loaded in syringe 1, and syringe 2 was loaded with several-fold excess ATP. These reactions were performed at 20° C, and fluorescence was recorded for 2 seconds after mixing. For these measurements, pyrene was excited at 365 nm and a KV389 band-pass filter was used to isolate the pyrene emission signal at ~407 nm, as well as a Kodak 47B filter to block eGFP background. Each reaction was repeated for 3 to 5 mixing events and the traces averaged to produce a single fluorescence trace. Each averaged fluorescence trace was fit by non-linear regression using Equation 2 to determine the rate of the observed reaction. With the actin-S1 complex saturated by ADP before mixing, upon mixing with excess ATP, k_{obs}

is expected to be limited by the maximum rate of ADP-dissociation (governed by k_{+5A}) unless that rate exceeds the rate of ATP binding, in which case k_{obs} is expected to approximate k_{+2A}.

Measuring ATP binding to S1 in the absence of actin

In the absence of actin, measurements can be made using intrinsic protein fluorescence from tryptophan residues in S1. As described above, changes in tryptophan fluorescence intensity are known to signal conformational changes in S1 proteins in response to 1) binding ATP and 2) hydrolyzing ATP to ADP and P_i[76, 126, 183-185]. On the stopped-flow, measurements of ATP binding to S1 in the absence of actin were performed by loading syringe 1 with S1 and loading syringe 2 with ATP. The contents of the two syringes were then rapidly mixed and the tryptophan fluorescence signal change observed as the reaction progressed in the flowcell. After mixing, S1 was at a concentration of 0.25 μM. Reactions were repeated from 5 μM to 500 μM (IIa, IIb, IId) or 1 mM ATP (extraocular) after mixing. These reactions were performed at 20° C, and fluorescence recorded for up to 5 seconds after mixing. For these measurements, tryptophan fluorescence was excited at 295 nm and a WG320 band-pass filter was used to isolate the tryptophan emission signal at ~348 nm. Each reaction was repeated for 3 to 5 mixing events and the traces averaged to produce a single fluorescence trace. Each averaged fluorescence trace was fit by non-linear regression using Equation 2. k_{obs} values were plotted with respect to ATP concentration and the plot was fit by non-linear regression using Equation 3A.

Measuring ADP binding to S1 in the absence of actin

ADP binding to S1 directly gives a weak tryptophan signal change, and so ADP binding is instead investigated by its inhibition of ATP binding. Since ADP also binds the nucleotide-binding site on S1, it can block ATP binding, and therefore inhibit the appearance of the ATP binding tryptophan signal. On the stopped-flow, measurements of ADP binding to S1 in the

absence of actin were performed by loading syringe 1 with S1 pre-incubated with ADP and loading syringe 2 with ATP. After mixing, S1 was at a final concentration of 0.25 μM and ATP was at a final concentration of 100 μM. Reactions were performed with no ADP, then repeated with from 0.1 μM to as much as 20 μM ADP in syringe 1, before mixing. At the moment of mixing, two populations are expected be present in syringe 1: S1 and S1-ADP, in proportion to each isoform's affinity for ADP (governed by K_5) and the concentration of ADP in syringe 1. These populations are expected to react at two different rates when mixed with ATP: rapidly inducing a signal in the population of S1, but waiting for ADP-dissociation (Step 5) to occur before binding the S1-ADP population and producing a fluorescence signal. The amplitudes of these two phases of the reaction are expected to reflect the relative concentrations of the two populations in syringe 1 and can therefore be used to determine K_5.

To determine the rate constant governing ADP-dissociation, the S1 in syringe 1 can be saturated by ADP, then mixed with saturating ATP to maximize the rate of signal appearance after ADP-dissociation. Under these conditions, the rate of the observed reaction should be governed by the rate constant for ADP-release, k_{+5}, unless that constant is greater than that of the rate-limiting step of ATP binding, k_{+2}.

These reactions were performed at 20° C, and fluorescence recorded for up to 10 seconds after mixing, using a logarithmic timebase for data collection to enhance resolution of the faster phase of the reaction, while also measuring with sufficient resolution the far slower phase of the reaction. For these measurements, tryptophan fluorescence was excited at 295 nm and a WG320 band-pass filter was used to isolate the tryptophan emission signal at ~348 nm. Each reaction was repeated for 3 to 5 mixing events and the traces averaged to produce a single fluorescence trace. Each averaged fluorescence trace was fit by non-linear regression using the sum of two

exponential terms, Equation 4, to determine amplitudes for both fast and slow phases of the reaction traces. The relative amplitudes for the slow and fast phases plotted with respect to ADP concentration were respectively fit using:

Equation 6A: $$A = \frac{A_{max}[ADP]}{K_5 + [ADP]} + A_{min}$$

and

Equation 6B: $$A = \frac{A_{max}K_5}{K_5 + [ADP]} + A_{min}$$ [2, 132, 133].

RESULTS

ATP-induced dissociation of actin-S1 (Steps 1A and 2A)

In order to investigate the ATP-induced crossbridge detachment of the skeletal myosins, we wanted to determine the affinity of the actin-S1 complex for ATP in Step 1A and the rate constant, k_{+2A}, which governs the rate-limiting step of detachment, the conformational change in Step 2A (Figure 15).

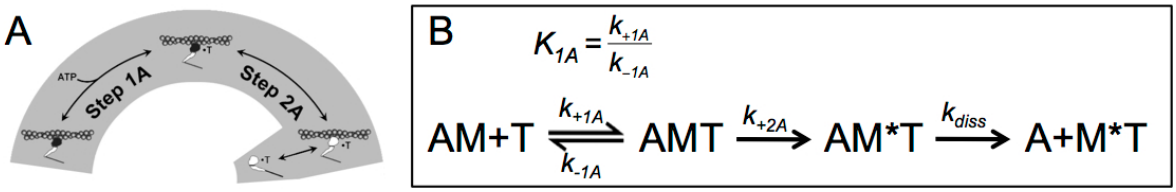

Figure 15: ATP-induced actin-S1 dissociation schemes. The participants in the reactions described are abbreviated as A = actin, M = myosin S1, and T = ATP. M* represents a different conformational state of myosin S1 with low actin affinity. ***A.*** The reaction steps following the mixing of ATP with AM are a rapid equilibrium step where ATP binds to AM (Step 1A) and a rate limiting conformational change (Step 2A) preceding a diffusion limited dissociation (k_{diss})[173, 174]. ***B.*** Step 1A is governed by the association constant, K_{1A}, and Step 2A is governed by the rate constant, k_{+2A}.

These reactions occur in the presence of actin. Actin-associated reactions can be examined on the stopped-flow by observing pyrene-actin fluorescence. As described above,

pyrene-actin fluorescence intensity is greater in free pyrene-actin than in the pyrene-actin-S1 complex. Therefore, an increase in fluorescence intensity as a result of pyrene-actin dissociation from S1 can be observed following Step 2A of the ATPase cycle (Figure 15). This dissociation reaction can be induced by the addition of ATP to the pyrene-actin-S1 complex. On the stopped-flow, measurements of ATP-induced actin-S1 dissociation were performed by loading syringe 1 with equimolar pyrene-actin and S1 to form the complex, and loading syringe 2 with ATP. The contents of the two syringes were then rapidly mixed and pyrene fluorescence observed as the reaction progressed in the flowcell. This reaction is designed to include Steps 1A and 2A, and therefore is dependent upon the affinity of pyrene-actin-S1 for ATP (K_{1A}) and the rate constant for Step 2A (k_{+2A}).

Upon mixing ATP with actin-S1 complex the dissociation reaction is modeled to progress through a two-step process: A rapid equilibrium step (Step 1A) followed by a rate-limiting conformational change (Step 2A), with hyperbolic dependence of the dissociation rate on the concentration of ATP.

The formation of the collision complex in Step 1A is assumed to be a rapid equilibrium step. This has been demonstrated for similar myosins in previous work ([2, 76, 78, 94, 132, 133, 138, 173, 174, 179-182, 186, 187]) and the assumption is supported for these myosins by adherence to our model in the hyperbolic dependence of the two-step dissociation reaction on ATP observed in this study (data shown below). The rate-limiting conformational change in Step 2A limits the maximum rate of the observed dissociation reaction and is followed by separation of the actin-S1 complex at a rate constant assumed to be essentially diffusion limited. The studies that established the utility of the pyrene fluorescence signal in observing the actin-S1 dissociation step determined that the signal arises following a temperature dependent first-order reaction step, Step 2A[173, 174,

[179, 180]. The temperature dependence of this reaction step indicated the involvement of protein movement, as is modeled for Step 2A, and the lack of any other observed events limiting the dissociation reaction indicated that dissociation following Step 2A proceeded at a rate greatly in excess of Step 2A. This was demonstrated by observing that the rate of complex separation at the end of the ATP-induced actin-S1 dissociation reaction, measured by light scattering (shown above in Figure 14), matched the rate of the pyrene fluorescence change[173, 174]. We therefore assume rapid complex dissociation following Step 2A.

ATP concentration was varied in order to observe the reaction at well below the K_D for ATP ($1/K_{1A}$), at saturating ATP concentration, and at sufficient points between the two in order to accurately model the substrate dependence of the reaction rate. Fluorescence transients resulting from these mixing events were monophasic and could be well described by non-linear regression analysis using the single exponential function, Equation 2: $F = A \cdot (1 - e^{(-k_{obs} \cdot t)}) + F_{\infty}$

Figure 16A shows a representative trace from extraocular-S1.

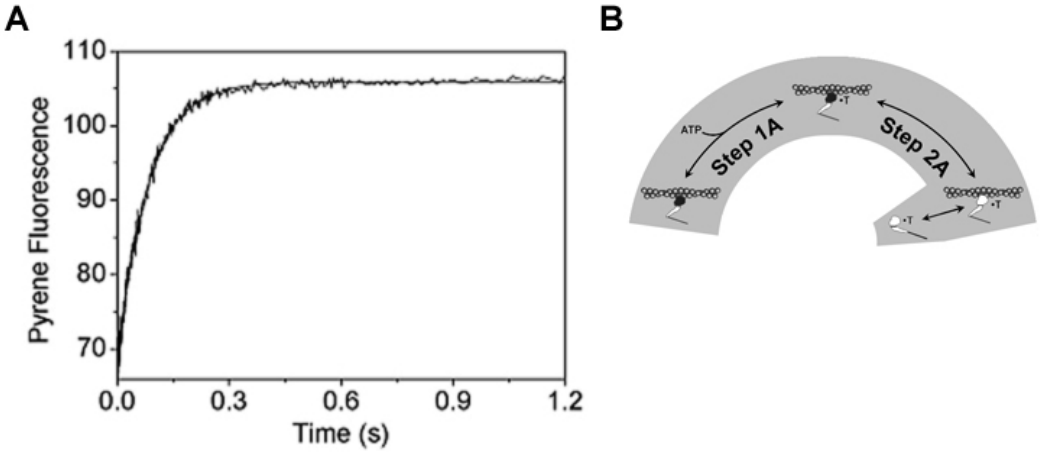

Figure 16: ATP-induced actin-S1 dissociation of extraocular-S1. ***A.*** Pyrene fluorescence change observed following mixing of pyrene-actin-extraocular-S1 with ATP, to final concentrations of 0.25 μM and 5 μM, respectively. The best-fit single exponential function is superimposed and gives a k_{obs} for this representative trace of $k_{obs} = 12.4\ s^{-1}$. ***B.*** The single phase transient observed for this reaction fits our model of a rapid equilibrium step (Step 1A) followed by a rate-limiting conformational change (Step 2A).

Because this reaction involves an initial step dependent upon a binding equilibrium (Step 1A), followed by a rate-limiting step (Step 2A), k_{max} for this reaction is defined by the rate constant for Step 2A, k_{+2A}. Therefore, at saturating ATP, $k_{obs} = k_{+2A}$. k_{obs} values obtained from these exponential functions were plotted with respect to their associated ATP concentrations to produce saturation curves. These curves were fit by non-linear regression analysis using the hyperbolic function, Equation 3B: $k_{obs} = \frac{K_{1A}k_{+2A}[ATP]}{1+K_{1A}[ATP]}$ [2, 132, 174]. For each isoform, this set of reactions was performed on three independent preparations of protein. Figure 17 shows representative curves from single preparations of each isoform.

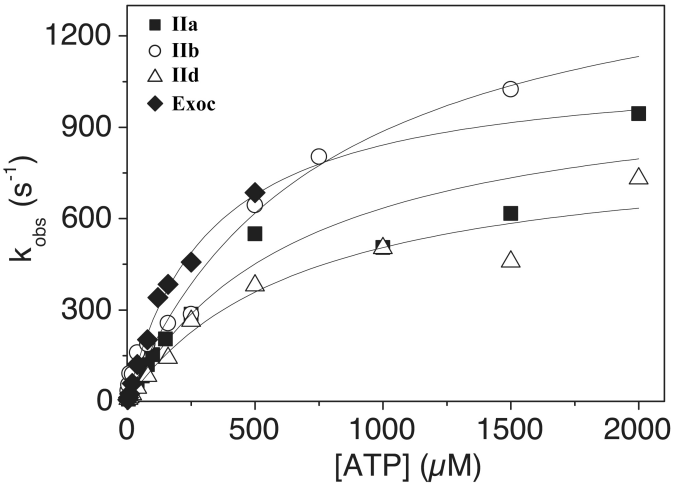

Figure 17: ATP-induced actin-S1 dissociation of fast skeletal S1. Plots of k_{obs} for the skeletal isoforms IIa (■), IIb (○), IId (△), and extraocular (◆) following binding of ATP are well-described by the hyperbolic function, Equation 3B, and best-fit curves are superimposed. Representative curves from single preparations of each isoform are shown, displaying variation in both saturation k_{max} (=k_{+2A}) and $K_{1/2}$ (=$1/K_{1A}$) values.

At high ATP concentrations the rate of the dissociation reaction becomes very fast and approaches the detection limit of the stopped-flow. Because of this, fits to reactions at low ATP concentrations have a higher confidence than at high ATP concentrations. At low ATP concentrations the plot of k_{obs} with respect to ATP concentration is linear and $k_{obs} = \frac{K_{1A}k_{+2A}[ATP]}{1+K_{1A}[ATP]}$ simplifies to:

Equation 7: $k_{obs} = K_{1A}k_{+2A}$,

with an estimated worst case error of ~20% for ATP concentrations where $K_{1A}[ATP] < 0.2$. This error falls within the range of confidence of our measurements. We therefore use linear fits to aid in the estimation of kinetic constants from ATP-induced actin-S1 dissociation reactions. The hyperbolic fits to the curves represented in Figure 17 as well as linear fits to the low ATP linear phase were used to calculate values for the kinetic constants, $K_{1A}k_{+2A}$, $1/K_{1A}$ and k_{+2A}. These measurements and calculations were repeated over three independent protein preparations for each isoform and the values averaged and reported as mean values in Table 3. From the linear fits, the apparent second-order rate constant for the ATP-induced actin-S1 dissociation reaction, $K_{1A}k_{+2A}$, differentiated the isoforms into the faster isoform: 3.2±0.4 $\mu M^{-1}s^{-1}$ for extraocular-S1, and the slower group: 1.4±0.07, 1.7±0.1, and 1.8±0.6 $\mu M^{-1}s^{-1}$, for IIb, IId and IIa respectively (Table 3). At high ATP concentrations the reaction rates were very fast and difficult to measure. At low ATP concentrations the reaction rates were slower and well defined. While for IIa and IId the reaction rates were measured at ATP concentrations greater than the reliability point of 3-times $1/K_{1A}$, this could not be achieved for extraocular or IIb. From the hyperbolic fits, the rate constant for the rate-limiting conformational change, k_{+2A}, was seen to be very fast for all four isoforms, from 814 s^{-1} for IId to >1400 s^{-1} for IIb. Given the limitations of the data at high ATP concentrations for the isoforms extraocular and IIb, and typical for ATP-induced actin-myosin dissociation measurements, $1/K_{1A}$ values were calculated using the linear phase fits with Equation 7, giving a range of tighter affinities: 360±49, 450±151, and 660±60 μM, for extraocular, IId, and IIa, respectively, and a far weaker affinity of >1000 μM for IIb (Table 3).

ADP inhibition of ATP-induced dissociation of actin-S1 (Step 5A)

In order to investigate the ADP-binding characteristics of the skeletal myosins, we wanted to determine the affinity of the actin-S1 complex for ADP and the rate of ADP-

dissociation from actin-S1 in Step 5A (Figure 18). To observe these characteristics in the presence of actin we again used pyrene-actin fluorescence to signal the ATP-induced dissociation of the actin-S1 complex, and added ADP to the reactions as a competitive inhibitor of ATP binding.

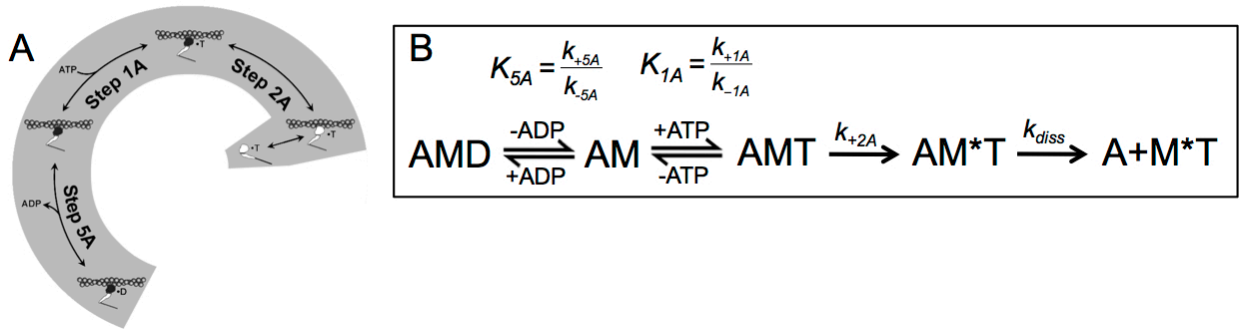

Figure 18: ADP inhibition of ATP-induced actin-S1 dissociation schemes. The participants in the reactions described are abbreviated as A = actin, M = myosin S1, D = ADP, and T = ATP. M* represents a different conformational state of myosin S1 with low actin affinity. ***A.*** The reaction steps following the mixing of ATP and ADP with AM include two possible paths, where AM mixed with ATP and ADP may progress through ATP-induced AM dissociation as described above, or may first bind ADP in the reverse reaction of Step 5A. ***B.*** Step 5A is governed by the dissociation constant K_{5A}, Step 1A is governed by the association constant K_{1A} and Step 2A is governed by the rate constant k_{+2A}.

ADP was added to the syringe containing ATP to act as a competitive inhibitor for binding actin-S1. With ATP at a fixed low concentration, well below the K_D of actin-S1 for ATP, ADP concentration was varied in sequential reaction mixtures in order to observe the reaction at well below the K_D of actin-S1 for ADP (K_{5A}), at saturating ADP concentration, and at sufficient points between the two in order to accurately model the inhibition. Fluorescence transients resulting from these mixing events were monophasic and could be well described by non-linear regression analysis using the single exponential function, Equation 2:

$F = A \cdot (1 - e^{(-k_{obs} \cdot t)}) + F_{\infty}$. k_{obs} values from these fits were converted to k_{rel} values by dividing by k_0, and k_{rel} was plotted with respect to ADP concentration. These plots were fit using Equation

5: $\frac{k_{obs}}{k_0} = k_{rel} = \frac{1}{1+([ADP]/K_{5A})}$. Figure 19A shows representative curves from single preparations of each isoform.

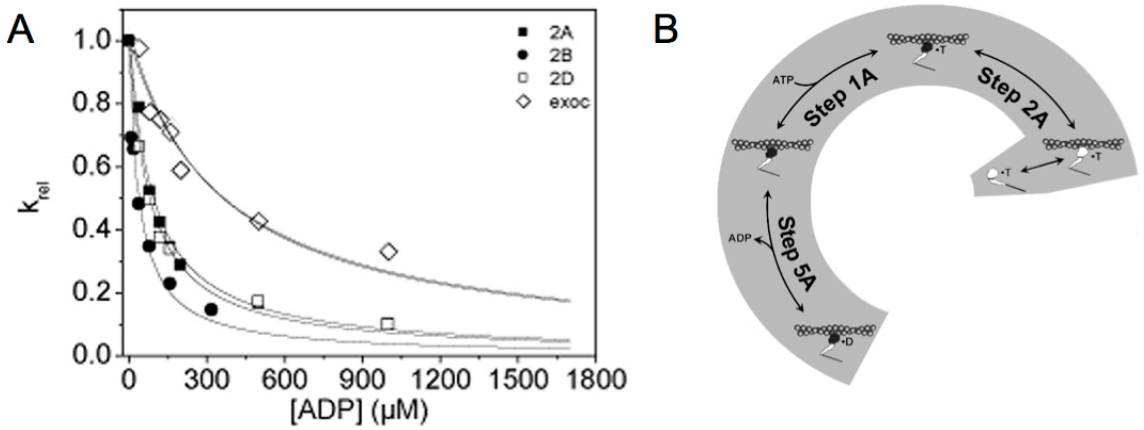

Figure 19: ADP inhibition of ATP-induced actin-S1 dissociation of fast skeletal S1. ***A.*** Plots of k_{rel} for the skeletal isoforms IIa (■), IIb (●), IId (□), and extraocular (◇) with respect to ADP concentration. ***B.*** A fit of Equation 5 to this data yields the dissociation constant of the actin-S1 complex for ADP in Step 5A, K_{5A}.

These ADP inhibition of ATP-induced actin-S1 dissociation measurements were repeated on three independent protein preparations of each isoform and the K_{5A} values averaged and reported as mean values in Table 3. K_{5A} values range from a tighter binding group of IIb, IIa and IId, with K_{5A} = 42±6, 80±15 and 109±29 μM, respectively, to the far lower affinity extraocular isoform, with K_{5A} = 350±9 μM (Table 3).

Investigations of the rate constant governing ADP dissociation from actin-S1 were performed by pre-incubating actin-S1 with saturating ADP in syringe 1 before mixing with excess ATP in syringe 2. For each of the fast skeletal isoforms it was found that the presence of ADP did not separate k_{obs} from k_{+2A}. The ADP dissociation step, therefore, must occur more rapidly than the ATP binding step and so could not be observed. For each skeletal isoform the rate constant for ADP-dissociation in Step 5A, k_{+5A}, is set to the minimum value of > k_{+2A}, since k_{+2A} limits the observable rate of ADP-dissociation from actin-S1 for these isoforms.

Actin-independent ATP binding and hydrolysis (Steps 1-3)

In order to investigate the interaction of S1 with ATP in the absence of actin we wanted to determine the affinity of S1 for ATP, governed by the association constant, K_1, the rate constant governing Step 2, k_{+2}, and the rate constant for the ATP hydrolysis step, $k_{+3} + k_{-3}$, in Step 3 (Figure 20).

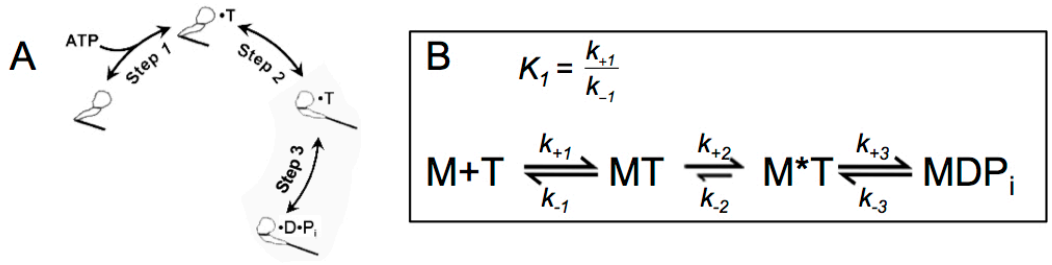

Figure 20: Actin-independent ATP binding and hydrolysis schemes. The participants in the reactions described are abbreviated as M = myosin S1, D = ADP, T = ATP, and P_i = inorganic phosphate. M* represents a different conformational state of myosin S1. ***A.*** The reaction steps following the mixing of ATP with myosin S1 are a rapid equilibrium step where ATP binds to S1 (Step 1), a conformational change (Step 2), and hydrolysis of ATP into ADP and P_i (Step 3). ***B.*** Step 1 is governed by the association constant K_1, Step 2 is governed by the rate constant k_{+2}, and in Step 3 the rate of ATP hydrolysis is defined by the sum, $k_{+3} + k_{-3}$.

These reactions occur in the absence of actin and we therefore could not use the pyrene fluorescence signal to detect reaction progress after mixing in the stopped-flow. For these reactions we observed changes in intrinsic protein fluorescence. As described above, several tryptophan residues in S1 are known exhibit changes in fluorescence signal as a result of conformational changes induced in S1 by Steps 2 and 3 of the contractile cycle. These reactions were experimentally investigated on the stopped-flow by loading syringe 1 with S1 and syringe 2 with ATP, then rapidly mixing and observing tryptophan fluorescence. This experimental design includes Steps 1, 2 and 3, and fluorescence changes are expected to result from Steps 2 and 3. Reaction mixtures were repeated with ATP concentration varied in order to observe the reaction at well below the K_D for ATP ($1/K_1$), at saturating ATP concentrations and at sufficient points

between the two in order to accurately model the substrate dependence of the reaction rate. Fluorescence transients resulting from these mixing events were monophasic and could be well described by non-linear regression analysis using the single exponential function, Equation 2: $F = A \cdot (1 - e^{(-k_{obs} \cdot t)}) + F_{\infty}$. Figure 21A shows a representative trace from IId-S1. k_{obs} values from these fits were plotted with respect to ATP concentration and the resulting curves were analyzed by fitting Equation 3A: $k_{obs} = \frac{k_{max}[ATP]}{K_{1/2} + [ATP]}$. For each isoform, this set of reactions was performed on three independent preparations of protein. Figure 21B shows a representative curve from a single preparation of IId-S1.

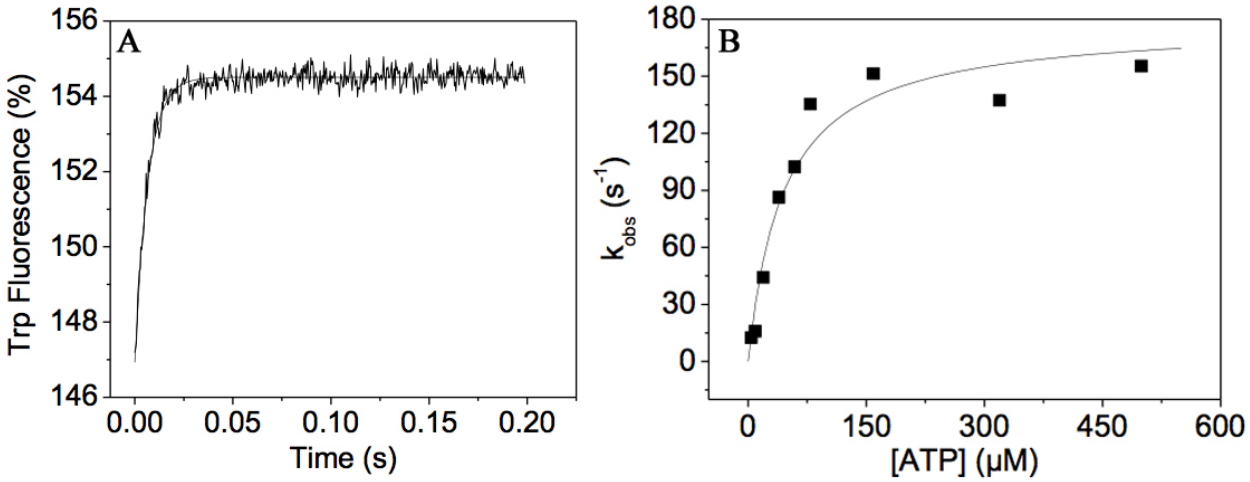

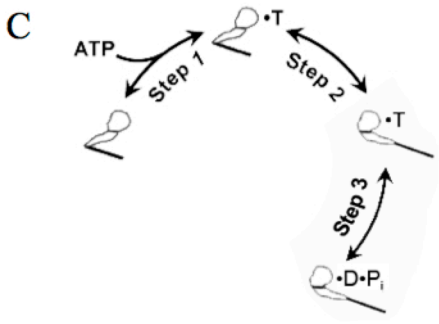

Figure 21: Actin-independent ATP binding to IId-S1. ***A.*** In the stopped-flow, 0.25 μM S1 was rapidly mixed with 160 μM ATP. The averaged fluorescence transient was fit using Equation 2, yielding, k_{obs} = 153 s^{-1}. ***B.*** Reactions were measured from 5 μM to 500 μM ATP and the resulting k_{obs} plotted with respect to ATP concentration. The resulting plot was fit using Equation 3A and saturated at k_{max} = 178 s^{-1}. ***C.*** Following ATP binding to S1 in Step 1, Steps 2 and 3 both are expected to give tryptophan signals. This monophasic reaction represents either Step 2 or Step 3.

The monophasic nature of the ATP-binding reaction traces indicated that only one of the

two possible reaction steps, Step 2 or Step 3, was observable using this reaction setup for the fast skeletal isoforms. We interpret this to mean that the other reaction of the two must occur faster than the observed reaction, though it is also possible that Step 2 was observed and a slower Step 3 exists, but gave no fluorescence signal. To clarify the assignment of these fluorescence changes to their appropriate reaction step we typically use quench-flow assays measuring the rate of ADP product formed resulting from mixing S1 with ATP and incubating for a short time before stopping the reaction (described in detail in Chapter IV, Methods). This second assay method provides an independent measure of Step 3 and aids in distinguishing between Steps 2 and 3 for this analysis. For these isoforms this process is still underway and the necessary quench-flow experiments have not yet been performed due to the limitations of recombinant protein production. We therefore can only determine that these data represent one of the two rate constants, k_{+2} or $k_{+3} + k_{-3}$.

Given these limitations, the hyperbolic fits yielded unassigned k_{max} values and fits to the linear phase using Equation 7 at low ATP concentrations where its derivation holds, yielded putative second order rate constants for the binding interaction, K_1k_{+2}, depending upon the observed rate-limiting reaction representing k_{+2}. These isoforms displayed a very similar range of values for the rate-limiting reaction (k_{+2} or $k_{+3} + k_{-3}$), from the lowest, IIa at 141±28 s^{-1}, to the highest, IId at 195±11 s^{-1}, with a group mean value of 170 s^{-1}. The putative second order rate constants, K_1k_{+2}, were found to differ more greatly, ranging from the lowest, extraocular at 1.0±0.2 $\mu M^{-1}s^{-1}$, to the highest, IId at 3.8±0.2 $\mu M^{-1}s^{-1}$, with a group mean of 2.2 $\mu M^{-1}s^{-1}$ (Table 3).

Actin-independent ADP binding (Step 5)

In order to investigate the interaction of S1 with ADP in the absence of actin we wanted to determine the affinity of S1 for ADP, governed by the dissociation constant, K_5, and the rate constant governing ADP-dissociation from S1 in Step 5, k_{+5} (Figure 22).

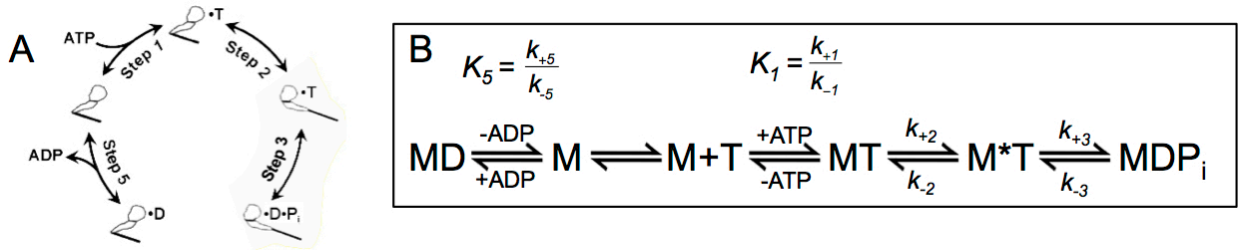

Figure 22: Actin-independent ADP binding and release schemes. The participants in the reactions described are abbreviated as M = myosin S1, D = ADP, T = ATP, and P_i = inorganic phosphate. M* represents a different conformational state of myosin S1. ***A.*** The reaction steps following the mixing of ATP with S1-ADP are a slow ADP-dissociation step (Step 5), a rapid equilibrium step where ATP binds to S1 (Step 1), a conformational change (Step 2), and hydrolysis of ATP into ADP and P_i (Step 3). ***B.*** Step 5 is governed by the dissociation constant, K_5, and the rate constant k_{+5}, Step 1 is governed by the association constant K_1, Step 2 is governed by the rate constant k_{+2}, and in Step 3 the rate of ATP hydrolysis is defined by the sum, $k_{+3} + k_{-3}$.

Tryptophan fluorescence was again used to observe reactions in the absence of actin. We observed that the tryptophan fluorescence change upon binding of S1 to ADP was very small and insufficient to accurately define the reaction, given our limitations with respect to protein production. Because the ATP-binding tryptophan fluorescence change was far greater, reactions were designed to infer parameters associated with ADP binding from reactions observing ATP-binding tryptophan signals. Because ADP and ATP share the same binding site on S1, ADP can block ATP binding and thereby inhibit the appearance of the ATP-binding tryptophan signal.

ADP binding parameters of the skeletal isoforms of S1 in the absence of actin were experimentally investigated on the stopped-flow by loading syringe 1 with pre-incubated S1 and ADP, and syringe 2 with ATP, then rapidly mixing and observing tryptophan fluorescence.

Given the monophasic nature of ATP binding to S1 for these isoforms, this experimental setup is designed to produce two phases in the ATP binding fluorescence transient, due to the two S1 populations in syringe 1. Syringe 1 contains both S1 and S1-ADP in complex before mixing with ATP from syringe 2. The ATP-binding signal occurs rapidly in the free S1 population and slower in the S1-ADP population due to the extra reaction step of ADP-dissociation. The signal amplitudes of these fast and slow phases reflect the respective concentrations of the two populations in syringe 1 before mixing. The relative concentrations of S1 and S1-ADP are governed by the dissociation constant K_5. As the ADP concentrations increase, the amplitude of the slow phase should increase and the amplitude of the fast phase should decrease, reflecting a shift in the two populations. By analyzing the amplitudes of the fast and slow phases with respect to ADP concentration, K_5 can be determined.

Reaction mixtures were repeated with pre-mixing ADP concentration varied in order to observe the reaction at well below the K_D of S1 for ADP (K_5), at saturating ADP concentrations and at sufficient points between the two in order to accurately model the substrate dependence of the amplitudes for each phase of the reaction. Fluorescence transients resulting from these mixing events were, as anticipated, biphasic. The transients could be well described by the sum of two exponential functions, Equation 4: $F = A_{fast} \cdot (1 - e^{(-k_{obs(fast)} \cdot t)}) + A_{slow} \cdot (1 - e^{(-k_{obs(slow)} \cdot t)}) + F_{\infty}$, when using ATP concentrations high enough to significantly separate the two phases of the reaction (~100-fold, Figure 23A). A representative trace from IId-S1 is shown in Figure 23A.

Amplitudes (A) for each exponential term in the function were defined as the percent fluorescence change during the reaction with respect to the fluorescence value at the end point of the reaction, and were obtained from fits to the fluorescence transients. Relative amplitudes for the slow and fast phases were plotted with respect to pre-mixing ADP concentration and fit using

Equations 6A: $A = \frac{A_{max}[ADP]}{K_5 + [ADP]} + A_{min}$ and 6B: $A = \frac{A_{max}K_5}{K_5 + [ADP]} + A_{min}$, respectively (Figure 23B). From these fits to the data, we yielded two K_5 values for each isoform, for each preparation of protein, which were averaged and are reported as a single K_5 value in Table 3. K_5 values for the fast skeletal isoforms ranged from a tighter binding group, 0.7±0.2, 1.0±0.3, and 1.4±0.1 μM, for extraocular, IIa and IIb, repectively, to the weaker binding, IId at K_5 = 3.0±0.5 μM. At saturating ADP (100 μM) and excess ATP (2 mM), k_{obs} should be defined by k_{+5}, assuming Step 5 occurs slower than and limits the rate of ATP binding. For these isoforms, k_{+5} was indeed slower. Measurements at these conditions yielded rate constants governing ADP-dissociation, k_{+5}, of between 0.7±0.1 s^{-1} for extraocular, and 2.0 s^{-1} for IIb (Table 3), with a group mean of 1.28 s^{-1}.

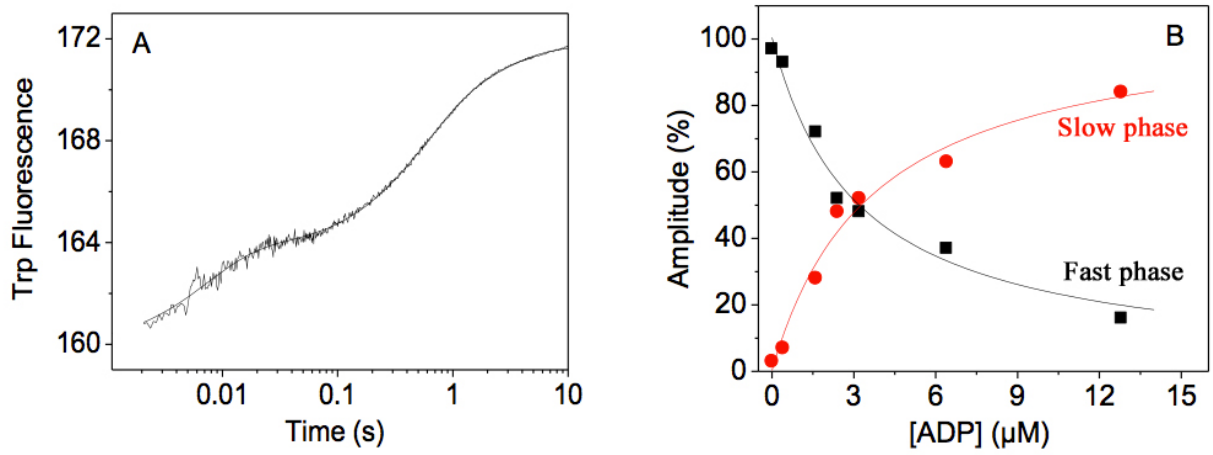

Figure 23: ADP binding to IId-S1. ***A.*** On the stopped-flow 0.25 μM, post-mixing, IId-S1, pre-incubated with ADP at 3.2 μM, before mixing, was rapidly mixed ATP at 100 μM, post-mixing. The fluorescence transient was best fit by the sum of two exponential terms, Equation 4, yielding a fast phase of k_{obs} = 144 s^{-1} with an amplitude of 2.4%, and a slow phase of k_{obs} = 1.6 s^{-1} with an amplitude of 4%. ***B.*** The dependence of the amplitudes of the two phases of the reaction were fit using Equations 6A and 6B. These functions gave K_5 values of 3.2 μM and 3.7 μM for the fast phase and slow phase, respectively.

	Extra-ocular	IIa	IId	IIb	Rabbit fast S1*	Bovine slow S1[#]
ATP binding to actin-S1						
$K_{1A}k_{+2A}$ ($\mu M^{-1}s^{-1}$)	3.2±0.4	1.7±0.1	1.8±0.6	1.4±0.07	2.4	1.24
$1/K_{1A}$ (μM)	360±49	660±60	450±151	>1000	520	984
k_{+2A} (s^{-1})	1152±60	1125±78	814±40	>1400	1250	1220
ADP binding to actin-S1						
K_{5A} (μM)	350±9	80±15	109±29	42±6	120	9.6
ATP binding to S1						
K_1k_{+2} ($\mu M^{-1}s^{-1}$) †	1.0±0.2	2.5 ±0.5	3.8±0.2	1.6±0.3	1.9	0.97
k_{+2} OR $k_{+3} + k_{-3}$ (s^{-1}) †	177±8	141±28	195±11	167±16	>200	117
ADP binding to S1						
K_5 (μM)	0.7±0.2	1.0±0.3	3.0±0.5	1.4±0.1	2.0	2.0
k_{+5} (s^{-1})	0.7±0.1	0.9±0.1	1.5±0.2	2.0±0.1	1.4	1.0

Table 3: Stopped-flow kinetics of the fast skeletal myosins. Recombinant S1 proteins bearing carboxy terminal eGFP-tags were observed interacting with ATP, ADP, and pyrene-actin. The mean values for calculated rate and equilibrium constants are given and variance reported as standard error of the mean. These data represent three biological replicates each. (†) These data require confirmation by quench-flow before they can be accurately attributed to their respective reactions. (*) Rabbit fast skeletal muscle S1 and ([#]) Bovine slow masseter muscle S1 are included for reference to previous measurements of fast and slow skeletal isoforms, including data from: [132, 180, 184]. For each constant, these isoforms generally reflect the activity of the rabbit fast S1, with the possible exception of IIb, which trends more with bovine slow S1.

Interference from the eGFP-tag

The presence of the eGFP-tag on the fast skeletal myosin constructs necessitated the use of the Kodak 47B filter for measurements using pyrene fluorescence. This removed nearly half of the total fluorescence signal from many reactions and therefore required higher quantities of protein to measure myosin activities. We therefore eliminated this tag from future myosin constructs and, as will be described in Chapter IV, this greatly improved signal to noise in stopped-flow measurements. Comparison of the kinetics of constructs with and without the eGFP-tag were generally similar, but possible differences were found (see Chapter IV, Results).

DISCUSSION

Extraocular has very fast crossbridge detachment kinetics

The apparent second order rate constant for crossbridge detachment, $K_{1A}k_{+2A}$, can be used as a convenient metric for comparing overall detachment rates from the nucleotide-free actin-S1 state[2, 132, 133, 138, 181]. In this set of human fast skeletal MyHC isoforms the traditional skeletal muscle trio, IIa, IId, and IIb group together closely by this metric at between 1.4±0.07 and 1.8±0.6 $\mu M^{-1}s^{-1}$. The specialized fast skeletal isoform, extraocular, is modestly faster than the traditional IIa, IId, and IIb group by this metric at 3.2±0.4 $\mu M^{-1}s^{-1}$. This is largely due to extraocular's actin-S1 to ATP binding being the tightest of the group, $1/K_{1A}$ = 360±49 μM, versus 660±60, and >1000 μM for IIa and IIb, although IId may be similarly tight at 450±151 μM.

ADP dissociation rate from actin-S1, governed by k_{+5A}, is known to limit crossbridge detachment in slow but not fast MyHC isoforms, in which the rate of ADP-dissociation in Step 5A, exceeds that of the ATP-binding rate-limiting step, Step 2A[2, 132, 133, 181]. The ADP affinity of actin-S1 (K_{5A}) trends with ADP-dissociation rate, such that slow isoforms with detachment rate-limiting ADP-dissociation steps tend to have tighter ADP affinities than fast isoforms with fast ADP-dissociation[2, 132, 181]. Among this group of human fast skeletal muscle isoforms, extraocular-MyHC binds ADP ~3- to 9-fold weaker (K_{5A} = 350±9 μM) than IIa, IId, or IIb (K_{5A} = 80±15, 109±29, and 42±6 μM, respectively). While this feature does not necessarily reflect a difference with physiological relevance to the contractile cycle, it trends towards "faster" detachment kinetics. These features combine to describe extraocular-MyHC as a very fast isoform. Further study of its ATP hydrolysis step will be of interest to determine its duty ratio and overall cycle time to complete the picture of its contractile character.

Human MyHC-IIb has the kinetic attributes of slower myosins

Fast skeletal muscle myosins are characterized as binding ATP tightly and rapidly dissociating the actin-myosin crossbridge. These characteristics can be seen in rabbit fast skeletal muscle S1, which has a high $K_{1A}k_{+2A}$ value and low value for the ATP dissociation constant, $1/K_{1A}$ relative to bovine slow skeletal muscle S1 (Table 3). MyHC-IIb in rodents is associated with the fastest fiber types, and is therefore thought to be very fast by these kinetic descriptors. However, the human isoform is not expressed as protein in healthy human muscles[61]. These measurements indicate that, unlike a fast skeletal myosin, human IIb-S1 binds ATP very weakly, $1/K_{1A}$ >1000 μM. The human MyHC-IIb S1 resembles the bovine slow masseter muscle S1 in actin-associated reaction kinetics more than either rabbit fast skeletal S1 or the human fast skeletal isoforms, IIa and IId. Human MyHC-IIb S1 has the slow-isoform traits of slow apparent second order kinetics of ATP-induced actin-S1 dissociation ($K_{1A}k_{+2A}$), weak ATP binding (K_{1A}), and trends towards tighter ADP binding (K_{5A}). It is conceivable that in humans the absence of MyHC-IIb expression in healthy muscles has effectively protected the gene from selection to resist genetic drift. Its ability to act as a functional motor and drift towards the highly selected for (in its own contractile environment) role of a slow myosin is surprising and potentially contradictory to this hypothesis. Further study of human MyHC-IIb function would be of interest to investigate these questions.

ADP-dissociation is fast in the presence of actin and slow in its absence

In the F-actin-activated reaction designed to investigate Step 5A, ADP-dissociation occurred fast enough to be undetectable, as it did not influence the maximum rate of ATP-induced actin-S1 dissociation at saturating ADP concentrations. This indicates that the ADP-dissociation step does not limit the rate of crossbridge detachment for these fast skeletal MyHC

isoforms, and thus does not determine fiber-shortening velocity in the fibers containing these isoforms.

In contrast to the very rapid rate of ADP-dissociation in the presence of actin, the fast skeletal isoforms release ADP very slowly in the absence of actin. The minimum values for the actin-dependent ADP-dissociation rate constant, k_{+5A}, limited by k_{+2A}, are estimated to be on the order of ~1000 s^{-1} for these isoforms, whereas, in the absence of actin, the rate constant, k_{+5}, ranged from 0.7 to 2.0 s^{-1}. This indicates that ADP-dissociation occurs on the order of 1000-fold slower when actin is not present. Likewise, the basal ATPase activities of these isoforms were on the order of 1000-fold slower than their F-actin-activated ATPase activities, as described in Chapter I. Therefore, the ADP-dissociation step, Step 5, may be responsible for limiting the rate of ATP consumption in the absence of F-actin by acting as the rate-limiting step of the basal ATPase cycle.

CHAPTER III

Human embryonic-MyHC and Freeman-Sheldon Syndrome

INTRODUCTION

Embryonic-MyHC

The Embryonic-MyHC isoform is expressed early in fetal development and is absent in the adult, except during muscle regeneration. Given the vastly different environment of muscles *in utero* versus in adult life, the embryonic-MyHC isoform may function differently from the adult skeletal isoforms. For example, the developmental contractile environment does not likely involve significant voluntary contractile activity, nor any high-tension contraction, but may instead play a role in guiding the development of muscle structures. Embryonic-MyHC has also been detected in muscles regenerating after injury. Previous studies of developmental myosins have indicated that the developmental myosin isoforms may be far slower than adult isoforms, as chicken embryo myosins have slower *in vitro* motility than adult chicken myosin[155], and myosin from fast-twitch muscle fibers in neonatal rats has increasing ATPase activity with age[154]. However, ATPase measurements of pure recombinant isoforms in Chapter I indicate that embryonic-MyHC is within ~2-fold of the rate all of the fast skeletal isoforms by ATPase k_{cat}. Further, the presence of disease-causing mutations in functional sites in the embryonic-MyHC motor domain indicates that its physiological role likely requires functional contractile activity. The activity of embryonic-MyHC in developmental and regenerating muscles therefore warrants closer examination.

Freeman-Sheldon Syndrome

Freeman-Sheldon Syndrome (FSS) is among the most severe of the congenital disorders

classified as distal arthrogryposes. Distal arthrogryposes include congenital conditions of isolated and multiple joint contractures, the most common of which is clubfoot. These disorders have a prevalence of between 1 in 500 births in the case of clubfoot, and 1 in 3000 births with multiple joint contractures[188]. While there are varied biological origins leading to the various distal arthrogryposes[189], FSS is known to be caused thus far, solely by dominant mutations in the motor domain of embryonic-MyHC[188, 190]. FSS is characterized by multiple distal joint contractures as well as facial muscle contractures. As the mutations causing this syndrome are in an isoform of myosin restricted to fetal development, it is non-progressive after birth but can still lead to significant and persistant abnormalities[190]. One of the most frequent sites of mutation is in arginine-672, which has been found mutated to histidine or cysteine[88, 190] in many FSS patients.

Arginine-672 is a highly conserved residue, which lies in the nucleotide-binding pocket of the MyHC motor domain (Figure 24). It is positioned in the central β-sheet with its sidechain facing a neighboring strand containing the residue threonine-178 (Figure 24, inset). Threonine-178 is immediately adjacent to the phosphate-binding loop of the active site. The polar guanidino and hydroxyl groups of these two residues are modeled to be within 2.9 - 3.2 Å of one another by crystallographic studies of human β-MyHC motor domain and scallop myosin S1, respectively (PDB IDs: 4DB1 and 1QV1, respectively), indicating that these residues may hydrogen bond to one another. The mutation of residue threonine-178 in embryonic-MyHC to isoleucine has been found to cause a similar distal arthrogryposis disorder, known as Sheldon-Hall Syndrome[88, 191]. The coincidence of these two mutations in this site indicates its high importance in the proper contractile function of embryonic-MyHC. The high degree of similarity between the disorders may indicate that this site controls very specific aspects of embryonic-MyHC's function. For this reason and to understand its impact in human disease, the

functional effects of the FSS-causing mutation R672H in embryonic-MyHC are examined in this chapter.

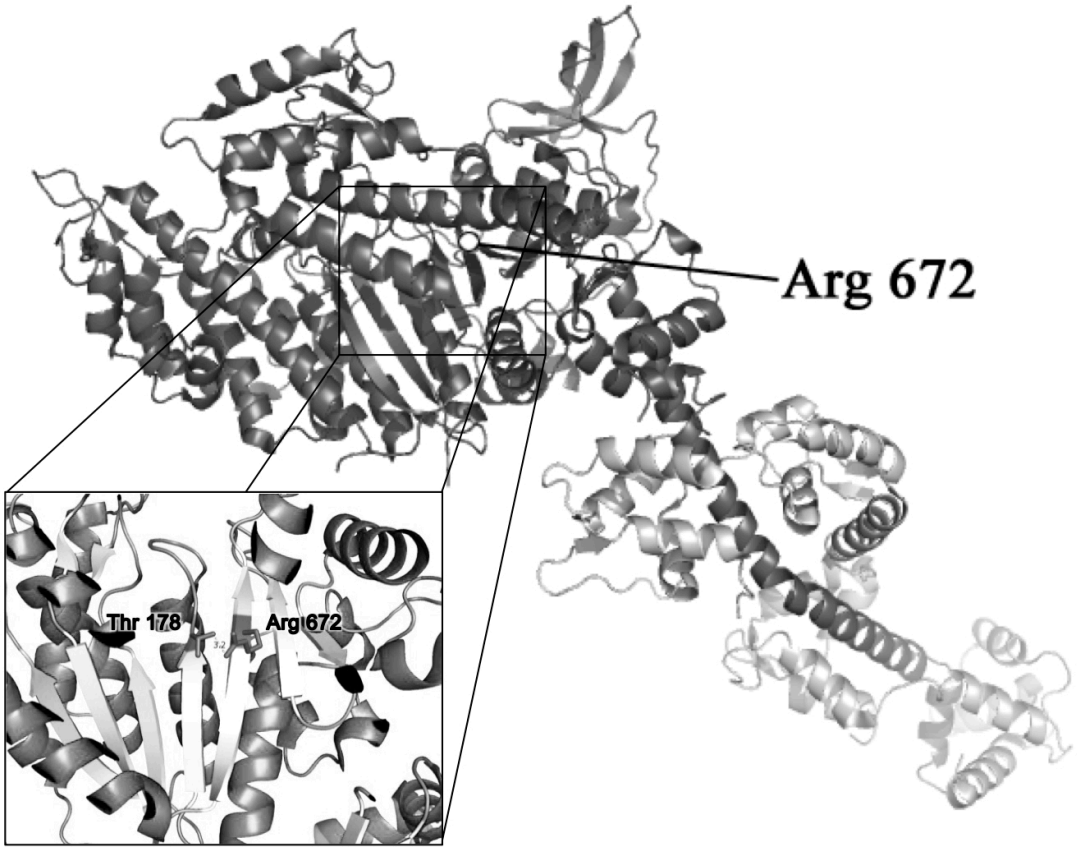

Figure 24: Freeman-Sheldon Syndrome mutation R672H. The arginine-672 residue of embryonic-MyHC, is located in the nucleotide-binding pocket in the central beta-sheet in the motor domain. When this site is mutated to a histidine residue it causes Freeman-Sheldon Syndrome. On the adjacent beta-strand, the nearby residue threonine-178 is also found to be mutated in embryonic-MyHC, causing a distal arthrogryposis disorder, Sheldon-Hall Syndrome. Shown within crystal structure PDB ID: 1QV1.

METHODS

Production of recombinant embryonic-MyHC subfragments

Human embryonic-MyHC was cloned from human embryonic cDNA. The region encoding S1, including methionine-1 through alanine-844, was subcloned into pShuttle, in frame with a 6x histidine-tag at the carboxy terminus prior to the translation stop codon (Figure 25).

This cloning vector was used to produce recombinant adenovirus using methods described in Chapter I. The point mutation R672H was inserted into the coding region of embryonic-S1 in the pShuttle vector using PCR primers containing single nucleotide mismatches overlapping the mutation target sequence to introduce the point mutation into PCR products. Using these PCR products, the S1 cloning region was reproduced by recombinant PCR and reinserted into pShuttle in frame with the 6x histidine-tag. These pShuttle plasmids were used to produce recombinant adenoviruses encoding human embryonic-S1 (Emb-WT) and human embryonic-R672H-S1 (Emb-R672H) proteins.

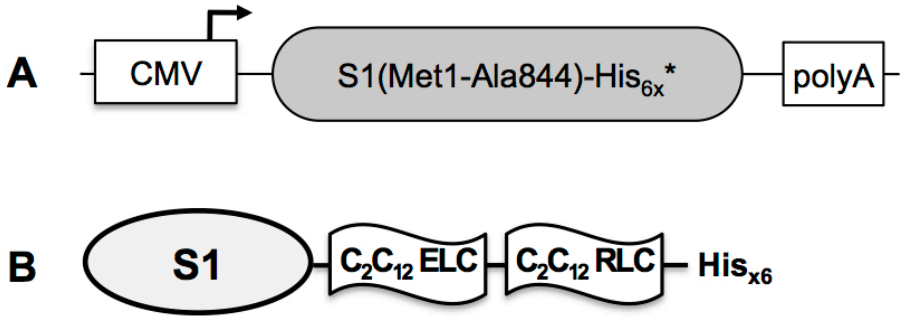

Figure 25: Embryonic-S1 expression construct. ***A.*** Embryonic-S1 spanning methionine-1 through alanine-844 was cloned into pShuttle in frame with 6xHistidine-Stop (*), under transcriptional control of a CMV promotor and upstream of a polyA signal sequence. ***B.*** The protein produced by this expression cassette, Emb-WT, consists of S1 fused at its carboxy terminus with a 6xHistidine purification tag. This protein is expected to copurify with myosin light chains (ELC and RLC) endogenous to the C_2C_{12} cells in which the protein is expressed.

Recombinant adenoviruses encoding these constructs were used to infect myotubes derived from C_2C_{12} mouse myoblasts in culture. Protein production in myotubes was performed as described in Chapter I, then Emb-WT and Emb-R672H S1 proteins were purified from frozen cell pellets by FPLC, also as described in Chapter I.

Stopped-flow measurements

Stopped-flow measurements were performed using a HiTech Scientific SF-61DX2 stopped-flow system. To observe reactions at pre-steady-state, assays were performed in high-

salt buffer: 20 mM MOPS pH 7.0, containing 100 mM KCl, 5 mM $MgCl_2$, and 1 mM DTT. Reactions were performed at 20°C, unless otherwise noted. Measurements were made using fluorescence signals of reaction progress. Data averaging to produce representative fluorescence transients and non-linear regressions of fluorescence transients were performed using the stopped-flow's included software, Kinetic Studio. The MyHC isoforms in this chapter were constructed into S1 proteins without eGFP, to eliminate the signal background observed in Chapter II.

Fluorescence approaches to observing myosin kinetics

As described in detail in Chapter II, two fluorescence signals were used to observe the interactions of S1 and actin-S1 with ATP and ADP in the experiments described in this chapter. For reactions in the presence of actin, pyrene-labeled actin (production described in Chapter II, Methods) was used. Pyrene-actin signals the dissociation of the actin-S1 complex by increasing its fluorescence intensity. Fluorescence from pyrene-actin was excited at 365 nm and the emission, with a maximum at ~407 nm, observed through a KV389 long-pass filter. For reactions in the absence of actin, the intrinsic protein fluorescence of MyHC-S1 proteins was measured by excitation at 295 nm and emission observed through a WG320 long-pass filter. Intrinsic protein fluorescence intensity is known to be modulated in MyHC-S1 proteins in response to nucleotide binding and ATP hydrolysis, as is described in more detail in Chapter II, Methods.

Measuring crossbridge detachment

As described above, pyrene-actin fluorescence intensity is greater in free pyrene-actin than in the pyrene-actin-S1 complex. Therefore, an increase in fluorescence intensity as a result of pyrene-actin dissociation from S1 can be observed following Step 2A of the ATPase cycle

(Figure 13). This dissociation reaction can be induced by the addition of ATP to the pyrene-actin-S1 complex. On the stopped-flow, measurements of ATP-induced actin-S1 dissociation were performed by loading syringe 1 with equimolar pyrene-actin and S1 to form the complex, and loading syringe 2 with ATP. The contents of the two syringes were then rapidly mixed and the signal change observed as the reaction progressed in the flowcell. This reaction is designed to include Steps 1A and 2A, and therefore is dependent upon the affinity of pyrene-actin-S1 for ATP (governed by $1/K_{1A}$) and the rate constant for Step 2A (k_{+2A}).

To observe actin-S1 crossbridge detachment and determine the constants K_{1A} and k_{+2A}, pyrene fluorescence experiments were conducted on the stopped-flow. Syringe 1 was loaded with pyrene-actin and Emb-WT or Emb-R672H S1 to form the pyrene-actin-S1 complex and syringe 2 was loaded with ATP. After mixing on the stopped-flow, pyrene-actin-S1 was at a final concentration of 0.025 μM. Reactions were repeated from 10 μM to as much as 2 mM ATP. These reactions were performed at 20° C, and fluorescence recorded for 1 second after mixing (until the fluorescence signal reached plateau). For these measurements pyrene was excited at 365 nm and a KV389 band-pass filter was used to isolate the pyrene emission signal at ~407 nm. Each reaction was repeated for 3 to 5 mixing events and the traces averaged to produce a single fluorescence trace. Each averaged fluorescence trace was fit by non-linear regression using Equation 2: $F = A \cdot (1 - e^{(-k_{obs} \cdot t)}) + F_{\infty}$, to determine the rate of the observed reaction. k_{obs} values were plotted with respect to ATP concentration. These data were fit using the hyperbolic function, Equation 3B: $k_{obs} = \frac{K_{1A} k_{+2A} [ATP]}{1 + K_{1A} [ATP]}$, as defined above in Chapter II, Methods. These reactions were repeated for two separate preparations of each protein.

Measuring ADP affinity of actin-S1

As described above, the affinity of actin-S1 for ADP can be investigated using the ATP-induced actin-S1 dissociation signal. Since ADP and ATP share the same binding site on S1, ADP can be used as an inhibitor of ATP binding and therefore inhibit dissociation. On the stopped-flow, measurements to determine ADP affinity were performed in two ways.

Emb-WT S1 was analyzed by using ADP as a competitive inhibitor of ATP binding, as described in Chapter II, Methods. These experiments were conducted by observing the pyrene fluorescence signal for actin-S1 dissociation on the stopped-flow. Syringe 1 was loaded with pyrene-actin and Emb-WT S1 to form the pyrene-actin-S1 complex and syringe 2 was loaded with ATP and ADP. After mixing on the stopped-flow, pyrene-actin-S1 was at a final concentration of 25 nM and ATP was at a final concentration of 10 μM. Reactions were performed with no ADP, then repeated with from 5 μM to as much as 400 μM ADP. These reactions were performed at 20° C, and fluorescence recorded for up to 10 seconds after mixing. For these measurements pyrene was excited at 365 nm and a KV389 band-pass filter was used to isolate the pyrene emission signal at ~407 nm. Each reaction was repeated for 3 to 5 mixing events and the traces averaged to produce a single fluorescence trace. Each averaged fluorescence trace was fit by non-linear regression using Equation 2 to determine the rate of the observed reaction. k_{obs} values were plotted with respect to ADP concentration and the resulting plot fit using Equation 5: $\frac{k_{obs}}{k_0} = k_{rel} = \frac{1}{1+([ADP]/K_{5A})}$, as derived and defined in detail in Chapter II, Methods. This set of reactions was repeated for two separate preparations of Emb-WT S1.

Emb-R672H S1 protein binding to ADP was analyzed by pre-incubating pyrene-actin-S1 with ADP in syringe 1 and mixing with ATP in syringe 2, as described for ADP binding to free

S1 in Chapter II, with pyrene fluorescence signaling reaction progress rather than tryptophan fluorescence. On the stopped-flow, measurements of ADP binding to Emb-R672H actin-S1 were performed by loading syringe 1 with Emb-R672H, pyrene-actin, and ADP and loading syringe 2 with ATP. After mixing, Emb-R672H was at a final concentration of 25 nM and ATP was at a final concentration of 10 μM. Reactions were performed with no ADP, then repeated with from 2.5 μM to 40 μM ADP in syringe 1, before mixing. Syringe 1 is expected to contain two populations in the presence of ADP, pyrene-actin-S1 and pyrene-actin-S1-ADP, which are expected to produce a biphasic fluorescence transient where the amplitudes of each phase reflect the relative concentrations of each population, as described in Chapter II, Methods and Results. For these measurements, pyrene fluorescence was excited at 365 nm and a KV389 band-pass filter was used to isolate the pyrene emission signal at ~407 nm. Each reaction was repeated for 3 to 5 mixing events and the traces averaged to produce a single fluorescence trace. Each averaged trace was fit by non-linear regression using the sum of two exponential terms, Equation 4, to determine amplitudes for both fast and slow phases of the reaction traces. The relative amplitudes for the slow and fast phases plotted with respect to ADP concentration were respectively fit using Equations 6A and 6B, with the dissociation constant K_{5A} substituted for K_5: $A = \frac{A_{max}[ADP]}{K_{5A} + [ADP]} + A_{min}$ and $A = \frac{A_{max}K_{5A}}{K_{5A} + [ADP]} + A_{min}$, as defined in Chapter II. These reactions were repeated for two separate preparations of Emb-R672H S1 protein.

To determine the rate constant k_{+5A}, which governs ADP-dissociation from actin-S1, saturating ADP (500 μM for Emb-WT S1 and 50 μM for Emb-R672H S1, before mixing) was pre-incubated with pyrene-actin-S1 and loaded in syringe 1, and syringe 2 was loaded with saturating, 2 mM ATP. These reactions were performed at 20° C, and fluorescence recorded for up to 10 seconds after mixing. For these measurements pyrene was excited at 365 nm and a

KV389 band-pass filter was used to isolate the pyrene emission signal at ~407 nm. These measurements were repeated for 3 mixing events and the traces averaged to produce a single fluorescence trace. The averaged fluorescence traces were fit by non-linear regression using Equation 2 to determine the rate of the observed reaction. With the actin-S1 complex saturated by ADP before mixing, upon mixing with high ATP concentrations k_{obs} is expected to be limited by the maximum rate of ADP-dissociation (governed by k_{+5A}) unless that rate exceeds the rate of ATP binding, in which case k_{obs} will approximate k_{+2A}. Emb-WT was pre-incubated with 400 μM ADP and Emb-R672H was pre-incubated with 40 μM ADP before each were mixed with 2 mM ATP to determine the rate constant of ADP-dissociation from actin-S1, k_{+5A}. The reaction was repeated 3 times and the traces averaged to produce a single fluorescence transient. The transient was fit using the single exponential function, Equation 2.

RESULTS

Purification of Emb-WT and Emb-R672H proteins

Emb-WT and Emb-R672H S1 proteins were purified from frozen infected C_2C_{12} cell pellets, but yielded low protein concentrations. Peak concentrations were 2.0 μM and 1.2 μM in the two Emb-WT preparations used for this work. By SDS-PAGE these purified S1 proteins appeared to copurify with mixed endogenous C_2C_{12} ELC and RLC isoforms, which were seen as bands of ~15 kDa, ~18 kDa, and ~22 kDa (Figure 26).

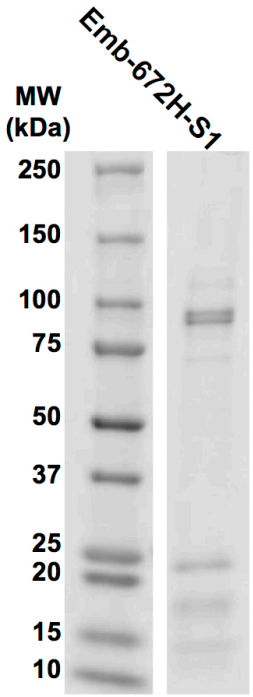

Figure 26: Purified recombinant Emb-R672H S1 protein. SDS-PAGE of the mutant S1 construct appears identical to its wild-type counterpart in both apparent molecular weight and light chain composition and is representative of both purified S1 constructs. Emb-R672H protein runs at the expected size and along with bands of approximately the appropriate size to be C_2C_{12} endogenous myosin light chains, between ~15 and ~25 kDa.

ATP-induced dissociation of actin-S1 (Steps 1A and 2A)

In order to investigate the ATP-induced crossbridge detachment of Emb-WT and Emb-R672H, we wanted to determine the affinity of the actin-S1 complex for ATP in Step 1A and the rate constant, k_{+2A}, governing the rate-limiting step of detachment, the conformational change in Step 2A (Figure 27).

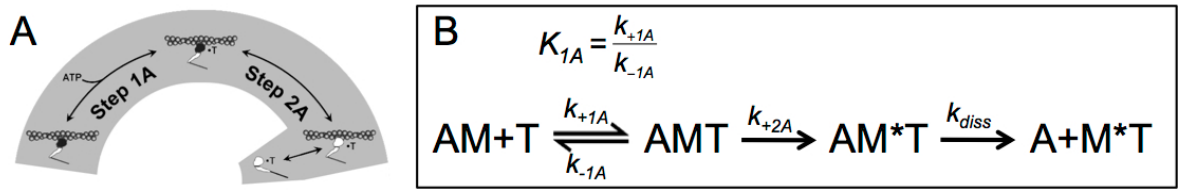

Figure 27: ATP-induced actin-S1 dissociation schemes. The participants in the reactions described are abbreviated as A = actin, M = myosin S1, and T = ATP. M* represents a different conformational state of myosin S1 with low actin affinity. ***A.*** The reaction steps following the mixing of ATP with AM are a rapid equilibrium step where ATP binds to AM (Step 1A) and a rate limiting conformational change (Step 2A) preceding a diffusion limited dissociation (k_{diss}), as described in detail in Chapter II[173, 174]. ***B.*** Step 1A is governed by the association constant K_{1A} and Step 2A is governed by the rate constant k_{+2A}.

Since these reactions occur in the presence of actin, pyrene-actin fluorescence is used to signal dissociation of the actin-S1 complex. As described above, pyrene-actin fluorescence intensity is greater in free pyrene-actin than in the pyrene-actin-S1 complex. Therefore, an increase in fluorescence intensity as a result of pyrene-actin dissociation from S1 can be observed following Step 2A of the ATPase cycle, as described in detail in Chapter II, Results. Dissociation can be induced by mixing pyrene-actin-S1 with ATP on the stopped-flow. Measurements of ATP-induced dissociation of Emb-WT and Emb-R672H actin-S1 were performed on the stopped-flow by loading syringe 1 with equimolar pyrene-actin and S1 to form the complex, and loading syringe 2 with ATP. The contents of the two syringes were then rapidly mixed and pyrene fluorescence observed as the reaction progressed in the flowcell. This reaction is designed to include Steps 1A and 2A, and therefore is dependent upon the affinity of pyrene-actin-S1 for ATP (K_{1A}) and the rate constant for Step 2A (k_{+2A}). ATP concentration was varied in order to observe the reaction at well below the K_D for ATP ($1/K_{1A}$), at saturating ATP concentration, and at sufficient points between the two in order to accurately model the substrate dependence of the reaction rate. Fluorescence transients resulting from these mixing events were monophasic and could be well described by non-linear regression analysis using the single exponential function, Equation 2: $F = A \cdot (1 - e^{(-k_{obs} \cdot t)}) + F_{\infty}$. Figure 28A shows representative traces from Emb-WT and Emb-R672H S1.

At high ATP concentrations, signal was insufficiently distinguishable from noise for Emb-WT, due to low S1 concentrations and the fast reaction rate at high ATP concentrations. The highest measureable concentration for Emb-WT was 500 μM ATP. k_{obs} values from these functions were plotted with respect to ATP concentration and the resulting plots fit using

Equation 3B: $k_{obs} = \frac{K_{1A}k_{+2A}[ATP]}{1 + K_{1A}[ATP]}$ (Figure 28B). For Emb-WT, the fitted function yielded k_{+2A} values with a mean of 808±75 s^{-1}. Since these data were limited to low substrate concentrations, the slope of the initial linear phase was more trusted than the hyperbolic fit, and fitting Equation 7, $k_{obs} = K_{1A}k_{+2A}$ at low ATP concentrations (defined in Chapter II) to the linear phase gave $K_{1A}k_{+2A}$ = 2.7±0.3 $\mu M^{-1}s^{-1}$. For Emb-WT, both calculation using the linear phase fit and the $K_{1/2}$ point from the hyperbolic fit estimated $1/K_{1A}$ = ~300 μM and we therefore report that value as an approximation of $1/K_{1A}$. We also report k_{+2A}, taken from the hyperbolic fit as an approximation of ~800 s^{-1}, given the limitations of the data at high ATP concentrations (Table 4). For Emb-R672H, the fitted hyperbolic function yielded k_{+2A} = 475±31 s^{-1}. The slope of the linear phase of this plot at low ATP concentrations was fit using Equation 7, yielding $K_{1A}k_{+2A}$ = 1.0±0.2 $\mu M^{-1}s^{-1}$. For Emb-R672H, the dissociation constant for ATP was calculated as, $1/K_{1A}$ = ~590 μM (Figure 28, Table 4).

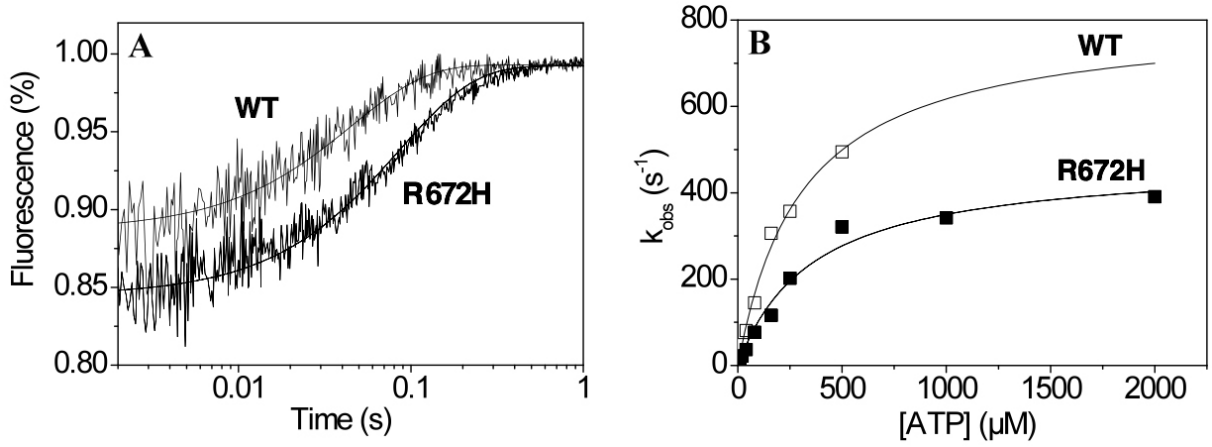

Figure 28: ATP-induced actin-S1 dissociation of Emb-WT and Emb-R672H. ***A.*** Fuorescence transients resulting from rapidly mixing pyrene-actin-S1 with ATP on the stopped-flow to final concentrations of 25 nM pyrene-actin-S1 and 10 μM ATP were fit using Equation 2. ***B.*** Plots of k_{obs} with respect to ATP concentration were fit using Equation 3B. The function fitted to Emb-WT saturates at k_{+2} = 808 s^{-1} and a fit of Equation 7 to the low ATP phase yields $K_{1A}k_{+2A}$ = 2.7 $\mu M^{-1}s^{-1}$. The functions fit to Emb-R672H gave k_{+2A} = 475 s^{-1} and $K_{1A}k_{+2A}$ = 1.0 $\mu M^{-1}s^{-1}$.

ADP inhibition of ATP-induced dissociation of actin-S1 (Step 5A)

In order to investigate the ADP-binding characteristics of Emb-WT and Emb-R672H, we wanted to determine the affinity of the actin-S1 complex for ADP and the rate of ADP release from actin-S1 in Step 5A (Figure 29). To observe these characteristics in the presence of actin we again used pyrene-actin fluorescence to signal the ATP-induced dissociation of the actin-S1 complex, and added ADP to the reactions as a competitive inhibitor of ATP binding.

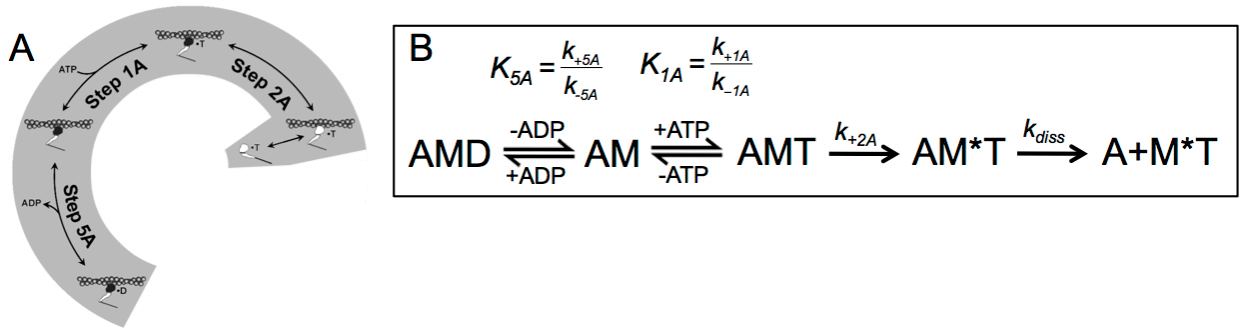

Figure 29: ADP inhibition of ATP-induced actin-S1 dissociation schemes. The participants in the reactions described are abbreviated as A = actin, M = myosin S1, D = ADP and T = ATP. M* represents a different conformational state of myosin S1 with low actin affinity. ***A.*** Reactions where ATP and ADP are mixed with AM lead to two possible reaction paths, where AM may progress through ATP-induced AM dissociation as described above, or may first bind ADP in the reverse reaction of Step 5A. Reactions where ATP is mixed with a pre-incubated solution of ADP and AM follow two reaction paths, where the population of AM in the pre-incubated solution progresses through ATP-induced AM dissociation and the population of AMD first must undergo Step 5A, ADP-dissociation from AMD, before progressing through ATP-induced AM dissociation. ***B.*** Step 5A is governed by the dissociation constant K_{5A}, Step 1A is governed by the association constant K_{1A} and Step 2A is governed by the rate constant k_{+2A}.

As described in detail in Chapter II, ADP can affect the progress of ATP binding reactions with actin-S1 by competitive inhibition. Using this principle, ADP binding to actin-S1 can be indirectly measured in two ways. For Emb-WT, ADP was added to the syringe containing ATP to act as a competitive inhibitor for binding actin-S1. With ATP at a fixed low concentration, well below the K_D of actin-S1 for ATP, ADP concentration was varied in sequential reaction mixtures in order to observe the reaction at well below the K_D of actin-S1 for

ADP (K_{5A}), at saturating ADP concentration, and at sufficient points between the two in order to accurately model the inhibition. Fluorescence transients resulting from these mixing events were monophasic and could be well described by fitting the single exponential function, Equation 2: $F = A \cdot (1 - e^{(-k_{obs} \cdot t)}) + F_{\infty}$. In the absence of ADP, $k_{obs} = 28\ s^{-1}$ was defined as k_0. k_{obs} values were plotted with respect to post-mixing ADP concentration and the plots fitted using Equation 5: $\frac{k_{obs}}{k_0} = k_{rel} = \frac{1}{1 + ([ADP] / K_{5A})}$. A representative plot is shown in Figure 30A. These fits, repeated for two independent preparations of protein, yielded a mean K_{5A} value of 56±6 μM for Emb-WT.

For Emb-R672H, ADP was pre-incubated with the actin-S1 in syringe 1, then mixed with ATP, such that the two populations of actin-S1 in syringe 1, pyrene-actin-S1 and pyrene-actin-S1-ADP, reacted at easily separable rates. As described in detail for S1 in the absence of actin in Chapter II, Results, by analyzing the amplitudes of the two phases of the reaction with respect to ADP concentration it is possible to infer the relative concentrations of the two populations of actin-S1 in syringe 1 before mixing and therefore determine the dissociation constant of actin-S1 for ADP, K_{5A}. Fluorescence transients resulting from these mixing events were biphasic and fit using the sum of two exponential terms, Equation 4. Relative amplitudes for the slow and fast phases were plotted with respect to pre-mixing ADP concentration and fit using Equation 6A: $A = \frac{A_{max}[ADP]}{K_{5A} + [ADP]} + A_{min}$ and Equation 6B: $A = \frac{A_{max} K_{5A}}{K_{5A} + [ADP]} + A_{min}$, respectively. A representative plot is shown in Figure 30B. From these fits to the data, we yielded two K_{5A} values for Emb-R672H, for each preparation of protein, which were averaged and are reported as a single mean K_{5A} value in Table 4.

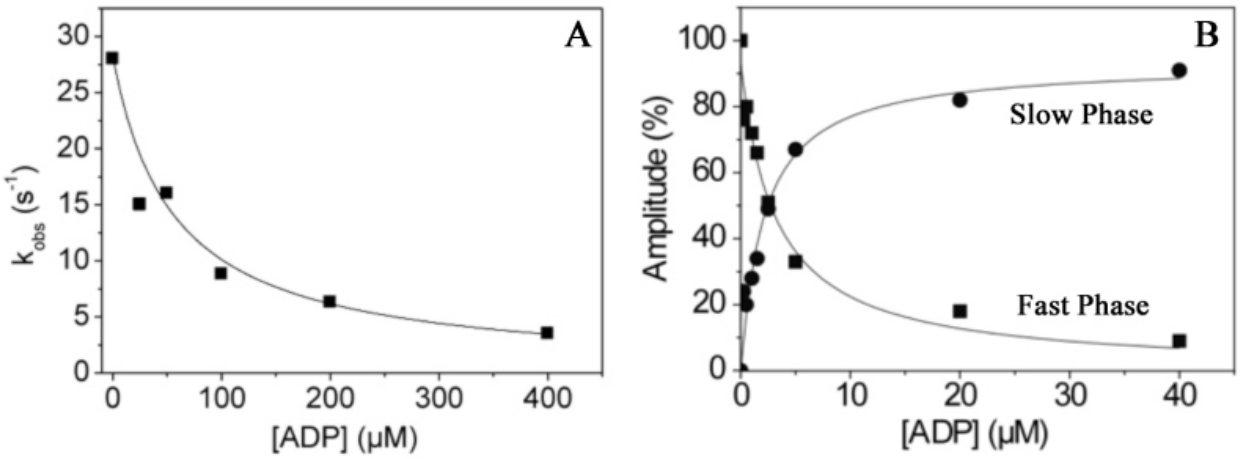

Figure 30: ADP binding to Emb-WT and Emb-R672H S1 proteins. ***A.*** ADP binding to Emb-WT was measured by mixing pyrene-actin-S1 with ATP supplemented with ADP as a competitive inhibitor, from 0 to 400 μM ADP. k_{obs} values were plotted with respect to ADP concentration and fit using Equation 5, yielding K_{5A} = 56 μM for Emb-WT. ***B.*** Emb-R672H pyrene-actin-S1was pre-incubated with ADP, then rapidly mixed with ATP to induce dissociation. The amplitudes of the slow and fast phases were plotted with respect to ADP concentration and fit using Equations 6A and 6B, respectively, yielding K_{5A} = 3.2 and 2.1 μM, respectively. ***C.*** Reaction scheme for the ADP inhibition of ATP-induced actin-S1 dissociation.

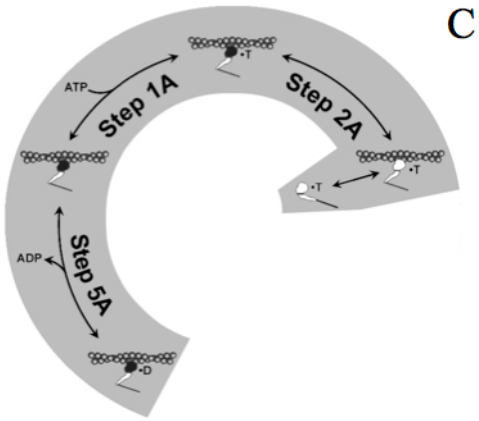

At saturating ADP and excess ATP, k_{obs} will be limited by the rate constant governing ADP-dissociation, k_{+5}, unless that step occurs faster than k_{+2A}. Measurements at these conditions did not separate and define a slower rate of dissociation for Emb-WT in the presence of saturating ADP. For Emb-WT, we interpret this to mean that k_{+5A} does not limit the rate of the ATP-induced dissociation reaction and therefore $k_{+5A} > k_{+2A}$. Using these measurements we can only set a lower limit on the k_{+5A} value for Emb-WT of >200 s^{-1}, at which point the fast rate of reaction and low signal to noise from low S1 protein concentrations made accurate measurements impossible. For the tighter ADP-binding Emb-R672H, the k_{obs} at saturating ADP

separated from k_{+2A}, such that $k_{obs} = k_{+5A} = 12\pm0.2\ s^{-1}$ (Table 4).

	Emb-WT	Emb-R672H	Rabbit fast skeletal S1*	Bovine slow masseter S1#
ATP-binding to actin-S1				
$K_{1A}k_{+2A}$ ($\mu M^{-1}s^{-1}$)	2.7±0.3	1.0±0.2	2.4	1.24
$1/K_{1A}$ (μM)	~300	590±124	520	984
k_{+2A} (s^{-1})	~800	475±31	1250	1220
ADP-binding to actin-S1				
K_{5A} (μM)	56±6	2.6±0.6	120	9.6
k_{+5} (s^{-1})	>200	12±0.2	>1200	94

Table 4: Stopped-flow kinetics of Emb-WT and Emb-R672H. Constants governing the interaction of S1 proteins with ATP, ADP, and pyrene-actin. The mean values for calculated rate and equilibrium constants are given and variance reported as standard error of the mean. (*) Rabbit fast skeletal muscle S1 and (#) Bovine slow masseter muscle S1 are included for reference to previous measurements of fast and slow skeletal isoforms, including data from: [132, 180, 184].

DISCUSSION

Embryonic-MyHC kinetics are similar to those of fast skeletal isoforms

ADP-dissociation and ATP binding, sequentially, must occur in the actin-S1 complex in order for crossbridge detachment to follow. As described above, the kinetics of crossbridge detachment in the MyHC of a muscle fiber are relevant because this step governs the maximum rate of fiber shortening. These results place the human embryonic MyHC isoform among the fast skeletal isoforms described in Chapter II in terms of the kinetics of crossbridge detachment. For the fast skeletal isoforms, IIa, IId, IIb, and extraocular described in Chapter II, the apparent second order rate constant of ATP-induced actin-S1 dissociation, $K_{1A}k_{+2A}$, clustered into two groups. The traditional fast skeletal muscle isoforms, IIa, IId and IIb, agreed closely with one another with a mean value of 1.6 $\mu M^{-1}s^{-1}$, while the specialized isoform, extraocular, was ~2-fold faster at 3.2 $\mu M^{-1}s^{-1}$. Emb-WT is at the faster end of this range: $K_{1A}k_{+2A} = 2.7\ \mu M^{-1}s^{-1}$, primarily due to its high affinity for ATP, $1/K_{1A} = \sim300\ \mu M$, which is a higher affinity (i.e. lower

dissociation constant) than any muscle MyHC isoform measured so far. The other contributor to this second order rate constant, k_{+2A} = 808 s^{-1}, clusters with the lowest value measured for this constant: k_{+2A} = 814 s^{-1} for MyHC-IId. This latter step of ATP-induced actin-S1 dissociation, Step 2A, may therefore control the rate of detachment for embryonic MyHC. One caveat to these conclusions is the low quality of the data for Emb-WT at high ATP concentrations. For this reason, these measurements will be repeated in future work with higher concentration protein preparations to adequately address these areas of the data.

ADP-release is known to determine the rate of crossbridge detachment of slow isoforms[49]. Past studies of myosins isolated from chicken embryos concluded that developmentally expressed MyHC isoforms were slow in steady-state[155]. This led to the hypothesis that human embryonic MyHC would function kinetically in a similar manner to slow isoforms, such as bovine masseter myosin-S1, which binds ADP tightly enough for ADP-dissociation to limit its rate of crossbridge detachment. However, the ADP-affinity of Emb-WT is more similar to the fast skeletal isoforms rather than to the slow masseter-S1. Among the fast skeletal isoforms discussed in Chapter II, the embryonic isoform binds ADP most similarly to the tightest binding fast skeletal isoform, IIb, which in many respects was similar to a slow myosin, and so Emb-WT can be placed somewhere between fast and slow categories in terms of ADP-affinity. While the rate constant governing ADP-dissociation from Emb-WT actin-S1, k_{+5A}, could not be determined precisely, its measurement at >200 s^{-1} may indicate that it exceeds that of the ATP-binding step (limited by Step 2, k_{+2A}), which would further categorize it with the fast skeletal isoforms.

Together, these results for embryonic-MyHC S1 describe a myosin with fast detachment kinetics and which likely does not bind ADP tightly enough to limit its rate of crossbridge detachment. This pattern is typical of fast skeletal myosins, rather than the slow isoforms with

which previous studies predicted the embryonic isoform would share its activity. The results which led to this prediction, published by Lowey, et al., were based on *in vitro* motility measurements. The rate-limiting step governing this assay and therefore their conclusions may be a step of the ATPase cycle not measured for Emb-WT in this study, such as the ATP-hydrolysis step. Previous work carried out by Daniel R. Resnicow in the Leinwand lab in collaboration with Hans Warrick in the Spudich lab at Stanford tested the *in vitro* motility of purified embryonic-eGFP-S1, produced also for the ATPase experiments in Chapter I. These measurements agreed with the work of Lowey, et al. that the embryonic isoform was among the slowest isoforms by *in vitro* motility[2]. Further study of Emb-WT to characterize more steps in its ATPase cycle should be able to clarify these conflicting conclusions.

Functional alterations in embryonic-S1 resulting from the R672H mutation

The contractile class into which these results place the human embryonic MyHC isoform is that of a fast skeletal type. The ability of MyHC isoforms of this type to generate and sustain contractile tension is dependent upon a high frequency of contraction. Embryonic muscles are not known to be very active, so we can conclude that this motor is unlikely to be intended to generate or sustain tension.

The alterations to the kinetics of Emb-WT resulting from the R672H mutation change its contractile class. The R672H mutation results in a nearly 3-fold decrease in the apparent second order rate constant for ATP-induced actin-S1 dissociation, from $K_{1A}k_{+2A}$ = 2.7 to 1.0 $\mu M^{-1}s^{-1}$, which was contributed to by a nearly 2-fold drop in ATP affinity, from $1/K_{1A}$ = ~300 to 590 μM, as well as by a nearly 2-fold drop in k_{+2A}, from ~800 s^{-1} to 475 s^{-1} for Emb-WT and Emb-R672H, respectively (Figure 31). Most strikingly, R672H had a large effect on ADP binding to actin-S1, increasing ADP affinity ~20-fold, from K_{5A} = 56 μM to 2.6 μM, leading to a decrease in the rate

constant for ADP-dissociation of at least ~20-fold, from k_{+5A} > 200 s^{-1} to 12 s^{-1}. If the rate of ADP-dissociation for Emb-WT is in fact in excess of the rate limiting step of ATP binding, k_{+2A}, then the decrease in this constant in Emb-R672H could be as much as ~70-fold, from k_{+2A} = ~800 s^{-1} for Emb-WT to k_{+5A} = 12 s^{-1} for Emb-R672H.

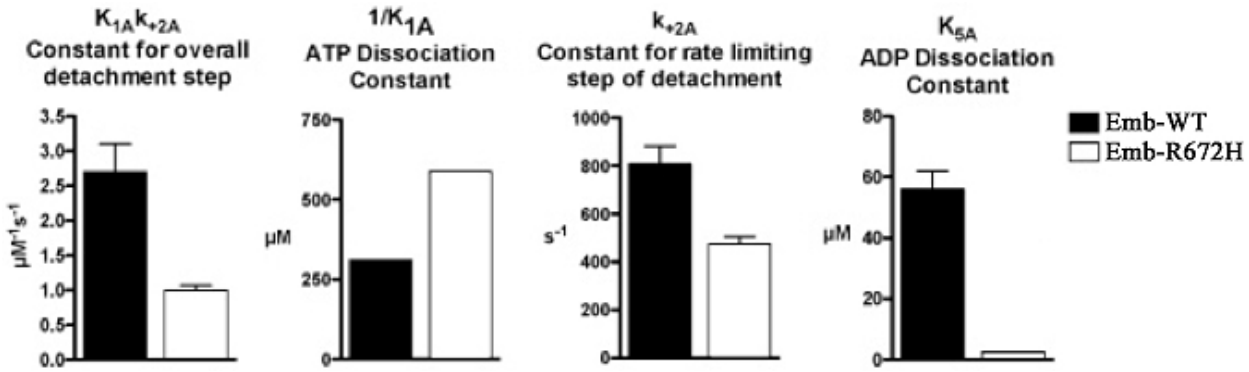

Figure 31: Relative rate and equilibrium constants for Emb-WT and Emb-R672H. The alterations imparted on the contractile kinetics of Emb-WT as a result of the R672H mutation are shown graphically: A nearly 3-fold decrease in ATP-induced cross-bridge detachment, $K_{1A}k_{+2A}$, a nearly 2-fold decrease in ATP affinity, K_{1A}, a nearly 2-fold decrease in maximal rate of detachment, k_{+2A}, and a ~20-fold increase in ADP affinity, K_{5A}. Most detrimentally, the rate constant governing ADP-dissociation is decreased at least ~20-fold. These alterations all contribute to extending the lifetime of the cross-bridge.

These defects all influence the crossbridge detachment reaction in such a way as to elongate the lifetime of the actin-bound phase of the ATPase cycle. By comparison with the fast and slow S1 kinetics in Table 4, Emb-WT shares most kinetic features in common with rabbit fast skeletal muscle S1. Emb-R672H appears most similar to the bovine slow masseter muscle S1, but with nearly 10-fold slower ADP-dissociation than even the classic "slow" S1 from bovine masseter. In a muscle environment where Emb-WT is adapted to have fast detachment kinetics, as these data indicate is likely the case in embryonic muscle, the extension of the crossbridge lifetime at least 20-fold is expected to have major consequences. Interestingly, the disease caused by the R672H mutation is of the class of contracture disorders, which produces a phenotype in which muscles of the face and distal limbs seem to be irreversibly contracted.

Although this *in vitro* system is not sufficient for predicting the consequences of Emb-R672H kinetics *in vivo*, it is conceivable that a crossbridge detachment defect in a major myosin of embryonic muscles leads to the inability of the muscles to release tension during development, and could thereby contribute to the formation of distal joint and facial muscle contractures.

This large alteration of ADP binding and the location of the altered residue in the core of the protein, near the active site of the motor domain make this mutation a good candidate for structure versus function studies aimed at determining the structural determinants of ADP affinity and dissociation.

CHAPTER IV

Pre-steady-state cardiac muscle myosin kinetics

INTRODUCTION

Cardiac MyHC isoforms

The two MyHC isoforms in human cardiac muscle, α- and β-, share 91% amino acid identity in S1[192]. Due to this high degree of identity, it was hypothesized that the contractile kinetics of these isoforms would be quite similar. However, steady-state measurements of their ATPase as well as *in vitro* motility indicate 2- to 3-fold differences between α- and β-MyHC, with α-MyHC being the faster of the two[165]. No previous studies of α-MyHC before this work have measured α-MyHC pre-steady-state kinetics, though several kinetic studies have been performed on slow muscle β-MyHC from species other than human[132, 133, 186].

In the healthy human heart ventricle, MyHC composition is ~90% β and 10% α. The importance of the small proportion of α in the human heart is emphasized by the effects of certain cardiac disease states, where α-MyHC becomes undetectable[167]. The loss of detectable α-MyHC in the heart is correlated with loss of contractile function. Following pharmacological intervention, α-MyHC becomes detectable again only in the hearts of patients with improved cardiac function[167, 193, 194]. Animal models produced to investigate the result of variations in the α- and β-MyHC balance in the heart indicate that this balance of MyHC expression has a strong influence on the contractile function of isolated muscle fibers and cardiac myocytes[168-172].

Disease-causing mutations in cardiac MyHC

Greater than 300 mutations in β-MyHC are known to cause various cardiac and skeletal muscle diseases[195]. Determining how mutations affect the contractile properties of the motor

may contribute both to understanding the molecular origins of the disease phenotypes as well as to understanding the differences between the cardiac and skeletal contractile niches. In this study the disease-causing mutation in β-MyHC, R453C, is examined. The residue arginine-453 is located at the edge of the nucleotide-binding pocket, approximately 29 Å from the catalytic site. It lies on the surface of the motor domain, facing the actin-binding pocket[196] (Figure 32). Because of this location it is thought to play a role in actin binding, nucleotide binding, and/or communication between the two sites. R453C is a dominant mutation found in β-MyHC, which causes hypertrophic cardiomyopathy (HCM)[197]. HCM is a severe form of heart disease characterized by a disproportionate thickening of the ventricle walls such that the chamber space becomes restricted and cardiac output is decreased. This is associated with cardiac myocellular disarray and fibrosis and is the most common cause of sudden cardiac death in people under 35 years of age[197-199]. HCM can be inherited through mutations in sarcomeric proteins, such as β-MyHC[200, 201]. In this study the effects of the R453C mutation on human β-MyHC kinetics are examined.

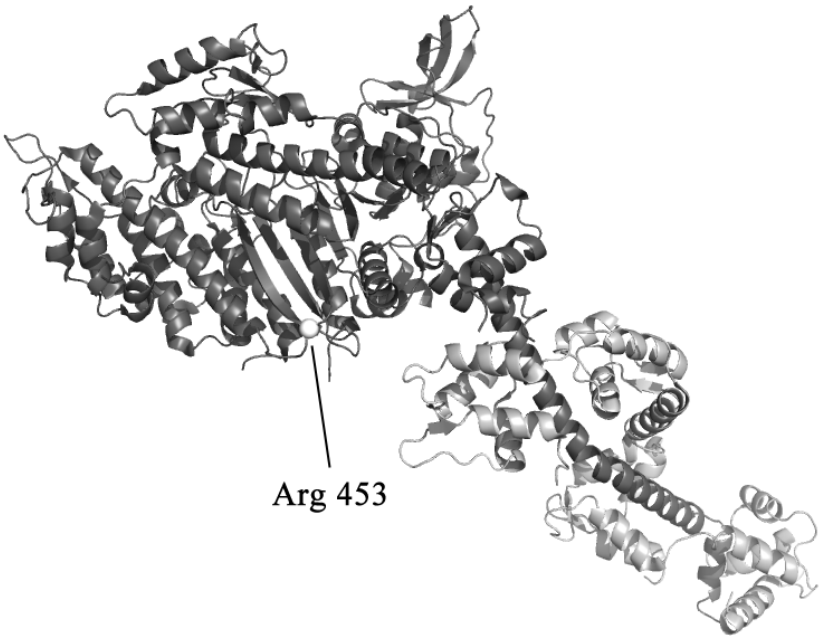

Figure 32: Arginine-453 in myosin S1. Arginine-453 of human β-MyHC (white sphere), lies at the edge of the nucleotide-binding pocket of S1 (dark grey), facing the actin-binding site. When this site in the human β-MyHC gene is mutated, altering this residue to cysteine, it is known to cause hypertrophic cardiomyopathy. Shown within the crystal structure of PDB ID: 1QV1.

METHODS

Production of recombinant cardiac MyHC subfragments

Human α- and β-MyHC were cloned from human heart cDNA. The regions encoding S1, including methionine-1 through alanine-843, with respect to the human β-MyHC sequence (alanine-845 in α-MyHC), were subcloned into pShuttle, in frame with a 6x histidine-tag at the carboxy terminus, prior to the translation stop codon (Figure 33A). These cloning vectors were used to produce recombinant adenoviruses using the methods described in Chapter I, which encoded the protein constructs β-S1 and α-S1.

To study a totally humanized cardiac myosin, a shorter subfragment of MyHC, analogous to chymotrypsin-digested MyHC, was produced by subcloning the region encoding methionine-1 through arginine-808 of β-MyHC, followed by a translation-stop codon, into the multiple cloning site of pShuttle. This cloning vector was used to produce a recombinant adenovirus encoding the protein construct, β-sS1. To investigate the effects of having the correct human cardiac light chain on the function of the motor domain, the human ventricular ELC, MYL3, was cloned from human heart cDNA into pShuttle, in frame with a sequence encoding a start codon and 6x histidine-tag at the amino terminus. This cloning vector was used to produce a recombinant adenovirus encoding the protein, MYL3.

α- and β-S1 proteins were produced in myotubes independently, and both were purified by affinity to the 6x histidine-tag on the carboxy terminus of S1. α- and β-S1 proteins co-purified with endogenous C_2C_{12} myosin light chains. β-sS1, with no affinity tag, and MYL3, with a 6x histidine-tag on its amino terminus, were coexpressed, and purification by affinity to the 6x histidine-tag isolated β-sS1 only as a heterodimer with MYL3 (Figure 33B). Recombinant adenoviruses encoding β-sS1 and MYL3 were used to co-infect myotubes at a 1:1

ratio. This sS1 construct was tested in conjunction with β-S1 to compare the effects on kinetics of β-MyHC complexed with ELC endogenous to the heart, compared with β-MyHC complexed with C_2C_{12} mouse light chains.

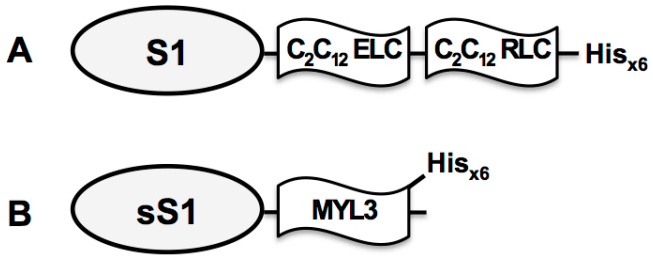

Figure 33: Protein constructs for recombinant cardiac S1 and sS1. ***A.*** Cardiac S1 constructs contain residues Met-1 through Ala-843, with respect to the human β sequence, are C-terminally 6x histidine-tagged and copurify with endogenous C_2C_{12} light chains. ***B.*** β-sS1 contains residues Met-1 through Arg-808, lacking the RLC binding domain, and is coexpressed along with the human ventricular ELC, MYL3, to produce a heterodimer more similar to how β-MyHC is found in the human heart.

The point mutation R453C was inserted into the coding region of β-sS1 in the pShuttle vector using PCR primers containing single nucleotide mismatches, overlapping the mutation target sequence, to introduce the point mutation into PCR products. Using these PCR products, the S1 cloning region was reproduced by recombinant PCR and reinserted into pShuttle, in frame with the 6x histidine-tag. This pShuttle vector was used to produce recombinant adenovirus encoding β-R453C-sS1.

Stopped-flow measurements

Stopped-flow measurements were performed using a HiTech Scientific SF-61DX2 stopped-flow system. To observe reactions at pre-steady-state, assays were performed in high-salt buffer: 20 mM MOPS pH 7.0, containing 100 mM KCl, 5 mM $MgCl_2$, and 1 mM DTT. Reactions were performed at 20°C, unless otherwise noted. Measurements were made using fluorescence signals of reaction progress. Data averaging to produce representative fluorescence transients and non-linear regressions of fluorescence transients were performed using the

stopped-flow's included software, Kinetic Studio. The MyHC isoforms in this chapter were constructed into S1 proteins without eGFP, to eliminate the signal background observed in Chapter II.

Fluorescence approaches to observing myosin kinetics

As described in detail in Chapter II, two fluorescence signals were used to observe the interactions of S1 and actin-S1 with ATP and ADP in the experiments described in this chapter. For reactions in the presence of actin, pyrene-labeled actin was used. Pyrene-actin signals the dissociation of the actin-S1 complex by increasing its fluorescence intensity. Fluorescence from pyrene-actin was excited at 365 nm and the emission, with a maximum at ~407 nm, observed through a KV389 long-pass filter. For reactions in the absence of actin, the intrinsic protein fluorescence of MyHC-S1 proteins was measured by excitation at 295 nm and emission observed through a WG320 long-pass filter. Intrinsic protein fluorescence intensity is known to be modulated in MyHC-S1 proteins in response to nucleotide binding and ATP hydrolysis, as is described in detail in Chapter II, Methods.

Measuring crossbridge detachment

As described above, pyrene-actin fluorescence intensity is greater in free pyrene-actin than in the pyrene-actin-S1 complex. Therefore, an increase in fluorescence intensity as a result of pyrene-actin dissociation from S1 can be observed following Step 2A of the ATPase cycle (Figure 13, discussed in detail in Chapter II, Methods and Results). This dissociation reaction can be induced by the addition of ATP to the pyrene-actin-S1 complex. On the stopped-flow, measurements of ATP-induced actin-S1 dissociation were performed by loading syringe 1 with equimolar pyrene-actin and S1 to form the complex, and loading syringe 2 with ATP. The contents of the syringes were then rapidly mixed and the signal change observed as the reaction

progressed in the flowcell. This reaction is designed to include Steps 1A and 2A, and therefore is dependent upon the affinity of pyrene-actin-S1 for ATP (governed by $1/K_{1A}$) and the rate constant for Step 2A (k_{+2A}).

To observe actin-S1 crossbridge detachment and determine the constants K_{1A} and k_{+2A}, pyrene fluorescence experiments were conducted on the stopped-flow. Syringe 1 was loaded with pyrene-actin and α- or β-S1 to form the pyrene-actin-S1 complex and syringe 2 was loaded with ATP. After mixing on the stopped-flow, pyrene-actin-S1 was at a final concentration of 0.1 μM. Reactions were repeated from 5 μM to as much as 2 mM ATP, post-mixing. These reactions were performed at 20° C, and fluorescence recorded for 1 second after mixing (until the fluorescence signal reached plateau). For these measurements pyrene was excited at 365 nm and a KV389 band-pass filter was used to isolate the pyrene emission signal at ~407 nm. Each reaction was repeated for 3 to 5 mixing events and the traces averaged to produce a single fluorescence trace. Each averaged fluorescence trace was biphasic and so was fit by non-linear regression using Equation 4: $F = A_{fast} \cdot (1 - e^{(-k_{obs(fast)} \cdot t)}) + A_{slow} \cdot (1 - e^{(-k_{obs(slow)} \cdot t)}) + F_{\infty}$, to determine the rates present in the observed reaction. k_{obs} values were plotted with respect to ATP concentration and the fast phase was fit using the hyperbolic function, Equation 3B: $k_{obs} = \frac{K_{1A} k_{+2A} [ATP]}{1 + K_{1A} [ATP]}$, as defined above in Chapter II, Methods. These reactions were repeated for three separate preparations of each protein.

Measuring ADP binding to actin-S1

As described above, the affinity of actin-S1 for ADP can be investigated using the ATP-induced actin-S1 dissociation signal. Since ADP and ATP share the same binding site on S1, ADP can be used as an inhibitor of ATP binding and therefore inhibit dissociation. These

experiments were conducted by observing the pyrene fluorescence signal for actin-S1 dissociation on the stopped-flow. Syringe 1 was loaded with pyrene-actin and α- or β-S1 to form the pyrene-actin-S1 complex and syringe 2 was loaded with ATP and ADP. After mixing on the stopped-flow, pyrene-actin-S1 was at a final concentration of 0.1 μM and ATP was at a final concentration of 25 μM for α-S1 or 50 μM for β-S1. Reactions were performed with no ADP, then repeated with from 2.5 μM to as much as 640 μM ADP for α-S1, or 320 μM ADP for β-S1, post-mixing. These reactions were performed at 20° C, and fluorescence recorded for up to 10 seconds after mixing. For these measurements pyrene was excited at 365 nm and a KV389 band-pass filter was used to isolate the pyrene emission signal at ~407 nm. Each reaction was repeated for 3 to 5 mixing events and the traces averaged to produce a single fluorescence trace. Each averaged fluorescence trace was fit by non-linear regression using Equation 4 to determine the rates present in the observed reaction. k_{obs} values for the fast phase were plotted with respect to ADP concentration and the resulting plot fit using Equation 5: $\frac{k_{obs}}{k_0} = k_{rel} = \frac{1}{1+([ADP]/K_{5A})}$, as derived and defined in detail in Chapter II, Methods. This set of reactions was repeated for three separate preparations each protein.

To determine the rate constant k_{+5A}, which governs ADP-dissociation from actin-S1, saturating ADP was pre-incubated with pyrene-actin-S1 and loaded in syringe 1, and syringe 2 was loaded with excess ATP. These reactions were performed at 20° C, and fluorescence recorded for up to 10 seconds after mixing. For these measurements pyrene was excited at 365 nm and a KV389 band-pass filter was used to isolate the pyrene emission signal at ~407 nm. These measurements were repeated for 3 mixing events and the traces averaged to produce a single fluorescence trace. The averaged biphasic fluorescence traces were fit by non-linear

regression using Equation 4 to determine the rates present in the observed reaction. With the actin-S1 complex saturated by ADP before mixing, upon mixing with high ATP concentrations k_{obs} is expected to be limited by the maximum rate of ADP-dissociation (governed by k_{+5A}) unless that rate exceeds the rate of ATP binding, in which case k_{obs} will approximate k_{+2A}.

Measuring ATP binding and hydrolysis by S1 in the absence of actin

In the absence of actin, measurements can be made using intrinsic protein fluorescence from tryptophan residues in S1. As described in detail in Chapter II, changes in tryptophan fluorescence intensity are known to signal conformational changes in S1 proteins in response to 1) binding ATP and 2) hydrolyzing ATP to ADP and P_i.[76, 126, 183-185]. On the stopped-flow, measurements of ATP binding to S1 in the absence of actin were performed by loading syringe 1 with S1 and loading syringe 2 with ATP. The contents of the two syringes were then rapidly mixed and the tryptophan fluorescence signal change observed as the reaction progressed in the flowcell. After mixing, S1 was at a concentration of 0.25 μM. Reactions were repeated from 5 μM to 500 μM (IIa, IIb, IId) or 1 mM ATP (extraocular) after mixing. These reactions were performed at 20° C, and fluorescence recorded for up to 5 seconds after mixing. For these measurements, tryptophan fluorescence was excited at 295 nm and a WG320 band-pass filter was used to isolate the tryptophan emission signal at ~348 nm. Each reaction was repeated for 3 to 5 mixing events and the traces averaged to produce a single fluorescence trace. Each averaged fluorescence trace was fit by non-linear regression using Equation 2 for monophasic transients or Equation 4 for biphasic transients. k_{obs} values were plotted with respect to ATP concentration and the plots fit by non-linear regression using Equation 3A. To determine which reaction step in the ATPase cycle each phase of the fluorescence transients represent, a second method of quantifying ATP hydrolysis rate was used (quench-flow), which is described below.

Measuring ADP binding to S1 in the absence of actin

As described in Chapter II, ADP binding to S1 directly gives a weak tryptophan signal change, and so ADP binding is instead investigated by its inhibition of ATP binding. Since ADP also binds the nucleotide-binding site on S1, it can block ATP binding, and therefore inhibit the appearance of the ATP binding tryptophan signal. On the stopped-flow, measurements of ADP binding to S1 in the absence of actin were performed by loading syringe 1 with S1 pre-incubated with ADP, and loading syringe 2 with ATP. After mixing, S1 was at a final concentration of 0.2 μM and ATP was at a final concentration of 100 μM. Reactions were performed with no ADP, then repeated with from 0.1 μM to as much as 1.6 μM ADP for β-S1 or 20 μM ADP for α-S1 in syringe 1, before mixing. At the moment of mixing, two populations are expected be present in syringe 1: free S1 and S1-ADP, in proportion to each isoform's affinity for ADP (governed by K_5) and the concentration of ADP in syringe 1. These populations are expected to react at two different rates when mixed with ATP: rapidly inducing a signal in the free S1, but waiting for ADP-dissociation (Step 5) to occur before binding the S1-ADP population and producing a fluorescence signal. The amplitudes of these two phases of the reaction are expected to reflect the relative concentrations of the two populations in syringe 1 and can therefore be used to determine K_5.

These reactions were performed at 20° C, and fluorescence recorded for up to 10 seconds after mixing, using a logarithmic timebase for data collection to enhance resolution of the faster phase of the reaction, while also measuring with sufficient resolution the far slower phase of the reaction. For these measurements, tryptophan fluorescence was excited at 295 nm and a WG320 band-pass filter was used to isolate the tryptophan emission signal at ~348 nm. Each reaction was repeated for 3 to 5 mixing events and the traces averaged to produce a single fluorescence

trace. Each averaged fluorescence trace was fit by non-linear regression using the sum of two exponential terms, Equation 4, to determine amplitudes for both fast and slow phases of the reaction traces. The relative amplitudes for the slow and fast phases were plotted with respect to ADP concentration, and were respectively fit using Equation 6A: $A = \frac{A_{max}[ADP]}{K_5 + [ADP]} + A_{min}$ and Equation 6B: $A = \frac{A_{max}K_5}{K_5 + [ADP]} + A_{min}$ [2, 132, 133].

To determine the rate constant governing ADP-dissociation, the S1 in syringe 1 can be saturated by ADP, then mixed with saturating ATP to maximize the rate of signal appearance after ADP-dissociation. Under these conditions, the rate of the observed reaction should be governed by the rate constant for ADP-release, k_{+5}, unless that constant is greater than that of the rate-limiting step of ATP binding, k_{+2}.

Measuring S1 binding to F-actin

Pyrene-actin fluorescence signal is quenched in the pyrene-actin-S1 complex. The amplitude of a dissociation reaction, coming only from the population of pyrene-actin in complex with S1 before mixing with ATP, must be related to the affinity of the S1 isoform for pyrene-actin. This affinity can therefore be measured by incubating a fixed concentration of pyrene-actin with varied concentrations of S1, from limiting to excess, in syringe 1 and rapidly mixing the resulting complex with a fixed, low concentration of ATP in syringe 2 (low ATP is used to give a slower reaction rate and therefore a more easily characterized fluorescence transient).

On the stopped-flow, actin-affinity was investigated by loading 30 nM pyrene-actin in syringe 1, pre-incubated with S1, and loading ATP in syringe 2. After mixing, ATP was at 20 μM. These measurements were repeated with S1 at concentrations of from 10 nM to 800 nM for

α-S1, or to 650 nM for β-S1, before mixing. Reactions were performed at 20° C. Each reaction was repeated for 3 to 5 mixing events, and the resulting fluorescence traces averaged to produce a single average fluorescence transient. These biphasic averaged fluorescence transients were fit using Equation 4. Amplitudes for the fast phase of the reaction were plotted with respect to S1 concentration. Due to limitations on the S1 concentrations and quantities our system was able to produce, these plots were not expected to reach saturation for observable concentrations of pyrene-actin, so the plots were fit using the quadratic function:

Equation 8: $$A = \frac{[S1] + K_D + [actin] - \sqrt{([S1] + K_D + [actin])^2 - \frac{4}{[S1][actin]}}}{2[actin]},$$

where "A" is the fraction of actin bound to S1 and "K_D" is the dissociation constant of S1 for actin, $K_{D(Actin)}$, as described in Bloemink, et al. (2007)[132]. This method was applied also with the addition of saturating 500 μM ADP to the actin-S1 complex prior to mixing to give the dissociation constant of S1-ADP for actin, $K_{D(ADP\text{-}Actin)}$[178].

Quench-flow measurements

Pre-steady-state measurements of the ATP hydrolysis step were also made by quench-flow. Quench-flow systems allow for rapid mixing of reagents followed by quenching quickly enough to capture the burst phase of product formation. While this method is highly regarded for characterizing the hydrolysis step of myosins, its high demand on protein quantity makes complete characterizations impractical, given limitations in protein production. Therefore only those experiments necessary to complement stopped-flow measurements were performed using this technique. Quench-flow experiments were performed using a Hi-Tech RQF-63. Measurements were made in high salt buffers: 20 mM MOPS pH 7.0, containing 100 mM KCl, 5 mM $MgCl_2$ and 1 mM DTT. S1 was mixed with ten-fold excess ATP and incubated at 20° C

for various time points (10–500 ms), then quenched by 1:1 addition of 6.25% (w/v) trichloro-acetic acid. After neutralization with NaOH, reaction solutions were centrifuged at 3,000 x g for 5 minutes to remove any precipitates. ADP and ATP were separated by HPLC using a Hypersil ODS (3 lm) column by isocratic flow. ADP and ATP associated peaks were quantified by integrating peak areas. For each time point, product formation was determined as a fraction of the peak areas: $\frac{\text{ADP}}{\text{ADP} + \text{ATP}}$. This fraction was used to calculate the absolute concentration of product formed from the initial nucleotide concentration, and this value was used to calculate the hydrolysis rate for S1. Reactions were performed in triplicate and on two separate preparations of protein.

RESULTS

Purification of cardiac MyHC subfragment proteins

Recombinant human cardiac MyHC α-S1, β-S1, and β-sS1 proteins were purified by FPLC, as described in Chapter I. Using SDS-PAGE with Imperial Protein Stain [Thermo], MyHC subfragments appear at expected molecular weights: ~98 kDa for α- and β-S1, and ~93 kDa for β-sS1. α- and β-S1 subfragments co-purify with bands of the appropriate size for mouse ELC and RLC isoforms (~18 kDa and ~22 kDa). β-sS1 co-purifies with the recombinant human ventricular isoform of ELC, MYL3 (~25 kDa) (Figure 34).

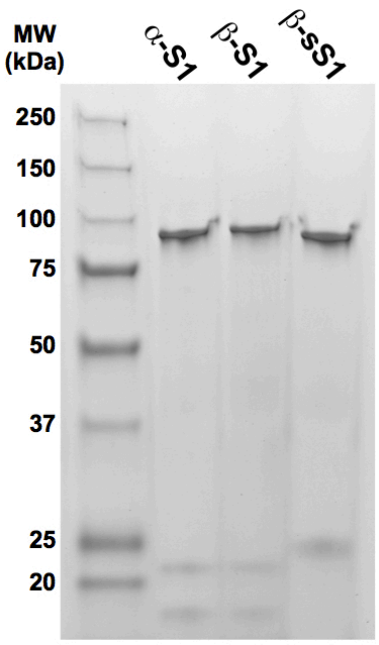

Figure 34: Purified recombinant cardiac MyHC subfragments. SDS-PAGE of recombinant α-S1, β-S1, and β-sS1 with MYL3, stained with Imperial Protein Stain [Thermo] and run along side the molecular weight marker, Precision Plus Protein Standards [Bio-Rad] shows bands corresponding to S1 in lanes 2 and 3 (~98 kDa) and to sS1 in lane 4 (~93 kDa). Bands of the appropriate size for copurified ELC and RLC proteins are present in lanes 2 and 3 (<20 and ~22 kDa) and a single band of the appropriate size for MYL3 is present in lane 4 (~25 kDa). Published in similar form in Deacon, et al. (2012)[2].

ATP-induced dissociation of actin-S1 (Steps 1A and 2A)

In order to investigate the ATP-induced crossbridge detachment of the cardiac myosins, we wanted to determine the affinity of the actin-S1 complex for ATP in Step 1A and the rate constant, k_{+2A}, which governs the rate-limiting step of detachment, the conformational change in Step 2A (Figure 35).

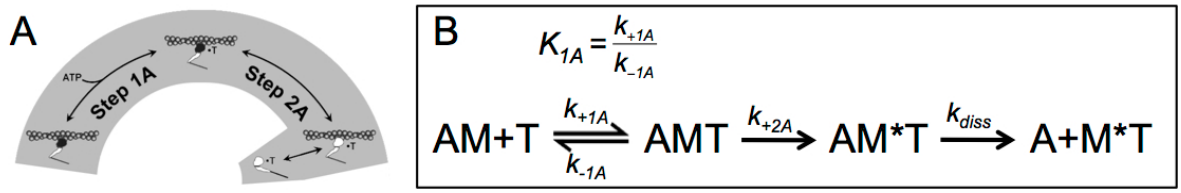

Figure 35: ATP-induced actin-S1 dissociation schemes. The participants in the reactions described are abbreviated as A = actin, M = myosin S1, and T = ATP. M* represents a different conformational state of myosin S1 with low actin affinity. ***A.*** The reaction steps following the mixing of ATP with AM are a rapid equilibrium step where ATP binds to AM (Step 1A) and a rate limiting conformational change (Step 2A) preceding a diffusion limited dissociation (k_{diss})[173, 174]. ***B.*** Step 1A is governed by the association constant, K_{1A}, and Step 2A is governed by the rate constant, k_{+2A}.

These reactions occur in the presence of actin. Actin-associated reactions can be examined on the stopped-flow by observing pyrene-actin fluorescence. As described above, pyrene-actin fluorescence intensity is greater in free pyrene-actin than in the pyrene-actin-S1 complex. Therefore, an increase in fluorescence intensity as a result of pyrene-actin dissociation from S1 can be observed following Step 2A of the ATPase cycle, as described in detail in Chapter II (Figure 35). This dissociation reaction can be induced by the addition of ATP to the pyrene-actin-S1 complex. On the stopped-flow, measurements of ATP-induced actin-S1 dissociation were performed by loading syringe 1 with equimolar pyrene-actin and S1 to form the complex, and loading syringe 2 with ATP. The contents of the two syringes were then rapidly mixed, and pyrene fluorescence observed as the reaction progressed in the flowcell. This reaction is designed to include Steps 1A and 2A, and therefore is dependent upon the affinity of pyrene-actin-S1 for ATP (governed by $1/K_{1A}$) and the rate constant for Step 2A (k_{+2A}).

ATP concentration was varied in order to observe the reaction at well below the K_D of actin-S1 for ATP ($1/K_{1A}$), at saturating ATP concentration, and at sufficient points between the two in order to accurately model the substrate dependence of the reaction rate. Fluorescence transients resulting from these mixing events were biphasic and were well described by non-linear regression analysis using the sum of two exponential functions, Equation 4. Figure 36A shows representative traces from α- and β-S1. k_{obs} for both the fast and slow phases of the observed reactions were plotted with respect to ATP concentration. The rate of the fast phase showed a hyperbolic dependence on ATP concentration, while the slow phase was not dependent on ATP concentration. The fast phases for α- and β-S1 were fit using Equation 3B:

$$k_{obs} = \frac{K_{1A}k_{+2A}[ATP]}{1 + K_{1A}[ATP]}$$ (Figure 36B).

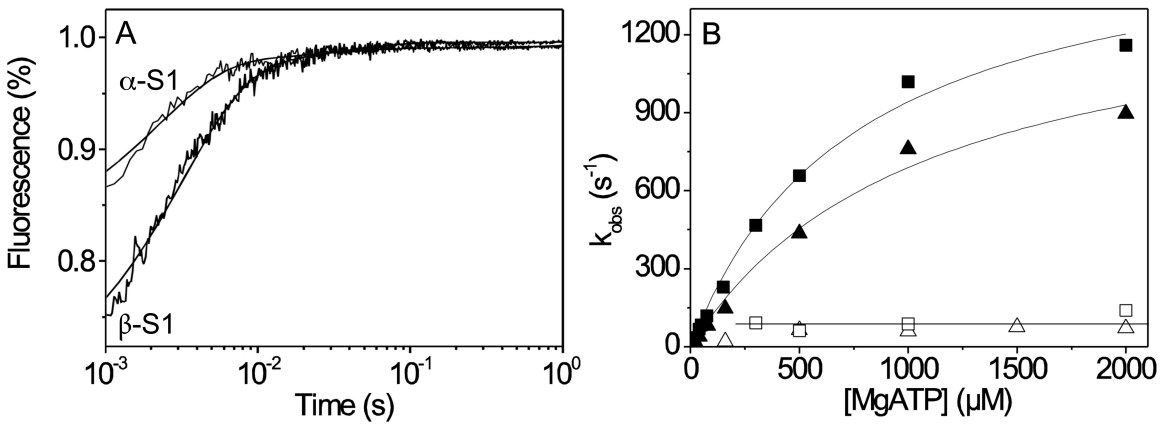

Figure 36: ATP-induced actin-S1 dissociation of α- and β-S1. ***A.*** Fluorescence transients observed after rapidly mixing pyrene-actin-α- or β-S1 with ATP, to final concentrations of 0.1 μM and 0.5 mM, respectively, were best fit by the sum of two exponential functions, Equation 4. ***B.*** Plots of k_{obs} with respect to ATP concentration for the fast phases of α- (■) and β-S1 (▲) showed hyperbolic dependence on ATP concentration, saturating at 1667 and 1432 s^{-1}, respectively, while the slow phases of the transients from α (□) and β (△) showed no ATP-dependence. Published in similar form in Deacon, et al. (2012)[2].

The biphasic nature of these traces was anticipated for the slow isoform, β-S1, which was expected to be kinetically similar to the slow, bovine masseter S1, which has been shown previously to exhibit biphasic ATP binding in the presence of actin[132]. This was modeled to be due to the opening and closing of the nucleotide-binding pocket, limiting binding or dissociation to or from the pocket in the "closed" state[2, 132]. This biphasic nature was also observed for α-S1, indicating that α-S1 also undergoes a pocket opening/closing reaction during Step 1A.

Hyperbolic fits to the fast phase for α- and β-S1 were augmented by fits to the low-ATP linear phase using Equation 7: $k_{obs} = K_{1A}k_{+2A}$ (at low ATP concentrations). These fits yielded the calculated constants $K_{1A}k_{+2A}$, $1/K_{1A}$, and k_{+2A}, as described in detail in Chapter II. α-S1 was found to be moderately faster than β-S1 in terms of the apparent second order rate constant, $K_{1A}k_{+2A} = 2.5\pm0.3$ $\mu M^{-1}s^{-1}$ for α-S1 and 1.1 ± 0.1 $\mu M^{-1}s^{-1}$ for β-S1. The hyperbolic fits yielded very similar $k_{max} = k_{+2A}$ values, of 1500 ± 167 s^{-1} for α-S1 and 1445 ± 150 s^{-1} for β-S1. The major contribution to the difference in their apparent second order rate constants was therefore the

dissociation constant of actin-S1 for ATP, $1/K_{1A}$ = 626±143 μM for α-S1 and 1140±65 μM for β-S1 (Figure 36, Table 5).

ADP inhibition of ATP-induced dissociation of actin-S1 (Step 5A)

In order to investigate the ADP-binding characteristics of α- and β-S1, we wanted to determine the affinity of the actin-S1 complex for ADP and the rate of ADP-dissociation from actin-S1 in Step 5A (Figure 37). To observe these characteristics in the presence of actin we again used pyrene-actin fluorescence to signal the ATP-induced dissociation of the actin-S1 complex, and added ADP to the reactions as a competitive inhibitor of ATP binding.

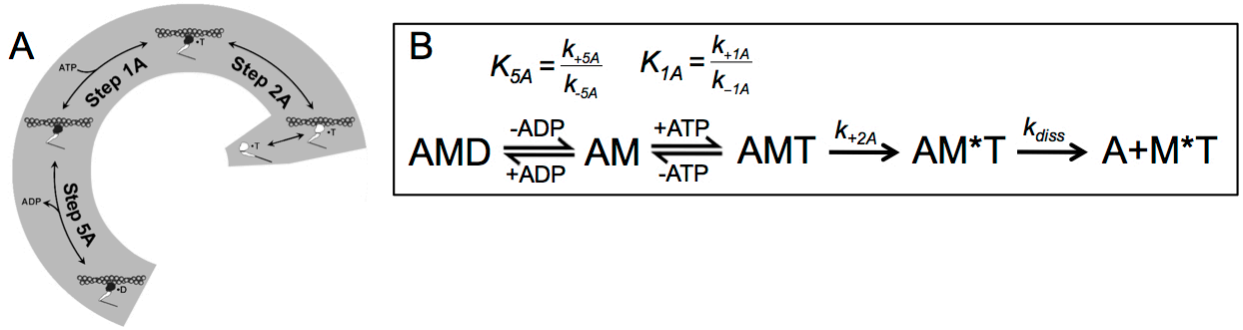

Figure 37: ADP inhibition of ATP-induced actin-S1 dissociation schemes. The participants in the reactions described are abbreviated as A = actin, M = myosin S1, D = ADP, and T = ATP. M* represents a different conformational state of myosin S1 with low actin affinity. ***A.*** The reaction steps following the mixing of ATP and ADP with AM include two possible paths, where AM mixed with ATP and ADP may progress through ATP-induced AM dissociation as described above, or may first bind ADP in the reverse reaction of Step 5A. ***B.*** Step 5A is governed by the dissociation constant K_{5A}, Step 1A is governed by the association constant K_{1A} and Step 2A is governed by the rate constant k_{+2A}.

Using the experimental setup for ATP-induced actin-S1 dissociation, ADP was added to the syringe containing ATP to act as a competitive inhibitor for binding actin-S1. With ATP at a fixed low concentration, well below the K_D of actin-S1 for ATP, ADP concentration was varied in sequential reaction mixtures in order to observe the reaction at well below the K_D of actin-S1 for ADP (K_{5A}), at saturating ADP concentration, and at sufficient points between the two in order to accurately model the inhibition. Fluorescence transients resulting from these mixing

events were biphasic, as they were for ATP-induced actin-S1 dissociation, and could be well described by non-linear regression analysis using the sum of two exponential functions, Equation 4. k_{obs} values from the fast phase of these fits were converted to k_{rel} values by dividing by k_0 and k_{rel} was plotted with respect to ADP concentration. These plots were fit using Equation 5: $\frac{k_{obs}}{k_0} = k_{rel} = \frac{1}{1+([ADP]/K_{5A})}$. For α- and β-S1, this set of reactions was performed on three independent preparations of protein. Figure 38A shows representative curves from single preparations of α- and β-S1. The fits to these data yielded the dissociation constant, K_{5A} = 152±25 μM for α-S1 and 21±3 μM for β-S1, revealing ~7-fold tighter binding of ADP in β-S1, compared to that of α-S1, when complexed with actin.

ADP dissociation from actin-S1 was measured by incubating pyrene-actin-S1 with saturating ADP and rapidly mixing with excess ATP. For β-S1, this yielded a Step 5-limited dissociation rate, $k_{obs} = k_{+5A} = 93\ s^{-1}$ (Figure 38C), at well below k_{+2A}. For α-S1, even after reducing reaction temperature to 12°C to extend the range of ATP concentrations able to be measured on the time scale of the stopped-flow to 16 mM, the saturating rate of ATP-induced actin-S1 dissociation in the presence and absence of ADP could not be discerned from one another (Figure 38B). This indicates that for α actin-S1 the ADP-dissociation reaction occurs very fast, with a rate constant greater than for the rate limiting constant of the ATP-induced actin-S1 dissociation reaction, k_{+2A}, and therefore cannot be measured using this reaction.

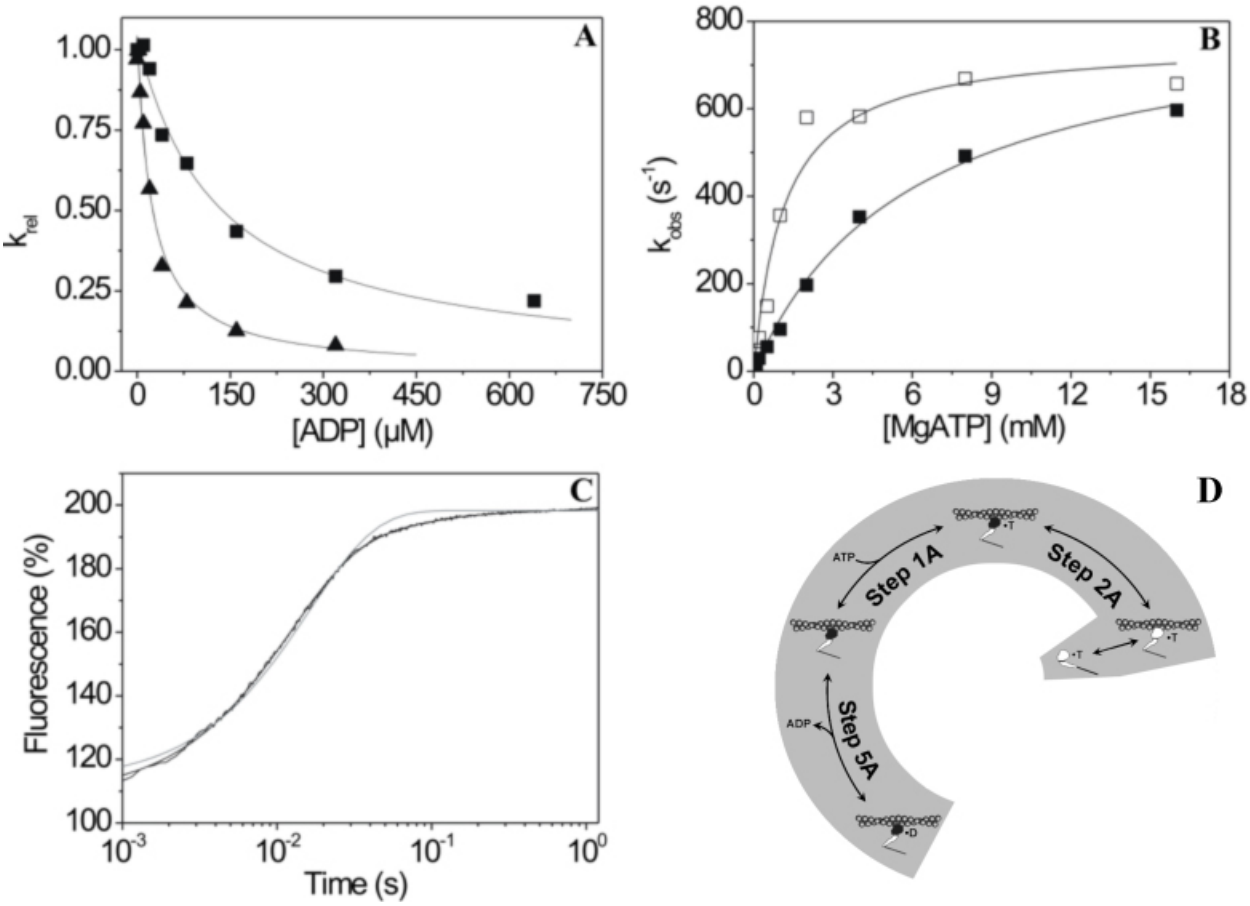

Figure 38: ADP binding to α- and β-MyHC actin-S1. ***A.*** 0.1 μM α (■) and β (▲) pyrene-actin-S1 was rapidly mixed with 25 μM (α) or 50 μM (β) ATP and a range of [ADP]. Single exponent fits to resulting transients were plotted as k_{rel} vs. ADP concentration and fit as described above. ***B.*** Plots of ATP-induced actin-S1 dissociation of α in the presence (■) and absence (□) of ADP at 12°C both saturate at ~800 s^{-1}, and thus ADP-dissociation occurs too fast for measurement in this manner for α. ***C.*** 0.5 μM pyrene-actin-β-S1 incubated with 100 μM ADP and mixed with excess ATP was best fit by a two exponential function (solid line) giving $k_{obs} = k_{+5A} = 84\ s^{-1}$. A single exponential fit (light grey line) is shown for comparison. ***D.*** Reactions involved in this set of experiments include Steps 5A, 1A, and 2A. Published in similar form in Deacon, et al. (2012)[2].

Actin binding of α- and β-S1 ($K_{D(Actin)}$ and $K_{D(ADP-Actin)}$)

In order to investigate the binding interaction between F-actin and S1, we wanted to determine the affinity of α- and β-S1 for F-actin, at the rigor state, prior to Steps 1 and 1A, and in the ADP-bound state, prior to Steps 5 and 5A (Figure 39). The dissociation constants governing the binding of F-actin by S1 and S1-ADP are referred to herein as, $K_{D(Actin)}$ and

$K_{D(ADP\text{-}Actin)}$.

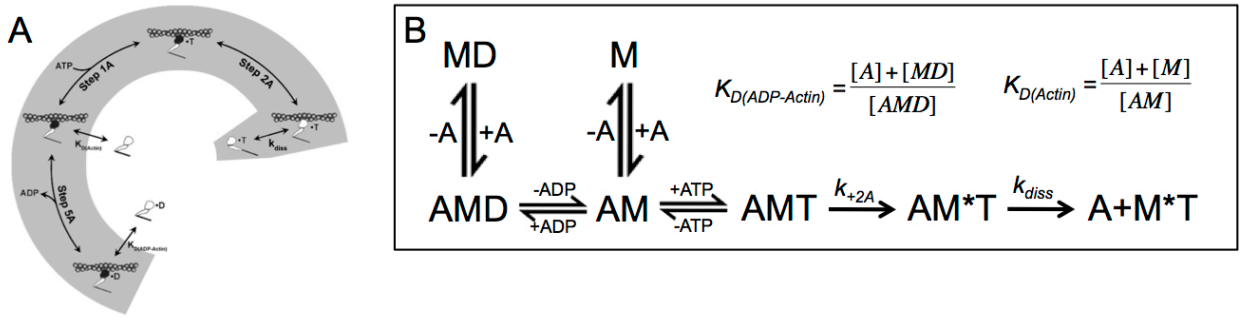

Figure 39: F-actin binding to S1 and S1-ADP schemes. The participants in the reactions described are abbreviated as A = actin, M = myosin S1, D = ADP and T = ATP. M* represents a different conformational state of myosin S1 with low actin affinity. ***A.*** Prior to Step 1A, AM is in equilibrium with A+M. Prior to Step 5A, AMD is in equilibrium with A+MD. ***B.*** The dissociation constants governing F-actin binding to M and MD are $K_{D(Actin)}$ and $K_{D(ADP\text{-}Actin)}$, respectively.

The signal amplitude of ATP-induced actin-S1 dissociation was performed and the concentration of S1 varied. In these reactions, the concentration of actin-S1 formed by pre-incubating a fixed pyrene-actin concentration with varied concentrations of α- or β-S1 was analyzed by following signal amplitude from the ATP-induced actin-S1 dissociation reaction. Since the concentration of actin-S1 complex formed by pre-incubating pyrene-actin with S1 was dependent upon the concentration of S1 and the dissociation constant, $K_{D(Actin)}$, the amplitude of the actin-S1 dissociation signal was in part defined by dissociation constant, $K_{D(Actin)}$.

Fluorescence transients resulting from these mixing events on the stopped-flow were biphasic for both α- and β-S1, as was anticipated for ATP-induced actin-S1 dissociation with these isoforms. As S1 concentration increased, the pyrene signal amplitudes resulting from the dissociation reaction visibly increased (Figure 40A). Averaged transients from 3 to 5 mixing events were fit using Equation 4, and the amplitudes from the fast phase of each reaction for β- and α-S1 were plotted with respect to S1 concentration. These plots were fit using the quadratic

function, Equation 8: $A = \frac{[S1] + K_D + [actin] - \sqrt{([S1] + K_D + [actin])^2 - \frac{4}{[S1][actin]}}}{2[actin]}$ (Figure 40B and 40C, respectively). The physiologically relevant root of the fitted functions yielded K_D values, which we attributed to the dissociation constant for actin binding, $K_{D(Actin)}$. β-S1 was found to bind F-actin ~4.5-fold more tightly than α-S1, as $K_{D(Actin)}$ = 37 nM and 8 nM for α- and β-S1, respectively (Table 5).

The same set of experiments was performed in the presence of saturating ADP in syringe 1, pre-incubated with actin-S1. The fits of signal amplitude with respect to S1 concentration in the presence of ADP yielded $K_{D(ADP\text{-}Actin)}$. β-S1-ADP was found to bind F-actin ~10-fold more tightly than α-S1-ADP, as $K_{D(ADP\text{-}Actin)}$ = 1.8 μM and 190 nM for α- and β-S1, respectively (Table 5, Figure 40). The ratio, $K_{D(ADP\text{-}Actin)} / K_{D(Actin)}$, was found to be ~2.5-fold larger for α-S1 than for β-S1, as $K_{D(ADP\text{-}Actin)} / K_{D(Actin)}$ = ~50 for α-S1 and ~20 for β-S1. The limitation of these measurements to low S1 concentration was due to the limits of the recombinant expression system, which is currently capable of producing S1 concentrations of up to ~5 μM.

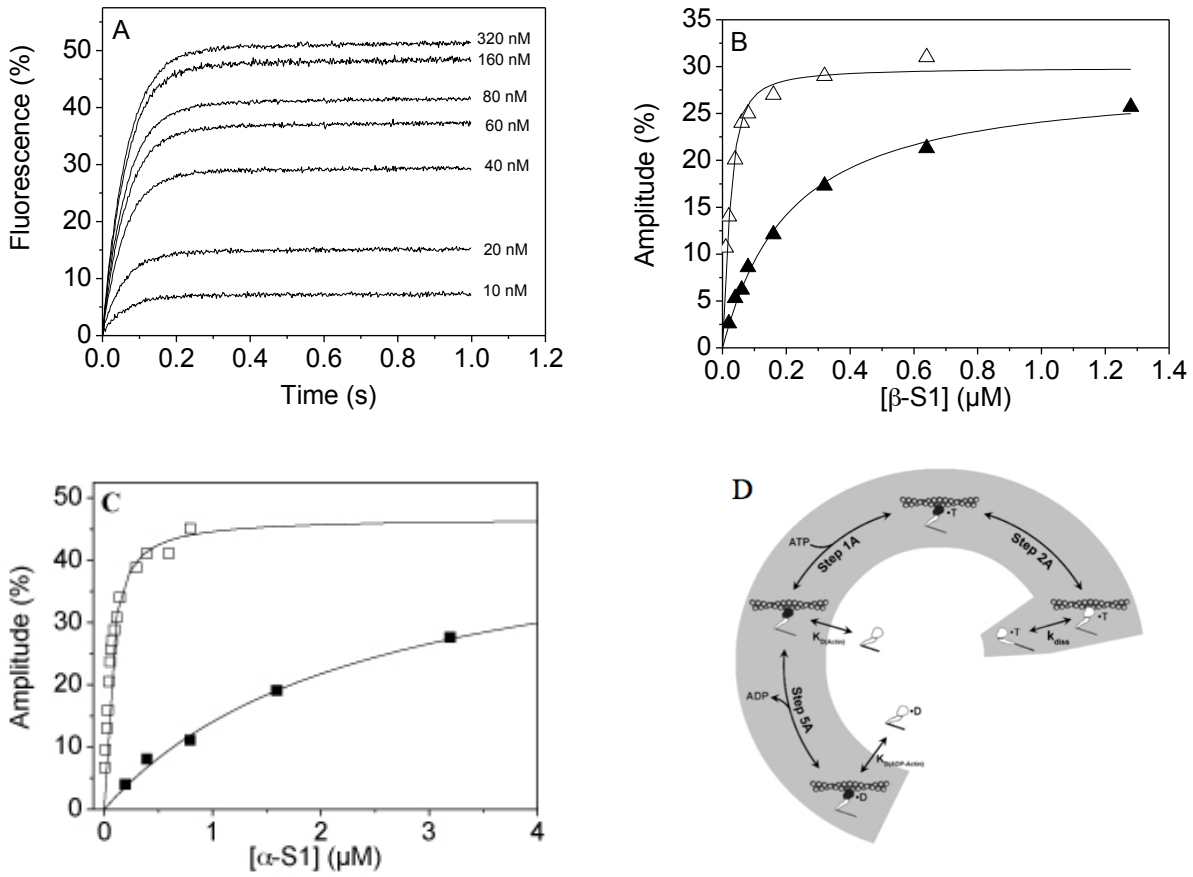

Figure 40: F-actin binding to α- and β-S1. ***A.*** Fluorescents transients measured upon the dissociation of 30 nM pyrene-actin and various β-S1 concentrations with 20 μM ATP steadily increased in signal amplitude proportional to S1 concentration. ***B.*** Amplitudes of the signal from *A* for β-S1 (△) and β-S1 in the presence of 500 μM ADP (▲), plotted with respect to S1 concentration and fit using the quadratic function, Equation 8. ***C.*** A plot of the amplitudes of the titrated dissociation signal for α-S1 (□) and α-S1 in the presence of ADP (■) shows a drastic affect on K_D in the presence ADP. ***D.*** The equilibrium constants studied herein govern transitions between states occurring prior to Steps 1A and 1, and prior to Steps 5A and 5. Published in similar form in Deacon, et al. (2012)[2].

Actin-independent ATP binding and hydrolysis (Steps 1-3)

In order to investigate the interaction of α- and β-S1 with ATP in the absence of actin we wanted to determine the affinity of α- and β-S1 for ATP, governed by the association constant, K_1, the rate constant governing Step 2, k_{+2}, and the rate constant for the ATP hydrolysis step, k_{+3} + k_{-3}, in Step 3 (Figure 41).

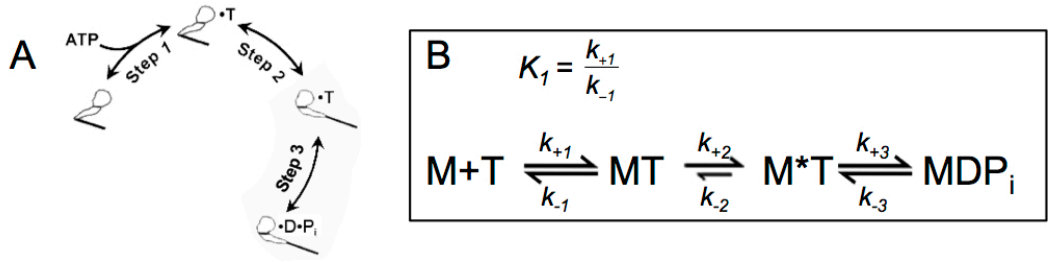

Figure 41: Actin-independent ATP binding and hydrolysis schemes. The participants in the reactions described are abbreviated as M = myosin S1, D = ADP, T = ATP, and P_i = inorganic phosphate. M* represents a different conformational state of myosin S1. ***A.*** The reaction steps following the mixing of ATP with myosin S1 are a rapid equilibrium step where ATP binds to S1 (Step 1), a conformational change (Step 2), and hydrolysis of ATP into ADP and P_i (Step 3). ***B.*** Step 1 is governed by the association constant K_1, Step 2 is governed by the rate constant k_{+2}, and in Step 3 the rate of ATP hydrolysis is defined by the sum, $k_{+3} + k_{-3}$.

These reactions occur in the absence of actin and we therefore used intrinsic protein fluorescence in S1 to observe ATP binding reactions, as described in detail in Chapter II. As described above, fluorescence signal changes are known to follow Steps 2 and 3 of the contractile cycle (Figure 41). These reactions were experimentally investigated on the stopped-flow by loading syringe 1 with S1 and syringe 2 with ATP, then rapidly mixing and observing tryptophan fluorescence. This experimental design includes Steps 1, 2 and 3, and fluorescence changes are expected to result from Steps 2 and 3. Reaction mixtures were repeated with ATP concentration varied in order to observe the reaction at well below the K_D for ATP ($1/K_1$), at saturating ATP concentrations and at sufficient points between the two in order to accurately model the substrate dependence of the reaction rate.

Fluorescence transients resulting from these mixing events were monophasic for α-S1 and biphasic for β-S1, and were therefore fit using Equation 2 and Equation 4, respectively. Figure 42A shows representative traces for α- and β-S1. k_{obs} values from these fits were plotted with respect to ATP concentration and the resulting curves for α-S1 and the fast phase for β-S1 were analyzed by fitting Equation 3A: $k_{obs} = \frac{k_{\max}[ATP]}{K_{1/2} + [ATP]}$. For each isoform, this set of

reactions was performed on three independent preparations of protein. Figure 42B shows representative curve from a single preparation of α- and β-S1.

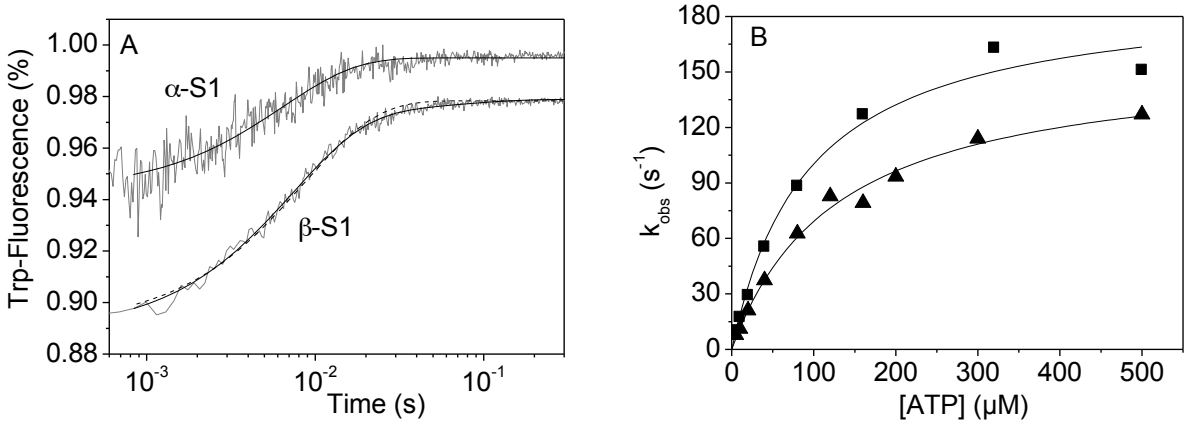

Figure 42: ATP binding to α- and β-S1. ***A.*** Fluorescence transients resulting from the rapid mixing of 0.2 μM α- and β-S1 with 500 μM ATP were monophasic for α-S1 and biphasic for β-S1. A single exponent fit of the β-S1 transient, using Equation 2, is shown for comparison (dotted line). ***B.*** Plots of k_{obs} for the fast phase with respect to ATP concentration for α (■) and β (▲) fit using Equation 3A. Published in similar form in Deacon, et al. (2012)[2].

The hyperbolic fits saturated at mean k_{max} values of 168 s^{-1} and 158 s^{-1}, for α- and β-S1, respectively. The mean of the slow phase for β-S1 was found to saturate at ~17 s^{-1} and was somewhat ATP-dependent. Given the multiple reaction steps modeled to contribute to the fluorescence signal in this experimental setup, determining which step produced each phase of the observed reactions required additional data. To assign the fast and slow phases to the appropriate reaction steps, quench-flow assays were performed. Quench-flow assays provided a separate measure of the rate of ATP-hydrolysis for comparison with α- and β-S1's fast and slow ATP binding reaction phases. S1 was rapidly mixed with excess ATP and incubated for timepoints of 10 to 500 ms before quenching. First, the long timepoint was used to determined the mean ADP production rate and total ADP signal amplitude of the burst phase, then three short timepoints were tested and a single exponential fit of the burst was used to provide a

preliminary k_{obs}. For β-S1, at 16, 33, and 68 ms timepoints ADP production was quantified as 16, 43, and 61% of the total burst amplitude, giving a k_{obs} = ~15 s^{-1}. By extrapolating K_1k_{+2} to the tested ATP concentration, β-S1's ADP production is roughly 1/3 of what would be expected for the fast phase (52.5 s^{-1}), while an extrapolation of the slow phase as the rate-limiting step of the scheme in Figure 41 predicts a k_{obs} of ~10.5 s^{-1}. The slow phase for β-S1 can therefore be attributed to ATP hydrolysis, k_{+3}+k_{-3}. For α-S1, a single short timepoint of 13 ms was sufficient to account for 33% of total burst amplitude and to assign the fast, single phase for α to the hydrolysis step. k_{+2} for α-S1 therefore must have a rate constant greater than that of the hydrolysis step. Therefore k_{+2} could only be quantified by this method as: $k_{+2} > 200$ s^{-1} (Table 5).

Actin-independent ADP binding (Step 5)

In order to investigate the interaction of α- and β-S1 with ADP in the absence of actin we wanted to determine the affinity of S1 for ADP, governed by the dissociation constant, K_5, and the rate constant governing ADP-dissociation from S1 in Step 5, k_{+5} (Figure 43).

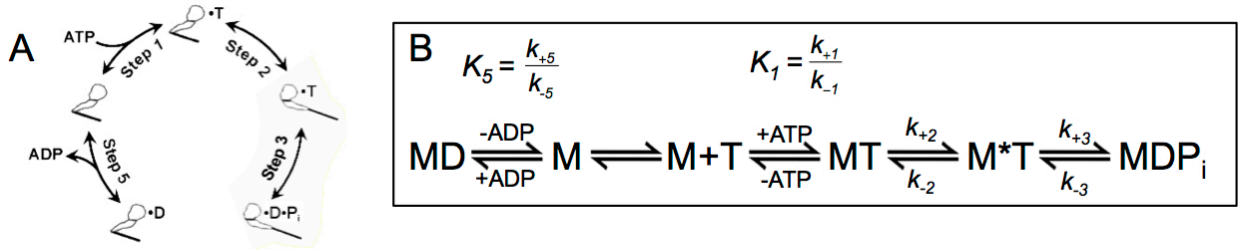

Figure 43: Actin-independent ADP binding and dissociation schemes. The participants in the reactions described are abbreviated as M = myosin S1, D = ADP, T = ATP, and P_i = inorganic phosphate. M* represents a different conformational state of myosin S1. ***A.*** The reaction steps following the mixing of ATP with S1-ADP are a slow ADP-dissociation step (Step 5), a rapid equilibrium step where ATP binds to S1 (Step 1), a conformational change (Step 2), and hydrolysis of ATP into ADP and P_i (Step 3). ***B.*** Step 5 is governed by the dissociation constant, K_5, and the rate constant k_{+5}, Step 1 is governed by the association constant K_1, Step 2 is governed by the rate constant k_{+2}, and in Step 3 the rate of ATP hydrolysis is defined by the sum, k_{+3} + k_{-3}.

Tryptophan fluorescence was again used to observe reactions in the absence of actin. As described in more detail in Chapter II, because the ADP-binding tryptophan signal was too small for measurement, reactions were designed to infer parameters associated with ADP binding from reactions observing ATP-binding tryptophan signals. Because ADP and ATP share the same binding site on S1, ADP can block ATP binding and thereby inhibit the appearance of the ATP binding tryptophan signal.

ADP binding parameters of the cardiac isoforms of S1 in the absence of actin were experimentally investigated on the stopped-flow by loading syringe 1 with pre-incubated S1 and ADP, and syringe 2 with ATP, then rapidly mixing and observing tryptophan fluorescence. This experimental setup is designed to produce two phases in the ATP-binding fluorescence transient, due to the two S1 populations in syringe 1. Syringe 1 contains both S1 and S1-ADP in complex before mixing with ATP from syringe 2. The ATP-binding signal occurs rapidly in the free S1 population and slower in the S1-ADP population due to the extra reaction step of ADP-dissociation. The signal amplitudes of these fast and slow phases reflect the respective concentrations of the two populations in syringe 1 before mixing. The relative concentrations of S1 and S1-ADP are governed by the dissociation constant K_5. As the ADP concentrations increase, the amplitude of the slow phase should increase and the amplitude of the fast phase should decrease, reflecting a shift in the two populations. By analyzing the amplitudes of the fast and slow phases with respect to ADP concentration, K_5 can be determined.

Reaction mixtures were repeated with the ADP concentration in syringe 1 varied in order to observe the reaction at well below the K_D of S1 for ADP (K_5), at saturating ADP concentrations and at sufficient points between the two in order to accurately model the substrate dependence of the amplitudes for each phase of the reaction. Fluorescence transients resulting

from these mixing events were biphasic and were fit using, Equation 4. Traces from one preparation of β-S1 protein are shown in Figure 44A to demonstrate the relative change in the signal amplitudes for the fast and slow phases as a result of changes in ADP concentration.

Relative amplitudes for the slow and fast phases were plotted with respect to pre-mixing ADP concentration and fit using Equations 6A: $A = \frac{A_{max}[ADP]}{K_5 + [ADP]} + A_{min}$ and 6B: $A = \frac{A_{max}K_5}{K_5 + [ADP]} + A_{min}$, respectively (Figure 43B). From these fits we calculated mean values for the ADP dissociation constant, K_5, of 2.8 μM and 0.5 μM for α and β, respectively (Figure 44B). At saturating ADP, where $k_{obs} = k_{+5}$, fits to averaged fluorescence transients yielded k_{+5} = 2.7 s^{-1} and 0.9 s^{-1}, for α- and β-S1, respectively (Table 5).

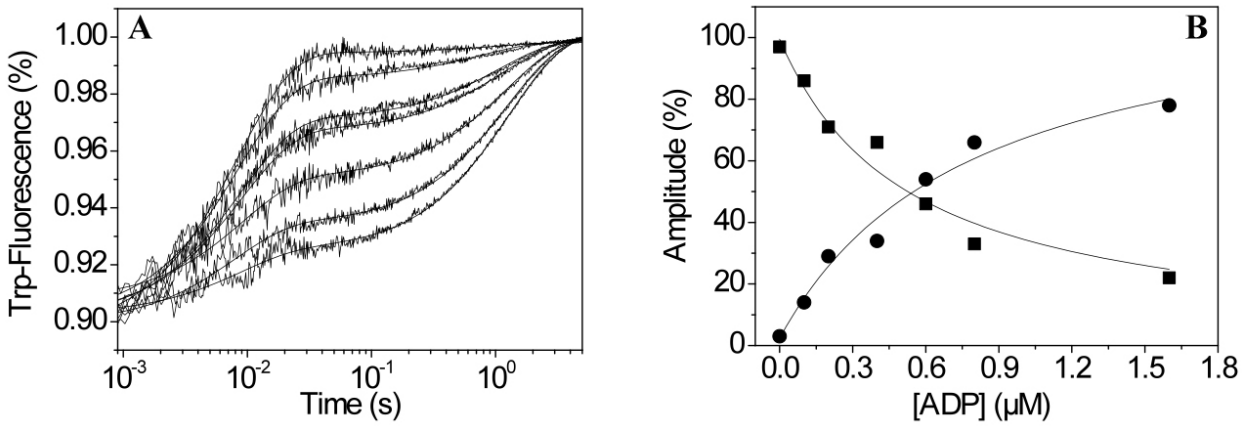

Figure 44: ADP binding to α- and β-S1. ***A.*** Fluorescence transients observed upon mixing 0.2 μM β-S1 and varied ADP (0 to 1.6 μM) with 100 μM ATP are fit using the double exponential function, Equation 4. ***B.*** The amplitudes for the slow and fast phases observed in *A* were plotted with respect to pre-mixing ADP concentration and fit using Equations 6A and 6B, respectively, to yield K_5 = 0.53 μM. Published in similar form in Deacon, et al. (2012)[2].

Stopped-flow kinetics of β-sS1

Each of these measurements was performed in a similar manner with β-sS1. For all kinetic constants measured, the values were within 2-fold of those reported for β-S1. The

influence of the shortened lever arm, the lack of the RLC and the known and physiologically appropriate isoform identity of the ELC were found to have no significant impact the kinetics of β-MyHC. These data are reported in Table 5, where they are compared to fast S1 purified from rabbit skeletal muscle and slow S1 purified from bovine masseter, from previous studies performed in the Geeves lab.

Duty ratio and cycle duration of α- and β-S1

Duty ratio is defined as the fraction of total ATPase cycle time a myosin spends cross-bridged to F-actin. Duty ratios were modeled by taking the inverse of the rate constants contributing to each phase of the cycle (crossbridged versus detached) extrapolated to physiological 5 mM ATP. The lifetimes of each phase of the ATPase cycle were calculated by: Crossbridge lifetime = $1/k_{+5A} + 1/(K_{1A}k_{+2A}[ATP]/(1+K_{1A}[ATP]))$ and Detached lifetime = $1/(k_{+3}+k_{-3})$, for a cycle at 20° C, as these constants were measured at that temperature and cannot simply be extrapolated to 37° C. In the same manner it is possible to predict the total cycle time for these motors by the sum of these two lifetimes. For β-S1 the cycle time of 79.9 ms is spent 16% (±2.7%) bound to F-actin, and for α-S1 the much shorter cycle time of 6.7 ms is spent only 10% (±3.1%) bound to F-actin.

	Human cardiac α-S1	Human cardiac β-S1	Human cardiac β-sS1	Rabbit skeletal S1[a]	Bovine masseter β-S1[b]
ATP binding to S1					
K_1k_{+2} ($\mu M^{-1}s^{-1}$)	2.2±0.1	1.5±0.3	1.5±0.1	1.9	0.97
k_{+2} (s^{-1})	>200	158±18	160±23	>1000	117
$k_{+3}+k_{-3}$ (s^{-1})	168±28	17±2	14	131	18
ADP binding to S1					
K_5 (μM)	2.8±0.7	0.5±0.1	1.0±0.1	2	2.0
k_{+5} (s^{-1})	2.7±0.6	0.9±0.1	0.59±0.08	1.4	1.0
ATP binding to actin·S1					
$K_{1A}k_{+2A}$ ($\mu M^{-1}s^{-1}$)	2.5±0.3	1.1±0.1	1.6±0.3	2.4	1.24
$1/K_{1A}$ (μM)	626±143	1140±65	710±65	520	984
k_{+2A} (s^{-1})	1500±167	1445±150	1081±50	1250	1220
$K_{\alpha 1A}$	10±2	8±2	12±2	*	7.7
$k_{+\alpha 1A}$ (s^{-1})	78±30	56±12	49±5	*	56
ADP binding to actin·S1					
K_{5A} (μM)	152±25	21±3	10±3	120	9.6
k_{+5A} (s^{-1})	>1252	93±5	64±3	>1200	94
$K_{\alpha 5A}$	*	7±1	3.7±0.4	*	5.3
$k_{+\alpha 5A}$ (s^{-1})	*	15±0.6	1.8±0.1	*	9.6
S1 binding to F-actin					
$K_{D(Actin)}$ (nM)	37±11	8±2	17±7	33	7.0
$K_{D(ADP\text{-}Actin)}$ (nM)	1844±546	191±17	229±138	1000	37

Table 5: Stopped-flow kinetics of α- and β-S1. Recombinant α- and β-S1 and β-sS1 proteins were observed interacting with ATP, ADP, and pyrene-actin. The mean values for the calculated kinetic constants governing these interactions are given, and the variance reported as standard error of the mean. These data represent 2 to 3 biological replicates each. For comparison, animal muscle derived fast, rabbit skeletal S1 and slow, bovine masseter S1 are listed from previous studies in the Geeves lab. Published in similar form in Deacon, et al. (2012)[2]. [a]Assembled from Ritchie et al. (1993)[184], Millar & Geeves (1988)[180] and Nyitrai et al. (2006)[181]. [b]From Bloemink et al. (2007)[132]. *No detectable slow component.

Kinetic effects of the hypertrophic cardiomyopathy mutation R453C in β-sS1

The R453C mutation was introduced into the sS1 construct of human β and copurified with MYL3 as described above; all kinetic comparisons were made with respect to β-sS1. The protein bearing the R453C mutation was produced and isolated as described above and purified with its coexpressed ELC, MYL3, which appeared at the expected molecular weight, ~25 kDa, by SDS-PAGE (Figure 45).

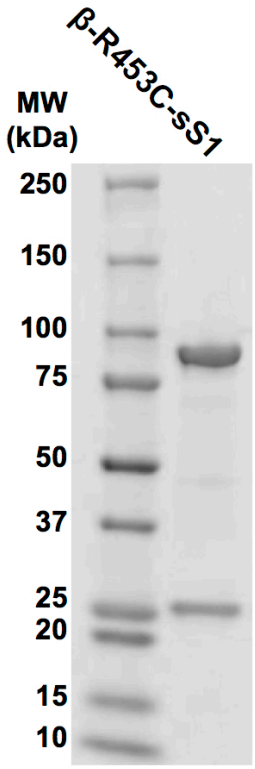

Figure 45: Purified recombinant β-R453C-sS1 protein. SDS-PAGE of purified recombinant β-R453C-sS1 appears similar to β-sS1 (Figure 29, lane 4) in the apparent molecular weights of myosin heavy chain and myosin light chain bands (~93 kDa and ~25 kDa, respectively. The sS1 construct of β-R453C-sS1 copurifies with the human recombinant ventricular ELC, MYL3.

Unexpectedly for a mutation associated with multiple functional domains in S1, The R453C mutation in β-sS1 did not produce broad kinetic alterations in the motor. ATP-induced actin-sS1 dissociation, ADP binding to actin-sS1, and actin-independent ATP binding to sS1 were each tested and all constants were determined to be within 1.5-fold of the wild-type, with the exception of the slow phase of ATP binding to sS1. This slow phase, attributed in β-sS1 to the ATP hydrolysis step (Step 3) was measured to be ~10-fold slower as a result of the R453C mutation, $k_{+3}+k_{-3}$ = 14 s^{-1} for β-sS1 and 1.5 s^{-1} for β-R453C-sS1. While all other kinetics of the cycle remain unchanged, this feature on which the lifetime of the detached state depends should therefore produce a significant change in both cycle time and duty ratio, which in the predominant motor of the cardiac sarcomere may impact the number of actin-myosin cross-bridges present at any given moment in a contracting cardiac fiber.

Interference from the eGFP-tag

The presence of the eGFP-tag on the fast skeletal myosin constructs necessitated the use of the Kodak 47B filter for fluorescence measurements on the stopped-flow. This removed nearly half of the total fluorescent signal from these reactions, which therefore required higher quantities of protein (Figure 46). Comparative analysis of kinetics measured from β-S1 constructs with and without this eGFP-tag identified a single significant difference in the eGFP-bearing construct. The kinetic constants for ATP binding to S1 and actin-S1, actin-S1 dissociation, actin binding, ADP-dissociation from S1 and actin-S1, and ADP binding to actin-S1 were all similar to within 20% between the constructs. The eGFP-bearing construct diverged from the eGFP-free construct in ADP binding to S1 in the absence of actin, where the presence of the eGFP-tag produced a ~10-fold decrease in ADP affinity, though with no concomitant change in the rate constant for ADP-dissociation. Given the limitations of the filtered signal for these fast skeletal studies it was possible to measure ATP and ADP binding in both the presence and absence of actin, but not to measure actin binding or detect ATP hydrolysis. Figure 46 shows the overlays of ATP-induced actin-S1 dissociation reactions performed using the same concentrations of eGFP-bearing and eGFP-free constructs.

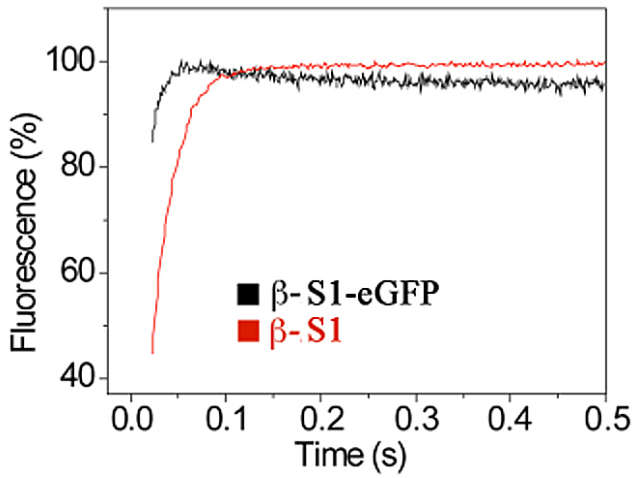

Figure 46: Effect of the eGFP-tag on stopped-flow measurements. Using the same concentration of S1, nearly 4-fold greater fluorescence amplitudes were obtained from S1 lacking the eGFP-tag, as well as improved signal over noise. The presence of an additional apparent reaction with a consistent rate of -0.5 s^{-1} was present in all pyrene-actin measurements of eGFP-bearing S1 proteins.

DISCUSSION

Human β-myosin is kinetically similar to bovine muscle derived slow, type I myosin

As shown in Table 5, the kinetic properties of recombinant human β-S1 and β-sS1 appear very similar to S1 proteins purified from slow, type-I-rich muscles, which are known to contain predominantly the β-MyHC isoform[202], as nearly all constants among the β-myosin constructs agreed to within ~2-fold. This suggests that the recombinant S1 and sS1 protein constructs we designed are sufficiently accurate models for studying myosin kinetics. This also suggests that the kinetic properties of myosin, such as β-myosin, are highly conserved.

Biphasic detachment step

The ATP-induced actin-myosin detachment of α- and β-S1 occurred in two distinct phases: a fast, ATP-dependent phase and a slow, ATP-independent phase. This feature has been seen previously in slow-fiber myosin purified from bovine masseter muscle, where it was attributed to the motion of a region of S1 with the capability to block diffusion of nucleotide in and out of the binding pocket, effectively opening and closing the pocket and was referred to in that previous work by the equilibrium constant $K\alpha$ and the rate constant $k_{+}\alpha$[132]. These states are not observed in kinetic measurements of the fast isoforms or the developmental isoforms, though the highly conserved nature of myosins would imply that the structures responsible for this event exist in those isoforms as well. Our hypothesis to explain this divergence is that in the fast and developmental isoforms where this reaction is not observed, the "closed" state which would limit the dissociation reaction does occur in these myosins but very infrequently and/or for very short durations. This reaction would therefore be present in such a small fraction of the population of S1 proteins in a stopped-flow reaction mixture that its signal would carry an amplitude small enough to be lost in the noise of the dissociation reaction. In this way, α- and β-myosins both

share a common feature with slow myosins in that they exhibit biphasic ATP binding kinetics in the presence of actin.

Crossbridge detachment is governed by different reactions in human α- and β-myosins

Crossbridge detachment is an influential step in muscle contraction. The rate of crossbridge detachment in a muscle fiber's myosin isoforms is thought to determine its maximum shortening velocity[181]. In striated muscle MyHC isoforms, the rate of the detachment step can be limited by the either the rate of ADP-dissociation (Step 5A) or the steps of ATP-induced actin-MyHC dissociation (Steps 1A and 2A)[181, 186, 187]. Human β-S1, like slow myosins purified from muscle, has a very slow detachment step characterized by tight ADP binding (the tightest measured in this study for wild-type motors), ADP dissociation sufficiently slow to limit the rate of detachment, and weak ATP binding (the lowest affinity measured in this study, with the exception of IIb). This produces an elongated crossbridge lifetime and a higher duty ratio, both features of the slow moving, tension maintaining class of myosins[46]. α-S1, although most similar in amino acid sequence to the slow β isoform, does not share this trait. α-S1, like fast myosins purified from muscle, has a very fast detachment step, characterized instead by weak ADP binding, very fast ADP-dissociation, and tight ATP binding. In each facet of crossbridge detachment, the human α isoform appears to be like the fast skeletal isoforms as a lower duty ratio, fast moving motor type[46].

α-S1 exits the detached state ~10-fold faster than β-S1

While the steps leading to crossbridge detachment determine the lifetime of the crossbridged state, the detached lifetime is defined by the rate of ATP hydrolysis. The rate constant for the ATP hydrolysis step, $k_{+3}+k_{-3}$, for β-S1 again agrees closely with slow muscle myosins, at 17 s^{-1}. This predicts a long dwell time in the detached state, which in combination

with its slow detachment describes the theoretical contractile cycle of human β-myosin at 20° C as long (~80 ms) with a moderately high duty ratio (for a sarcomeric myosin) of 16% (±2.7%). Human α-S1, by contrast has a ~10-fold higher rate constant for the hydrolysis step. This predicts a short dwell time in the detached state, which in combination with its rapid crossbridge dissociation kinetics predicts its theoretical cycle to be very short in comparison (6.7 ms), with a lower duty ratio of 10% (±3.1%).

Human α- and β-myosins are kinetically dissimilar

The natural hypothesis arising from high protein sequence identity between α- and β-myosins, in conjunction with the only modest steady-state functional differences, is that in general kinetic character α-myosin is likely to behave like β-myosin, though somewhat faster. Surprisingly, while human β-S1 closely resembles the previously measured slow, bovine masseter muscle S1 in nearly all kinetic parameters, α-S1 in nearly all kinetic parameters resembles a fast skeletal muscle myosin. In spite of >90% identity with the slow β-MyHC and as low as ~80% identity with the fast skeletal isoforms, α-MyHC can be best categorized as, kinetically, a fast skeletal type myosin (Figure 47). The only manner in which α differs from the fast skeletal mode and appears more like β is in its biphasic ATP-induced actin-S1 dissociation, indicating the presence of a slow nucleotide pocket opening/closing step. This step is never seen in fast skeletal myosins. It is unclear if this trait has any significance in physiological contractile activity.

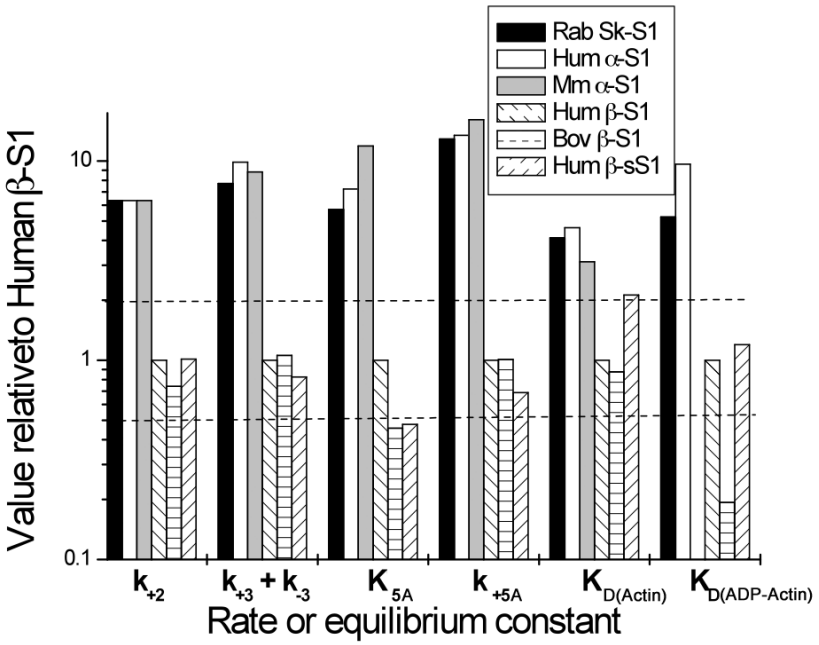

Figure 47: Relation of human α- and β-S1 kinetics to known fast and slow myosins. Rate and equilibrium constants measured for mouse, rabbit, and cow myosins are compared to human α- and β-S1 from this study. Constants are normalized to the values for human β-S1. β-S1 constants group closely with the slow muscle derived bovine masseter S1[132]. α-S1 constants differ from β-S1 constants and group instead with rabbit fast skeletal muscle[180, 184] and mouse cardiac muscle S1[2]. Published in similar form in Deacon, et al. (2012)[2].

Implications of α- and β-MyHC kinetics in cardiac muscle fibers

α- and β-myosins are predicted by this study to preform distinct and different roles in muscle contraction. α-MyHC is predicted to act as a "fast" myosin and β-MyHC as a "slow" myosin. These "slow" and "fast" roles may be very important to proper contractile function in the human heart, since the loss of the fast α isoform from the heart in disease is correlated with decreased cardiac function[167]. These roles may be described as: a "slow" myosin acts to efficiently but slowly generate force and maintain tension, while a "fast" myosin has the capacity to rapidly generate force, but is unable to maintain tension on its own. α- and β-myosins would therefore complement each other in a scenario such as the human heart where large forces are required to achieve contraction, and where a constant demand exists to generate force and

rapidly cycle, contracting again and again, continuously. While β-MyHC is capable of sustaining large forces, it is very slow and may not be capable of maintaining the pace of a constantly rapidly contracting heart on its own. However, while α-MyHC has the capacity to contract very quickly and cycle very rapidly, this feature comes without the ability on its own to hold the tension which may be necessary for proper contraction in a large human heart. One reason to think this may be the case is by a comparison to rodent hearts. Rat hearts are far smaller and beat far more rapidly than human hearts. This requires less maintenance of tension but faster turnover. In the rat heart α-myosin is the predominant isoform in an approximately 9 to 1 ratio with respect to β-myosin, the approximate inverse of the human heart's myosin composition[203].

ELC identity and the presence or absence of the RLC do not effect β-MyHC kinetics

The "short-S1" protein, β-sS1, differs from β-S1 in two ways: it lacks the RLC binding region and thus lacks the RLC, and it is bound by a single isoform of ELC of the appropriate identity for its human cardiac muscle environment, MYL3. These differences were predicted to have some impact on the kinetics of the motor, however, no kinetic constant was seen to differ more than 2-fold. Since each of these parameters was essentially similar between S1 and sS1 constructs of β, we conclude that the features of myosin kinetics studied herein are not strongly influenced by the identity of the ELC. Examining the impact of a loss of RLC may however require weight bearing contraction conditions, since previous studies indicate the influence of RLC may only be apparent under loaded conditions[204]. Similarly, the role of the ELC may only be apparent under steady-state ATPase conditions. Ongoing collaborative studies aim to address the roles of the light chains by testing additional isoforms of human ELC, as well as by testing single-molecule kinetics under load-bearing conditions.

The R453C mutation in β-MyHC extends the detached lifetime and lowers the duty ratio

The HCM mutant, β-R453C-sS1, has a single major change in its kinetic properties with respect to the wild-type, β-sS1. The R453C mutation apparently decreases the rate constant for ATP hydrolysis ~10-fold. This is predicted to alter both the duration of the overall cycle and the duty ratio. The duration of the cycle is predicted to increase from ~80 ms to >600 ms as a result of the R453C mutation with a duty ratio reduced to ~2%. Hypothetically, in a human HCM patient, with a heart composed of 90% β-MyHC, where approximately half of the β-MyHC bears the R453C mutation, ~45% of the myosin in the heart would be affected by the mutation. If our predicted cycle time for β-R453C is correct, relative to wild-type β-MyHC, then the effected 45% of total myosin may be participating in only 13% of the crossbridge events of a healthy β-myosin. Since the role of the slow β isoform in muscle contraction is predicted to be as an efficient tension maintaining motor[46], this loss of tension maintaining crossbridges may be sufficient to disrupt contractile function. While the coordinated nature of the sarcomere allows it to contract with only a fraction of the ~300 myosins per thick filament crossbridged to actin at a given moment, such a major alteration to a large fraction of its motors can be anticipated to produce notable effects. Ongoing collaborative studies aim to investigate such possible effects *in vivo*.

eGFP signal difficulties

The presence of the eGFP-tag was found to produce a ~10-fold decrease in ADP affinity. There is no known biochemical basis for such an effect as a result of eGFP. One hypothesis is that the eGFP was capable of coming in contact with the nucleotide binding site due to flexibility in the carboxy terminus of S1, but the absence of effects on other nucleotide binding reactions makes this far less likely. It is far more likely that eGFP fluorescence interfered with the

reaction signal. The reaction affected consistently produced the lowest signal to noise ratio of those tested, and therefore any influence of eGFP fluorescence on the fluorescence transients would be more significant to such data. This effect could have led to the observed differences. For this reason, however, it is not possible to compare this feature of the kinetics of constructs bearing the eGFP-tag with those of constructs lacking it. For all future kinetics studies on the stopped-flow, constructs lacking a fluorescent tag will be constructed to avoid this difficulty.

CONCLUSIONS

The first kinetic study of pure populations of human myosin isoforms

The development of a system for producing recombinant striated muscle myosin motors has expanded the type and scope of the experiments that are accessible to the striated muscle myosin field. Without the limitations on isoform type and purity imposed by isolating myosin from animal muscles, and without the limitations on quantity and cost from genetically modified systems or from human patients and volunteers, additional studies in many aspects of human myosin biology are now possible.

This study represents the first detailed kinetic measurements of pure populations of single human myosin isoforms and the first such study in any species of the specialized extraocular isoform, of the individual developmental isoforms embryonic and perinatal, and of the cardiac isoform α-MyHC. The study of the kinetics of single myosin isoforms reveals distinct roles for individual isoforms in muscle contraction. The general categories "slow" and "fast" have been used to describe the kinetic categories of these myosin isoforms, but as the data show, there is additional variation within those descriptors. The terms "slow" and "fast" as descriptors of isoform contractile style are expanded upon in Bloemink and Geeves, 2011[46]. The modes of slow and fast myosins, described therein, follow closely with our characterizations of the recombinant human myosins. For example, slow myosins are characterized by slow contraction with the capacity for efficiently maintaining tension (i.e. without requiring rapid fiber twitching and high ATPase cycling rate). This involves both slow entry into the actin-myosin crossbridge, defined by slow ATP hydrolysis (low value for k_{+3}+k_{-3}), and slow exit from the crossbridge, defined by a slow ADP-dissociation step (low value for k_{+5A}). This latter aspect, a slow ADP-dissociation step, which limits the rate of crossbridge detachment, is a key manner by which

slow myosins maintain the force of contraction in a sarcomere, by extending the lifetime of the actin-myosin crossbridge. By contrast, the "fast" isoforms have several-fold faster ATP hydrolysis and very rapid ADP dissociation, such that it does not limit crossbridge detachment. When fast and slow myosins are mixed together in a contractile unit their features may be synergistic in the coordinated system of the sarcomere, for the efficient production of contractile power, as suggested by studies varying the relative compositions of α- and β-myosins in rat and rabbit hearts[169, 170, 205]. In a simplified model of this synergistic activity, the fast α-myosin functions as a rapid initiator of force generation, and the concurrent activity of slow β-myosin holds the tension produced by the fast activity of α-myosin without the need for high twitch frequency, as is required in fibers containing only fast isoforms[121].

Correlation of steady-state ATPase with pre-steady-state kinetics

ATPase k_{cat} values separated into two groups, "fast" and "slow." β-myosin was the only slow motor tested, ranging from 2- to 5-fold slower than the other human isoforms. k_{cat} correlates well with both the ADP-dissociation step (Step 5A) and the ATP hydrolysis step (Step 3), both of which were found to be significantly slower in β-myosin than in the other isoforms tested. However, since the rate-limiting step in F-actin-activated ATPase has been identified as occurring in the detached state, this points to Step 3 governing k_{cat} for the F-actin-activated ATPase reaction, though this cannot be substantiated by these data since the ATP hydrolysis step was not determined for the fast skeletal isoforms in this study. K_{ATPase} values did not apparently correlate to any specific pre-steady-state constant. Due to the differing ionic strength and temperature of the steady-state and pre-steady-state assay conditions, the kinetic property governing K_{ATPase} in the steady-state assay may function differently in the pre-steady-state assays.

Disease-causing mutations in human myosins

Studies of disease-causing mutations in mouse revealed that it was very important to study disease-causing mutations in the appropriate MyHC isoform. The HCM-causing R403Q mutation in human β-myosin produced contradictory results when put into the mouse α- and β-myosin genes[97]. This emphasizes the importance of studying myosins and their mutations in their physiologically appropriate backgrounds. Overall, the close agreement of the kinetics of the recombinant myosin subfragments described in this thesis with the established kinetics for fast and slow myosin subfragments prepared from muscle, as shown in Tables 3, 4 and 5, supports the notion that these recombinant motors accurately represent their respective counterparts in human muscle. This system also allows for the relatively simple and inexpensive production of modified or mutated myosin subfragments (when compared with the cost of genetically modified animals). This system is therefore highly suitable for the study of human disease-associated mutations.

The effects observed in the two disease-associated mutations tested herein both appear to be biologically significant. The HCM-causing mutation R453C in human β-sS1 produced a ~10-fold decrease in the rate constant determining the lifetime of the detached state, predicting an 8-fold decrease in duty ratio, from 16% to 2%, and an 8-fold elongation of the predicted duration of each cycle. If these alterations hold true in the physiological context of the cardiac muscle fiber, then this mutation in one allele of β-MyHC would be predicted to cause up to a 40% decrease in the number of load-bearing crossbridge events formed in the sarcomere. While these *in vitro* kinetic data do not indicate a pathway of hypertrophy they do describe a major alteration in sarcomeric activity that could have consequences in the heart.

The FSS-causing mutation R672H in human embryonic-S1 produced multiple alterations to crossbridge detachment steps. The major factor in its disruption of embryonic myosin activity, however, is predicted to be its alteration to ADP affinity and ADP dissociation kinetics. As described above, the major difference between "slow" and "fast" myosins is the presence or absence, respectively, of a slow ADP-dissociation step governing the lifetime of the crossbridged state. In embryonic-S1, this mutation alters its contractile activity from "fast" to *very* "slow." The contractile characteristics of Emb-WT indicated that it may be faster in terms of detachment kinetics than the fast skeletal isoforms IIa, IId, and IIb by ATP binding reactions. In Emb-R672H, the ADP-dissociation rate constant, k_{+5A}, becomes altered to ~10-fold lower than that of the slow β isoform. This ADP-binding alteration, resulting from the R672H mutation, may be expected to have significant consequences in developing muscles. According to previous studies, the myosin content of neonatal mouse muscle consists of primarily embryonic and perinatal isoforms, with ~10% β-MyHC. If perinatal is similar to embryonic in being a fast isoform, as its ATPase k_{cat} would indicate, then it is likely that these neonatal muscles would have a 9 to 1 ratio of fast to slow myosins. At birth, the embryonic isoform composes ~25% of the total myosin and before birth this is thought to be much higher[154, 155, 206]. Therefore, this mutation in one allele of embryonic-MyHC can be predicted to cause the balance of fast to slow myosins in developing muscles to shift to nearly 4 to 1. It is unsurprising, therefore, that the phenotype associated with this mutation involves multiple contractures, as these predictions would drastically increase the tension maintaining properties of the muscle. However, these *in vitro* measurements are not themselves sufficient to extrapolate to effects *in vivo*.

The limitations of *in vitro* assays such as these include the absence of regulation on F-actin binding and the absence of load, which could each play a large role in the impact of

disease-causing mutations in myosins. However, upcoming collaborative studies aim to address these points in the near future.

Methods Enhancements

The development of the recombinant expression system and the enhancement of the F-actin-activated ATPase assay method with stirring methods by Daniel R. Resnicow in the Leinwand lab represent large advancements in the methods used in the study of myosin preceding my involvement in this project. Since that time the project aims have continued to advance. During my graduate work we performed the first pre-steady-state kinetic measurements on active recombinant striated muscle myosins. Initially using the eGFP-fusion S1 constructs produced for previous steady-state studies, these measurements were complicated by the interference of the eGFP tag. While it was not at first apparent that the origin of the steady -0.5 s^{-1} signal was a result of eGFP fluorescence, the elimination of that signal upon the first use of the Kodak 47B filter satisfied us with this conclusion. This motivated the production of myosin subfragments lacking the fluorescent tag. The first experiments with β-S1 lacking the eGFP tag produced a ~4-fold increase in signal amplitude from pyrene fluorescence measurements, with additional improvement in signal to noise using the same sample concentrations. By this modification, the data we were able to generate per unit of protein produced was increased several-fold. This is of particular significance because the method of protein production is intensive.

For that reason, advancements in protein production are also of great significance to this field of study. Advancements have been made in tissue culture materials efficiency, myotube infection efficiency, recombinant adenovirus production efficiency, purification efficiency, and in protein storage. Briefly, this includes the main findings that: 1) C_2C_{12} cultures used for

producing protein can be cultured in 10% FBS rather than 20% FBS with no loss in cell health or protein yield. 2) Infecting myotubes with small quantities of recombinant adenovirus is possible by applying the virus to cells in proportionately smaller volumes of media for up to 1 hour, with no loss in cell health or protein yield. 3) During purification of S1 proteins, dialysis into low salt buffer following nickel-affinity chromatography at high protein concentrations can cause precipitation of S1 protein and therefore significant loss of materials. This precipitation can be decreased to large extent by performing the dialysis as a gradient from start condition to target condition overnight. 4) Due to the long timescale and large quantities of cell material involved in the protein production process in culture, coordination between production and experimental protein demand is a significant concern. By establishing a method for safely freezing cell pellets, while retaining myosin activity, it has been possible to eliminate protein production timing concerns to a large extent and to accumulate sufficient quantities of protein-bearing cells for crystallographic studies.

Future directions

This work using recombinant sources of human myosin heavy chain proteins has established that studies of individual myosin isoforms using pre-steady-state techniques are capable of revealing new activities and distinctions between and among the isoforms. This work has also established the feasibility of investigating kinetic alterations resulting from disease causing mutations in human myosins. To continue these studies, several additional research aims should be undertaken. The fast skeletal isoforms, IIa, IId, IIb, and extraocular, should be further analyzed to determine the rate constant governing ATP hydrolysis, $k_{+3} + k_{-3}$, and thereby assign their ATP binding reaction phases. This would complete our kinetic analysis of the fast skeletal isoforms and allow the prediction of cycle times and duty ratios to properly place these

isoforms into their respective kinetic categories. This work is currently underway and simply awaits sufficient protein quantities to undertake the task. Also, the current short list of disease causing mutations under study should be expanded to include multiple mutations leading to the same disease, multiple mutations in both fast and slow myosins, and similar mutations which lead to different diseases. These aims are also underway through a collaboration with multiple research groups, taking a multidisciplined approach to the study of myosins and mutations causing human cardiac and skeletal diseases. It is also of interest to study myosin by multiple methods of analysis. The multidisciplined approach taken by this collaborative team aims to complement this *in vitro* work with single molecule biophysical approaches, crystallographic structural analysis, as well as *in vivo* approaches to investigating the function of myosins in health and disease.

A related topic of interest to this work is the further advancement of the recombinant expression of striated muscle myosins. While the system described herein for expressing these proteins represents a major advancement in the study of myosins, many limitations are posed due to the expense and scale of the current system. It remains of great interest to uncover the muscle specific cell factors necessary to produce active recombinant myosin proteins in more tractable cellular expression systems. One approach that may allow for the investigation of these factors is the targeted knockdown of putative folding cofactors in the existing expression system, the C_2C_{12} myotube, aimed at knocking out the myosin folding ability of the system. The knockdown of folding cofactors could be achieved using shRNA or similar systems. Cofactors identified by this approach could be supplemented, in combination, to cells not normally capable of folding myosins and may make it possible for myosin expression to be accomplished in new cell environments.

REFERENCES

1. Resnicow DI, Deacon JC, Warrick HM, Spudich JA, Leinwand LA. Functional diversity among a family of human skeletal muscle myosin motors. *Proc Natl Acad Sci U S A*. 2010;107:1053-1058

2. Deacon JC, Bloemink MJ, Rezavandi H, Geeves MA, Leinwand LA. Identification of functional differences between recombinant human alpha and beta cardiac myosin motors. *Cell Mol Life Sci*. 2012

3. Houdusse A, Szent-Gyorgyi AG, Cohen C. Three conformational states of scallop myosin s1. *Proc Natl Acad Sci U S A*. 2000;97:11238-11243

4. Buvoli M, Buvoli A, Leinwand LA. Effects of pathogenic proline mutations on myosin assembly. *J Mol Biol*. 2012;415:807-818

5. Alberts B. *Molecular biology of the cell*. New York: Garland Science; 2002.

6. Tregear RT, Marston SB. The crossbridge theory. *Annu Rev Physiol*. 1979;41:723-736

7. Lowy J, Small JV. The organization of myosin and actin in vertebrate smooth muscle. *Nature*. 1970;227:46-51

8. Matthews GG. *Cellular physiology of nerve and muscle*. Osney Mead, Oxford ; Malden, MA: Blackwell Pub.; 2003.

9. Van De Graaff KM. *Human anatomy*. Boston: McGraw-Hill; 2002.

10. Gelfi C, Vasso M, Cerretelli P. Diversity of human skeletal muscle in health and disease: Contribution of proteomics. *J Proteomics*. 2011;74:774-795

11. Raddatz K, Albrecht D, Hochgrafe F, Hecker M, Gotthardt M. A proteome map of murine heart and skeletal muscle. *Proteomics*. 2008;8:1885-1897

12. Pette D, Spamer C. Metabolic properties of muscle fibers. *Fed Proc*. 1986;45:2910-2914

13. Franzini-Armstrong C. Annemarie weber: Ca2+ and the regulation of muscle contraction. *Trends Cell Biol*. 1998;8:251-253

14. Melzer W, Herrmann-Frank A, Luttgau HC. The role of ca2+ ions in excitation-contraction coupling of skeletal muscle fibres. *Biochim Biophys Acta*. 1995;1241:59-116

15. Luther PK. The vertebrate muscle z-disc: Sarcomere anchor for structure and signalling. *J Muscle Res Cell Motil*. 2009;30:171-185

16. Clark KA, McElhinny AS, Beckerle MC, Gregorio CC. Striated muscle cytoarchitecture: An intricate web of form and function. *Annu Rev Cell Dev Biol*. 2002;18:637-706

17. Takahashi K, Hattori A. Alpha-actinin is a component of the z-filament, a structural backbone of skeletal muscle z-disks. *J Biochem*. 1989;105:529-536

18. Sjoblom B, Salmazo A, Djinovic-Carugo K. Alpha-actinin structure and regulation. *Cell Mol Life Sci*. 2008;65:2688-2701

19. Littlefield R, Fowler VM. Defining actin filament length in striated muscle: Rulers and caps or dynamic stability? *Annu Rev Cell Dev Biol*. 1998;14:487-525

20. Marshall WF. Cellular length control systems. *Annu Rev Cell Dev Biol*. 2004;20:677-693

21. McElhinny AS, Kazmierski ST, Labeit S, Gregorio CC. Nebulin: The nebulous, multifunctional giant of striated muscle. *Trends Cardiovasc Med*. 2003;13:195-201

22. Trinick J. Titin and nebulin: Protein rulers in muscle? *Trends Biochem Sci*. 1994;19:405-409

23. Maruyama K. Connectin, an elastic protein from myofibrils. *J Biochem*. 1976;80:405-407

24. Wang K, McClure J, Tu A. Titin: Major myofibrillar components of striated muscle. *Proc Natl Acad Sci U S A*. 1979;76:3698-3702

25. Granzier H, Labeit S. Cardiac titin: An adjustable multi-functional spring. *J Physiol*. 2002;541:335-342

26. Granzier HL, Labeit S. The giant protein titin: A major player in myocardial mechanics, signaling, and disease. *Circ Res*. 2004;94:284-295

27. Granzier H, Wu Y, Siegfried L, LeWinter M. Titin: Physiological function and role in cardiomyopathy and failure. *Heart Fail Rev*. 2005;10:211-223

28. Granzier H, Labeit S. Structure-function relations of the giant elastic protein titin in striated and smooth muscle cells. *Muscle Nerve*. 2007;36:740-755

29. Linke WA. Sense and stretchability: The role of titin and titin-associated proteins in myocardial stress-sensing and mechanical dysfunction. *Cardiovasc Res*. 2008;77:637-648

30. Fukuda N, Granzier HL, Ishiwata S, Kurihara S. Physiological functions of the giant elastic protein titin in mammalian striated muscle. *J Physiol Sci*. 2008;58:151-159

31. Luther PK, Padron R, Ritter S, Craig R, Squire JM. Heterogeneity of z-band structure within a single muscle sarcomere: Implications for sarcomere assembly. *J Mol Biol*. 2003;332:161-169

32. Rowe RW. The ultrastructure of z disks from white, intermediate, and red fibers of mammalian striated muscles. *J Cell Biol*. 1973;57:261-277

33. Stromer MH. Immunocytochemistry of the muscle cell cytoskeleton. *Microsc Res Tech*. 1995;31:95-105

34. Lewin B. *Cells*. Sudbury, Mass.: Jones and Bartlett Publishers; 2007.

35. Lodish HF. *Molecular cell biology*. New York: W.H. Freeman and Company; 2003.

36. Zhao FQ, Craig R. Capturing time-resolved changes in molecular structure by negative staining. *J Struct Biol*. 2003;141:43-52

37. Littlefield R, Almenar-Queralt A, Fowler VM. Actin dynamics at pointed ends regulates thin filament length in striated muscle. *Nat Cell Biol*. 2001;3:544-551

38. Ishiwata S, Funatsu T. Does actin bind to the ends of thin filaments in skeletal muscle? *J Cell Biol*. 1985;100:282-291

39. Sanger JW, Mittal B, Sanger JM. Analysis of myofibrillar structure and assembly using fluorescently labeled contractile proteins. *J Cell Biol*. 1984;98:825-833

40. Bai J, Hartwig JH, Perrimon N. Sals, a wh2-domain-containing protein, promotes sarcomeric actin filament elongation from pointed ends during drosophila muscle growth. *Dev Cell*. 2007;13:828-842

41. Mardahl-Dumesnil M, Fowler VM. Thin filaments elongate from their pointed ends during myofibril assembly in drosophila indirect flight muscle. *J Cell Biol*. 2001;155:1043-1053

42. Bing W, Fraser ID, Marston SB. Troponin i and troponin t interact with troponin c to produce different ca2+-dependent effects on actin-tropomyosin filament motility. *Biochem J*. 1997;327 (Pt 2):335-340

43. Solaro RJ, Rarick HM. Troponin and tropomyosin: Proteins that switch on and tune in the activity of cardiac myofilaments. *Circ Res*. 1998;83:471-480

44. Parmacek MS, Solaro RJ. Biology of the troponin complex in cardiac myocytes. *Prog Cardiovasc Dis*. 2004;47:159-176

45. Hodge T, Cope MJ. A myosin family tree. *J Cell Sci*. 2000;113 Pt 19:3353-3354

46. Bloemink MJ, Geeves MA. Shaking the myosin family tree: Biochemical kinetics defines four types of myosin motor. *Semin Cell Dev Biol*. 2011;22:961-967

47. Weiss A, Mayer DC, Leinwand LA. Diversity of myosin-based motility: Multiple genes and functions. *Soc Gen Physiol Ser*. 1994;49:159-171

48. Staron RS. Correlation between myofibrillar atpase activity and myosin heavy chain composition in single human muscle fibers. *Histochemistry*. 1991;96:21-24

49. Reiser PJ, Moss RL, Giulian GG, Greaser ML. Shortening velocity in single fibers from adult rabbit soleus muscles is correlated with myosin heavy chain composition. *J Biol Chem*. 1985;260:9077-9080

50. Allen DL, Leinwand LA. Postnatal myosin heavy chain isoform expression in normal mice and mice null for iib or iid myosin heavy chains. *Dev Biol*. 2001;229:383-395

51. Lyons GE, Ontell M, Cox R, Sassoon D, Buckingham M. The expression of myosin genes in developing skeletal muscle in the mouse embryo. *J Cell Biol*. 1990;111:1465-1476

52. Bandman E. Continued expression of neonatal myosin heavy chain in adult dystrophic skeletal muscle. *Science*. 1985;227:780-782

53. Wieczorek DF, Periasamy M, Butler-Browne GS, Whalen RG, Nadal-Ginard B. Co-expression of multiple myosin heavy chain genes, in addition to a tissue-specific one, in extraocular musculature. *J Cell Biol*. 1985;101:618-629

54. Butler-Browne GS, Eriksson PO, Laurent C, Thornell LE. Adult human masseter muscle fibers express myosin isozymes characteristic of development. *Muscle Nerve*. 1988;11:610-620

55. Schiaffino S, Reggiani C. Fiber types in mammalian skeletal muscles. *Physiol Rev*. 2011;91:1447-1531

56. Harridge SD. Plasticity of human skeletal muscle: Gene expression to in vivo function. *Exp Physiol*. 2007;92:783-797

57. Pette D, Staron RS. Mammalian skeletal muscle fiber type transitions. *Int Rev Cytol*. 1997;170:143-223

58. Schiaffino S, Reggiani C. Myosin isoforms in mammalian skeletal muscle. *J Appl Physiol*. 1994;77:493-501

59. Schiaffino S, Reggiani C. Molecular diversity of myofibrillar proteins: Gene regulation and functional significance. *Physiol Rev*. 1996;76:371-423

60. Harridge SD, Bottinelli R, Canepari M, Pellegrino MA, Reggiani C, Esbjornsson M, Saltin B. Whole-muscle and single-fibre contractile properties and myosin heavy chain isoforms in humans. *Pflugers Arch*. 1996;432:913-920

61. Harrison BC, Allen DL, Leinwand LA. Iib or not iib? Regulation of myosin heavy chain gene expression in mice and men. *Skelet Muscle*. 2011;1:5

62. Sartore S, Mascarello F, Rowlerson A, Gorza L, Ausoni S, Vianello M, Schiaffino S. Fibre types in extraocular muscles: A new myosin isoform in the fast fibres. *J Muscle Res Cell Motil*. 1987;8:161-172

63. Brueckner JK, Itkis O, Porter JD. Spatial and temporal patterns of myosin heavy chain expression in developing rat extraocular muscle. *J Muscle Res Cell Motil*. 1996;17:297-312

64. Lucas CA, Rughani A, Hoh JF. Expression of extraocular myosin heavy chain in rabbit laryngeal muscle. *J Muscle Res Cell Motil*. 1995;16:368-378

65. Everett AW. Isomyosin expression in human heart in early pre- and post-natal life. *J Mol Cell Cardiol*. 1986;18:607-615

66. Lompre AM, Mercadier JJ, Wisnewsky C, Bouveret P, Pantaloni C, D'Albis A, Schwartz K. Species- and age-dependent changes in the relative amounts of cardiac myosin isoenzymes in mammals. *Dev Biol*. 1981;84:286-290

67. Margossian SS, Lowey S. Substructure of the myosin molecule. 3. Preparation of single-headed derivatives of myosin. *J Mol Biol*. 1973;74:301-311

68. Margossian SS, Lowey S. Substructure of the myosin molecule. Iv. Interactions of myosin and its subfragments with adenosine triphosphate and f-actin. *J Mol Biol*. 1973;74:313-330

69. Cooke R. A new method for producing myosin subfragment-1. *Biochem Biophys Res Commun*. 1972;49:1021-1028

70. McNally EM, Bravo-Zehnder MM, Leinwand LA. Identification of sequences necessary for the association of cardiac myosin subunits. *J Cell Biol*. 1991;113:585-590

71. Weeds AG, Taylor RS. Separation of subfragment-1 isoenzymes from rabbit skeletal muscle myosin. *Nature*. 1975;257:54-56

72. Rayment I, Winkelmann DA. Crystallization of myosin subfragment 1. *Proc Natl Acad Sci U S A*. 1984;81:4378-4380

73. Mornet D, Pantel P, Audemard E, Kassab R. The limited tryptic cleavage of chymotryptic s-1: An approach to the characterization of the actin site in myosin heads. *Biochem Biophys Res Commun*. 1979;89:925-932

74. Spudich JA. How molecular motors work. *Nature*. 1994;372:515-518

75. Smith CA, Rayment I. X-ray structure of the magnesium(ii).Adp.Vanadate complex of the dictyostelium discoideum myosin motor domain to 1.9 a resolution. *Biochemistry*. 1996;35:5404-5417

76. Geeves MA, Holmes KC. Structural mechanism of muscle contraction. *Annu Rev Biochem*. 1999;68:687-728

77. De La Cruz EM, Ostap EM. Relating biochemistry and function in the myosin superfamily. *Curr Opin Cell Biol*. 2004;16:61-67

78. Geeves MA, Fedorov R, Manstein DJ. Molecular mechanism of actomyosin-based motility. *Cell Mol Life Sci*. 2005;62:1462-1477

79. Maughan DW. Kinetics and energetics of the crossbridge cycle. *Heart Fail Rev*. 2005;10:175-185

80. Finer JT, Simmons RM, Spudich JA. Single myosin molecule mechanics: Piconewton forces and nanometre steps. *Nature*. 1994;368:113-119

81. Murphy CT, Rock RS, Spudich JA. A myosin ii mutation uncouples atpase activity from motility and shortens step size. *Nat Cell Biol*. 2001;3:311-315

82. Geisterfer-Lowrance AA, Kass S, Tanigawa G, Vosberg HP, McKenna W, Seidman CE, Seidman JG. A molecular basis for familial hypertrophic cardiomyopathy: A beta cardiac myosin heavy chain gene missense mutation. *Cell*. 1990;62:999-1006

83. Kimura A. Contribution of genetic factors to the pathogenesis of dilated cardiomyopathy: The cause of dilated cardiomyopathy: Genetic or acquired? (genetic-side). *Circ J*. 2011;75:1756-1765; discussion 1765

84. LeWinter MM, VanBuren P. Sarcomeric proteins in hypertrophied and failing myocardium: An overview. *Heart Fail Rev*. 2005;10:173-174

85. Xu Q, Dewey S, Nguyen S, Gomes AV. Malignant and benign mutations in familial cardiomyopathies: Insights into mutations linked to complex cardiovascular phenotypes. *J Mol Cell Cardiol*. 2010;48:899-909

86. Laing NG, Laing BA, Meredith C, Wilton SD, Robbins P, Honeyman K, Dorosz S, Kozman H, Mastaglia FL, Kakulas BA. Autosomal dominant distal myopathy: Linkage to chromosome 14. *Am J Hum Genet*. 1995;56:422-427

87. Mastaglia FL, Phillips BA, Cala LA, Meredith C, Egli S, Akkari PA, Laing NG. Early onset chromosome 14-linked distal myopathy (laing). *Neuromuscul Disord*. 2002;12:350-357

88. Toydemir RM, Rutherford A, Whitby FG, Jorde LB, Carey JC, Bamshad MJ. Mutations in embryonic myosin heavy chain (myh3) cause freeman-sheldon syndrome and sheldon-hall syndrome. *Nat Genet*. 2006;38:561-565

89. Veugelers M, Bressan M, McDermott DA, Weremowicz S, Morton CC, Mabry CC, Lefaivre JF, Zunamon A, Destree A, Chaudron JM, Basson CT. Mutation of perinatal myosin heavy chain associated with a carney complex variant. *N Engl J Med*. 2004;351:460-469

90. Tajsharghi H, Thornell LE, Darin N, Martinsson T, Kyllerman M, Wahlstrom J, Oldfors A. Myosin heavy chain iia gene mutation e706k is pathogenic and its expression increases with age. *Neurology*. 2002;58:780-786

91. Tajsharghi H, Pilon M, Oldfors A. A caenorhabditis elegans model of the myosin heavy chain iia e706k [corrected] mutation. *Ann Neurol*. 2005;58:442-448

92. Epstein HF. Genetic analysis of myosin assembly in caenorhabditis elegans. *Mol Neurobiol*. 1990;4:1-25

93. Spudich JA. In pursuit of myosin function. *Cell Regul*. 1989;1:1-11

94. Kurzawa SE, Manstein DJ, Geeves MA. Dictyostelium discoideum myosin ii: Characterization of functional myosin motor fragments. *Biochemistry*. 1997;36:317-323

95. Swank DM, Wells L, Kronert WA, Morrill GE, Bernstein SI. Determining structure/function relationships for sarcomeric myosin heavy chain by genetic and transgenic manipulation of drosophila. *Microsc Res Tech*. 2000;50:430-442

96. Bernstein SI, Mogami K, Donady JJ, Emerson CP, Jr. Drosophila muscle myosin heavy chain encoded by a single gene in a cluster of muscle mutations. *Nature*. 1983;302:393-397

97. Lowey S, Lesko LM, Rovner AS, Hodges AR, White SL, Low RB, Rincon M, Gulick J, Robbins J. Functional effects of the hypertrophic cardiomyopathy r403q mutation are different in an alpha- or beta-myosin heavy chain backbone. *J Biol Chem*. 2008;283:20579-20589

98. Epstein HF, Waterston RH, Brenner S. A mutant affecting the heavy chain of myosin in caenorhabditis elegans. *J Mol Biol*. 1974;90:291-300

99. Waterston RH. The minor myosin heavy chain, mhca, of caenorhabditis elegans is necessary for the initiation of thick filament assembly. *EMBO J*. 1989;8:3429-3436

100. Beall CJ, Sepanski MA, Fyrberg EA. Genetic dissection of drosophila myofibril formation: Effects of actin and myosin heavy chain null alleles. *Genes Dev*. 1989;3:131-140

101. Jones WK, Grupp IL, Doetschman T, Grupp G, Osinska H, Hewett TE, Boivin G, Gulick J, Ng WA, Robbins J. Ablation of the murine alpha myosin heavy chain gene leads to dosage effects and functional deficits in the heart. *J Clin Invest*. 1996;98:1906-1917

102. Nishi H, Kimura A, Harada H, Koga Y, Adachi K, Matsuyama K, Koyanagi T, Yasunaga S, Imaizumi T, Toshima H, et al. A myosin missense mutation, not a null allele, causes familial hypertrophic cardiomyopathy. *Circulation*. 1995;91:2911-2915

103. Allen DL, Harrison BC, Leinwand LA. Inactivation of myosin heavy chain genes in the mouse: Diverse and unexpected phenotypes. *Microsc Res Tech*. 2000;50:492-499

104. Acakpo-Satchivi LJ, Edelmann W, Sartorius C, Lu BD, Wahr PA, Watkins SC, Metzger JM, Leinwand L, Kucherlapati R. Growth and muscle defects in mice lacking adult myosin heavy chain genes. *J Cell Biol*. 1997;139:1219-1229

105. Sartorius CA, Lu BD, Acakpo-Satchivi L, Jacobsen RP, Byrnes WC, Leinwand LA. Myosin heavy chains iia and iid are functionally distinct in the mouse. *J Cell Biol*. 1998;141:943-953

106. Clark RJ, Nyitrai M, Webb MR, Geeves MA. Probing nucleotide dissociation from myosin in vitro using microgram quantities of myosin. *J Muscle Res Cell Motil*. 2003;24:315-321

107. Conibear PB, Kuhlman PA, Bagshaw CR. Measurement of atpase activities of myosin at the level of tracks and single molecules. *Adv Exp Med Biol*. 1998;453:15-26; discussion 26-17

108. Weiss S, Chizhov I, Geeves MA. A flash photolysis fluorescence/light scattering apparatus for use with sub microgram quantities of muscle proteins. *J Muscle Res Cell Motil*. 2000;21:423-432

109. Bagshaw CR, Conibear PB. Single molecule enzyme kinetics: Application to myosin atpases. *Biochem Soc Trans*. 1999;27:33-37

110. Sweeney HL, Rosenfeld SS, Brown F, Faust L, Smith J, Xing J, Stein LA, Sellers JR. Kinetic tuning of myosin via a flexible loop adjacent to the nucleotide binding pocket. *J Biol Chem*. 1998;273:6262-6270

111. Chow D, Srikakulam R, Chen Y, Winkelmann DA. Folding of the striated muscle myosin motor domain. *J Biol Chem*. 2002;277:36799-36807

112. Landsverk HB, Hakelien AM, Kuntziger T, Robl JM, Skalhegg BS, Collas P. Reprogrammed gene expression in a somatic cell-free extract. *EMBO Rep*. 2002;3:384-389

113. Landsverk ML, Li S, Hutagalung AH, Najafov A, Hoppe T, Barral JM, Epstein HF. The unc-45 chaperone mediates sarcomere assembly through myosin degradation in caenorhabditis elegans. *J Cell Biol*. 2007;177:205-210

114. Liu L, Srikakulam R, Winkelmann DA. Unc45 activates hsp90-dependent folding of the myosin motor domain. *J Biol Chem*. 2008;283:13185-13193

115. Price MG, Landsverk ML, Barral JM, Epstein HF. Two mammalian unc-45 isoforms are related to distinct cytoskeletal and muscle-specific functions. *J Cell Sci*. 2002;115:4013-4023

116. Srikakulam R, Liu L, Winkelmann DA. Unc45b forms a cytosolic complex with hsp90 and targets the unfolded myosin motor domain. *PLoS One*. 2008;3:e2137

117. Srikakulam R, Winkelmann DA. Myosin ii folding is mediated by a molecular chaperonin. *J Biol Chem*. 1999;274:27265-27273

118. Srikakulam R, Winkelmann DA. Chaperone-mediated folding and assembly of myosin in striated muscle. *J Cell Sci*. 2004;117:641-652

119. Lowey S. Functional consequences of mutations in the myosin heavy chain at sites implicated in familial hypertrophic cardiomyopathy. *Trends Cardiovasc Med*. 2002;12:348-354

120. Barany M. Atpase activity of myosin correlated with speed of muscle shortening. *J Gen Physiol*. 1967;50:Suppl:197-218

121. Brooks SV, Faulkner JA, McCubbrey DA. Power outputs of slow and fast skeletal muscles of mice. *J Appl Physiol*. 1990;68:1282-1285

122. Close RI. Dynamic properties of mammalian skeletal muscles. *Physiol Rev*. 1972;52:129-197

123. Bottinelli R, Canepari M, Cappelli V, Reggiani C. Maximum speed of shortening and atpase activity in atrial and ventricular myocardia of hyperthyroid rats. *Am J Physiol*. 1995;269:C785-790

124. Geiger PC, Cody MJ, Macken RL, Sieck GC. Maximum specific force depends on myosin heavy chain content in rat diaphragm muscle fibers. *J Appl Physiol*. 2000;89:695-703

125. Korte FS, Herron TJ, Rovetto MJ, McDonald KS. Power output is linearly related to myhc content in rat skinned myocytes and isolated working hearts. *Am J Physiol Heart Circ Physiol*. 2005;289:H801-812

126. Rayment I, Smith C, Yount RG. The active site of myosin. *Annu Rev Physiol*. 1996;58:671-702

127. Yanagida T, Nakase M, Nishiyama K, Oosawa F. Direct observation of motion of single f-actin filaments in the presence of myosin. *Nature*. 1984;307:58-60

128. Homsher E. The time course of atp cleavage by contracting amphibian and mammalian skeletal muscles. *Adv Exp Med Biol*. 1986;194:27-40

129. Lionne C, Iorga B, Candau R, Travers F. Why choose myofibrils to study muscle myosin atpase? *J Muscle Res Cell Motil*. 2003;24:139-148

130. Candau R, Iorga B, Travers F, Barman T, Lionne C. At physiological temperatures the atpase rates of shortening soleus and psoas myofibrils are similar. *Biophys J*. 2003;85:3132-3141

131. Knight PJ, Trinick JA. Preparation of myofibrils. *Methods Enzymol*. 1982;85 Pt B:9-12

132. Bloemink MJ, Adamek N, Reggiani C, Geeves MA. Kinetic analysis of the slow skeletal myosin mhc-1 isoform from bovine masseter muscle. *J Mol Biol*. 2007;373:1184-1197

133. Iorga B, Adamek N, Geeves MA. The slow skeletal muscle isoform of myosin shows kinetic features common to smooth and non-muscle myosins. *J Biol Chem*. 2007;282:3559-3570

134. Malnasi-Csizmadia A, Pearson DS, Kovacs M, Woolley RJ, Geeves MA, Bagshaw CR. Kinetic resolution of a conformational transition and the atp hydrolysis step using relaxation methods with a dictyostelium myosin ii mutant containing a single tryptophan residue. *Biochemistry*. 2001;40:12727-12737

135. De La Cruz EM, Ostap EM. Kinetic and equilibrium analysis of the myosin atpase. *Methods Enzymol*. 2009;455:157-192

136. Stein LA, Chock PB, Eisenberg E. The rate-limiting step in the actomyosin adenosinetriphosphatase cycle. *Biochemistry*. 1984;23:1555-1563

137. Chalovich JM, Stein LA, Greene LE, Eisenberg E. Interaction of isozymes of myosin subfragment 1 with actin: Effect of ionic strength and nucleotide. *Biochemistry*. 1984;23:4885-4889

138. Iorga B, Candau R, Travers F, Barman T, Lionne C. Does phosphate release limit the atpases of soleus myofibrils? Evidence that (a)m. Adp.Pi states predominate on the cross-bridge cycle. *J Muscle Res Cell Motil*. 2004;25:367-378

139. Orentlicher M, Gersho A. A quantitative model of actin-myosin interaction in skeletal muscle. *Biophys J*. 1977;18:141-159

140. Stehle R, Iorga B. Kinetics of cardiac sarcomeric processes and rate-limiting steps in contraction and relaxation. *J Mol Cell Cardiol*. 2010;48:843-850

141. He TC, Zhou S, da Costa LT, Yu J, Kinzler KW, Vogelstein B. A simplified system for generating recombinant adenoviruses. *Proc Natl Acad Sci U S A*. 1998;95:2509-2514

142. Janknecht R, Nordheim A. Affinity purification of histidine-tagged proteins transiently produced in hela cells. *Gene*. 1992;121:321-324

143. Janknecht R, de Martynoff G, Lou J, Hipskind RA, Nordheim A, Stunnenberg HG. Rapid and efficient purification of native histidine-tagged protein expressed by recombinant vaccinia virus. *Proc Natl Acad Sci U S A*. 1991;88:8972-8976

144. Gill SC, von Hippel PH. Calculation of protein extinction coefficients from amino acid sequence data. *Anal Biochem*. 1989;182:319-326

145. Trybus KM. Biochemical studies of myosin. *Methods*. 2000;22:327-335

146. Pardee JD, Spudich JA. Purification of muscle actin. *Methods Enzymol*. 1982;85 Pt B:164-181

147. Kachur TM, Pilgrim DB. Myosin assembly, maintenance and degradation in muscle: Role of the chaperone unc-45 in myosin thick filament dynamics. *Int J Mol Sci*. 2008;9:1863-1875

148. Sweeney HL, Straceski AJ, Leinwand LA, Tikunov BA, Faust L. Heterologous expression of a cardiomyopathic myosin that is defective in its actin interaction. *J Biol Chem*. 1994;269:1603-1605

149. Toyoshima YY, Kron SJ, McNally EM, Niebling KR, Toyoshima C, Spudich JA. Myosin subfragment-1 is sufficient to move actin filaments in vitro. *Nature*. 1987;328:536-539

150. Stienen GJ, Kiers JL, Bottinelli R, Reggiani C. Myofibrillar atpase activity in skinned human skeletal muscle fibres: Fibre type and temperature dependence. *J Physiol*. 1996;493 (Pt 2):299-307

151. Han YS, Geiger PC, Cody MJ, Macken RL, Sieck GC. Atp consumption rate per cross bridge depends on myosin heavy chain isoform. *J Appl Physiol*. 2003;94:2188-2196

152. Bottinelli R, Canepari M, Reggiani C, Stienen GJ. Myofibrillar atpase activity during isometric contraction and isomyosin composition in rat single skinned muscle fibres. *J Physiol*. 1994;481 (Pt 3):663-675

153. Bottinelli R, Betto R, Schiaffino S, Reggiani C. Maximum shortening velocity and coexistence of myosin heavy chain isoforms in single skinned fast fibres of rat skeletal muscle. *J Muscle Res Cell Motil*. 1994;15:413-419

154. Drachman DB, Johnston DM. Development of a mammalian fast muscle: Dynamic and biochemical properties correlated. *J Physiol*. 1973;234:29-42

155. Lowey S, Waller GS, Trybus KM. Function of skeletal muscle myosin heavy and light chain isoforms by an in vitro motility assay. *J Biol Chem*. 1993;268:20414-20418

156. Fitts RH, Bodine SC, Romatowski JG, Widrick JJ. Velocity, force, power, and ca2+ sensitivity of fast and slow monkey skeletal muscle fibers. *J Appl Physiol*. 1998;84:1776-1787

157. Close RI, Luff AR. Dynamic properties of inferior rectus muscle of the rat. *J Physiol*. 1974;236:259-270

158. Sciote JJ, Morris TJ, Brandon CA, Horton MJ, Rosen C. Unloaded shortening velocity and myosin heavy chain variations in human laryngeal muscle fibers. *Ann Otol Rhinol Laryngol*. 2002;111:120-127

159. Takiguchi K, Hayashi H, Kurimoto E, Higashi-Fujime S. In vitro motility of skeletal muscle myosin and its proteolytic fragments. *J Biochem*. 1990;107:671-679

160. Lehninger AL, Nelson DL, Cox MM. *Lehninger principles of biochemistry*. New York: W.H. Freeman; 2005.

161. Harris DE, Work SS, Wright RK, Alpert NR, Warshaw DM. Smooth, cardiac and skeletal muscle myosin force and motion generation assessed by cross-bridge mechanical interactions in vitro. *J Muscle Res Cell Motil*. 1994;15:11-19

162. Malmqvist UP, Aronshtam A, Lowey S. Cardiac myosin isoforms from different species have unique enzymatic and mechanical properties. *Biochemistry*. 2004;43:15058-15065

163. Nguyen TT, Hayes E, Mulieri LA, Leavitt BJ, ter Keurs HE, Alpert NR, Warshaw DM. Maximal actomyosin atpase activity and in vitro myosin motility are unaltered in human mitral regurgitation heart failure. *Circ Res*. 1996;79:222-226

164. Tyska MJ, Hayes E, Giewat M, Seidman CE, Seidman JG, Warshaw DM. Single-molecule mechanics of r403q cardiac myosin isolated from the mouse model of familial hypertrophic cardiomyopathy. *Circ Res*. 2000;86:737-744

165. VanBuren P, Harris DE, Alpert NR, Warshaw DM. Cardiac v1 and v3 myosins differ in their hydrolytic and mechanical activities in vitro. *Circ Res*. 1995;77:439-444

166. Goodrich JA, Kugel JF. *Binding and kinetics for molecular biologists*. Cold Spring Harbor, N.Y.: Cold Spring Harbor Laboratory Press; 2007.

167. Miyata S, Minobe W, Bristow MR, Leinwand LA. Myosin heavy chain isoform expression in the failing and nonfailing human heart. *Circ Res*. 2000;86:386-390

168. Herron TJ, Korte FS, McDonald KS. Loaded shortening and power output in cardiac myocytes are dependent on myosin heavy chain isoform expression. *Am J Physiol Heart Circ Physiol*. 2001;281:H1217-1222

169. Herron TJ, McDonald KS. Small amounts of alpha-myosin heavy chain isoform expression significantly increase power output of rat cardiac myocyte fragments. *Circ Res*. 2002;90:1150-1152

170. Herron TJ, Vandenboom R, Fomicheva E, Mundada L, Edwards T, Metzger JM. Calcium-independent negative inotropy by beta-myosin heavy chain gene transfer in cardiac myocytes. *Circ Res*. 2007;100:1182-1190

171. James J, Hor K, Moga MA, Martin LA, Robbins J. Effects of myosin heavy chain manipulation in experimental heart failure. *J Mol Cell Cardiol*.48:999-1006

172. James J, Martin L, Krenz M, Quatman C, Jones F, Klevitsky R, Gulick J, Robbins J. Forced expression of alpha-myosin heavy chain in the rabbit ventricle results in cardioprotection under cardiomyopathic conditions. *Circulation*. 2005;111:2339-2346

173. Criddle AH, Geeves MA, Jeffries T. The use of actin labelled with n-(1-pyrenyl)iodoacetamide to study the interaction of actin with myosin subfragments and troponin/tropomyosin. *Biochem J*. 1985;232:343-349

174. Geeves MA, Jeffries TE, Millar NC. Atp-induced dissociation of rabbit skeletal actomyosin subfragment 1. Characterization of an isomerization of the ternary acto-s1-atp complex. *Biochemistry*. 1986;25:8454-8458

175. Jackson AP, Bagshaw CR. Kinetic trapping of intermediates of the scallop heavy meromyosin adenosine triphosphatase reaction revealed by formycin nucleotides. *Biochem J*. 1988;251:527-540

176. Jackson AP, Bagshaw CR. Transient-kinetic studies of the adenosine triphosphatase activity of scallop heavy meromyosin. *Biochem J*. 1988;251:515-526

177. Kouyama T, Mihashi K. Fluorimetry study of n-(1-pyrenyl)iodoacetamide-labelled f-actin. Local structural change of actin protomer both on polymerization and on binding of heavy meromyosin. *Eur J Biochem*. 1981;114:33-38

178. Kurzawa SE, Geeves MA. A novel stopped-flow method for measuring the affinity of actin for myosin head fragments using microgram quantities of protein. *J Muscle Res Cell Motil*. 1996;17:669-676

179. Millar NC, Geeves MA. The limiting rate of the atp-mediated dissociation of actin from rabbit skeletal muscle myosin subfragment 1. *FEBS Lett*. 1983;160:141-148

180. Millar NC, Geeves MA. Protein fluorescence changes associated with atp and adenosine 5'-[gamma-thio]triphosphate binding to skeletal muscle myosin subfragment 1 and actomyosin subfragment 1. *Biochem J*. 1988;249:735-743

181. Nyitrai M, Rossi R, Adamek N, Pellegrino MA, Bottinelli R, Geeves MA. What limits the velocity of fast-skeletal muscle contraction in mammals? *J Mol Biol*. 2006;355:432-442

182. Stehle R, Lionne C, Travers F, Barman T. Kinetics of the initial steps of rabbit psoas myofibrillar atpases studied by tryptophan and pyrene fluorescence stopped-flow and rapid flow-quench. Evidence that cross-bridge detachment is slower than atp binding. *Biochemistry*. 2000;39:7508-7520

183. Kurzawa-Goertz SE, Perreault-Micale CL, Trybus KM, Szent-Gyorgyi AG, Geeves MA. Loop i can modulate adp affinity, atpase activity, and motility of different scallop myosins. Transient kinetic analysis of s1 isoforms. *Biochemistry*. 1998;37:7517-7525

184. Ritchie MD, Geeves MA, Woodward SK, Manstein DJ. Kinetic characterization of a cytoplasmic myosin motor domain expressed in dictyostelium discoideum. *Proc Natl Acad Sci U S A*. 1993;90:8619-8623

185. Burghardt TP, Garamszegi SP, Park S, Ajtai K. Tertiary structural changes in the cleft containing the atp sensitive tryptophan and reactive thiol are consistent with pivoting of the myosin heavy chain at gly699. *Biochemistry*. 1998;37:8035-8047

186. Siemankowski RF, Wiseman MO, White HD. Adp dissociation from actomyosin subfragment 1 is sufficiently slow to limit the unloaded shortening velocity in vertebrate muscle. *Proc Natl Acad Sci U S A*. 1985;82:658-662

187. Siemankowski RF, White HD. Kinetics of the interaction between actin, adp, and cardiac myosin-s1. *J Biol Chem*. 1984;259:5045-5053

188. Bamshad M, Van Heest AE, Pleasure D. Arthrogryposis: A review and update. *J Bone Joint Surg Am*. 2009;91 Suppl 4:40-46

189. Shyy W, Wang K, Sheffield VC, Morcuende JA. Evaluation of embryonic and perinatal myosin gene mutations and the etiology of congenital idiopathic clubfoot. *J Pediatr Orthop*. 2010;30:231-234

190. Tajsharghi H, Kimber E, Kroksmark AK, Jerre R, Tulinius M, Oldfors A. Embryonic myosin heavy-chain mutations cause distal arthrogryposis and developmental myosin myopathy that persists postnatally. *Arch Neurol*. 2008;65:1083-1090

191. Toydemir RM, Bamshad MJ. Sheldon-hall syndrome. *Orphanet J Rare Dis*. 2009;4:11

192. Weiss A, Schiaffino S, Leinwand LA. Comparative sequence analysis of the complete human sarcomeric myosin heavy chain family: Implications for functional diversity. *J Mol Biol*. 1999;290:61-75

193. Lowes BD, Gilbert EM, Abraham WT, Minobe WA, Larrabee P, Ferguson D, Wolfel EE, Lindenfeld J, Tsvetkova T, Robertson AD, Quaife RA, Bristow MR. Myocardial gene expression in dilated cardiomyopathy treated with beta-blocking agents. *N Engl J Med*. 2002;346:1357-1365

194. Nakao K, Minobe W, Roden R, Bristow MR, Leinwand LA. Myosin heavy chain gene expression in human heart failure. *J Clin Invest*. 1997;100:2362-2370

195. Buvoli M, Hamady M, Leinwand LA, Knight R. Bioinformatics assessment of beta-myosin mutations reveals myosin's high sensitivity to mutations. *Trends Cardiovasc Med*. 2008;18:141-149

196. Rayment I, Holden HM, Sellers JR, Fananapazir L, Epstein ND. Structural interpretation of the mutations in the beta-cardiac myosin that have been implicated in familial hypertrophic cardiomyopathy. *Proc Natl Acad Sci U S A*. 1995;92:3864-3868

197. Watkins H, Rosenzweig A, Hwang DS, Levi T, McKenna W, Seidman CE, Seidman JG. Characteristics and prognostic implications of myosin missense mutations in familial hypertrophic cardiomyopathy. *N Engl J Med*. 1992;326:1108-1114

198. Roopnarine O, Leinwand LA. Functional analysis of myosin mutations that cause familial hypertrophic cardiomyopathy. *Biophys J*. 1998;75:3023-3030

199. Marian AJ, Roberts R. Molecular genetic basis of hypertrophic cardiomyopathy: Genetic markers for sudden cardiac death. *J Cardiovasc Electrophysiol*. 1998;9:88-99

200. Laredo R, Monserrat L, Hermida-Prieto M, Fernandez X, Rodriguez I, Cazon L, Alvarino I, Dumont C, Pinon P, Peteiro J, Bouzas B, Castro-Beiras A. [beta-myosin heavy-chain gene mutations in patients with hypertrophic cardiomyopathy]. *Rev Esp Cardiol*. 2006;59:1008-1018

201. Oldfors A. Hereditary myosin myopathies. *Neuromuscul Disord*. 2007;17:355-367

202. Pette D, Staron RS. Myosin isoforms, muscle fiber types, and transitions. *Microsc Res Tech*. 2000;50:500-509

203. Gupta M, Zak R. Reversibility of load-induced changes in myosin heavy chain gene expression. *Am J Physiol*. 1992;262:R346-349

204. Greenberg MJ, Kazmierczak K, Szczesna-Cordary D, Moore JR. Cardiomyopathy-linked myosin regulatory light chain mutations disrupt myosin strain-dependent biochemistry. *Proc Natl Acad Sci U S A*. 2010;107:17403-17408

205. Herron TJ, Devaney E, Mundada L, Arden E, Day S, Guerrero-Serna G, Turner I, Westfall M, Metzger JM. Ca2+-independent positive molecular inotropy for failing rabbit and human cardiac muscle by alpha-myosin motor gene transfer. *FASEB J*. 2010;24:415-424

206. Agbulut O, Noirez P, Beaumont F, Butler-Browne G. Myosin heavy chain isoforms in postnatal muscle development of mice. *Biol Cell*. 2003;95:399-406

APPENDIX A - ABBREVIATIONS

ADP	Adenosine diphosphate
ATP	Adenosine triphosphate
C_2C_{12}	Mouse myoblast cell line, can be differentiated into myotubes and infected with recombinant adenoviruses to express human myosin motors
CMV	Cytomegalovirus, a constitutive promoter of viral origin
CS	Calf serum
DMEM	Dulbecco's modified Eagle's medium
DTT	Dithiothreitol, a reducing agent used to extend the active lifetime of purified protein
E1	Early gene 1 from the adenoviral genome, essential for the replication competence of a virion, but can be supplemented by host cell production, as is present in HEK293 cells
eGFP	Enhanced green fluorescent protein
ELC	Essential myosin light chain
F-actin	Filamentous actin, polymerized actin monomers to mimic the thin filament for in vitro experiments
FBS	Fetal bovine serum
HCM	Hypertrophic cardiomyopathy
HEK293	Human epithelial kidney cell line, adherant cell line which complements the AdEasy system for viral replication by expressing the adenoviral gene, E1
HPLC	High performance liquid chromatography
HS	Horse serum
IQ domain	Myosin light chain binding peptide sequence found on the lever arm, commonly initiated with isoleucine and glutamate
KCl	Potassium chloride
$MgCl_2$	Magnesium chloride, providing magnesium ions necessary for myosin ATPase activity

MOPS	3-(N-morpholino)propanesulfonic acid, buffer
MyHC	Myosin heavy chain protein
NaN_3	Sodium Azide
NaOH	Sodium hydroxide
PFU	Plaque-forming units, a term for the quantificatino of virus based on an empirical metric of the infectivity of a solution
P_i	Inorganic phosphate, in this case produced as a product of the hydrolysis of adenosine triphosphate into adenosine diphosphate and inorganic phosphate
RLC	Regulatory myosin light chain
S1	Myosin heavy chain subfragment 1 contains the motor domain and lever arm, including binding sites for both essential and regulatory myosin light chains, with which it copurifies from C2C12 cells
SDS-PAGE	Sodium dodecyl sulfate poly-acrylamide gel electrophoresis, a denaturing protein separation technique for visualization of individual protein constituents of a substance
sS1	Myosin heavy chain short-subfragment 1 or short-S1 contains the motor domain and only a portion of the lever arm, including only the essential myosin light chain binding site
w/v	Weight per volume, for designating which method was used in the preparation of a solution

APPENDIX B - EQUATIONS

Equation 1: $$V_{obs} = \frac{k_{cat}[S1] \bullet [F-Actin]}{K_{ATPase} + [F-actin]}$$

Equation 2: $$F = A \cdot (1 - e^{(-k_{obs} \cdot t)}) + F_{\infty}$$

Equation 3A: $$k_{obs} = \frac{k_{max}[ATP]}{K_{1/2} + [ATP]}$$

Equation 3B: $$k_{obs} = \frac{K_{1A} k_{+2A}[ATP]}{1 + K_{1A}[ATP]}$$

Equation 4: $$F = A_{fast} \cdot (1 - e^{(-k_{obs(fast)} \cdot t)}) + A_{slow} \cdot (1 - e^{(-k_{obs(slow)} \cdot t)}) + F_{\infty}$$

Equation 5: $$\frac{k_{obs}}{k_0} = k_{rel} = \frac{1}{1 + ([ADP] / K_{5A})}$$

Equation 6A: $$A = \frac{A_{max}[ADP]}{K_5 + [ADP]} + A_{min}$$

Equation 6B: $$A = \frac{A_{max} K_5}{K_5 + [ADP]} + A_{min}$$

Equation 7: $$k_{obs} = K_{1A} k_{+2A}$$

Equation 8: $$A = \frac{[S1] + K_D + [actin] - \sqrt{([S1] + K_D + [actin])^2 - \frac{4}{[S1][actin]}}}{2[actin]}$$